Dendritic integration of synaptic inputs in the stellate cells of the medial entorhinal cortex

Gabija Toleikyte

University College London (UCL)

Thesis submitted towards the degree of

Doctor of Philosophy in Neuroscience

2015

London

DECLARATION

I, Gabija Toleikyte, confirm that the work presented in this thesis is my own. Where information is derived from other sources, I confirm that this has been indicated in the thesis.

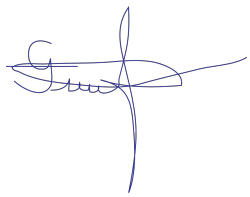

Gabija Toleikyte

Dedicated to my Family.

G.T.

ABSTRACT

Grid cells fire action potentials at regular intervals in space, giving rise to a spectacularly regular and stable hexagonal arrangement of firing fields (Hafting et al., 2005). For this reason they have been proposed to represent a neural code for path integration (McNaughton et al., 2006). Grid cells have primarily been found in layer II of the medial entorhinal cortex (MEC) (Hafting et al., 2005). In this thesis I explore the dendritic properties of putative grid cells in MEC layer II and how they may contribute to generating the grid cell firing pattern.

To assess the spatial and temporal dynamics of dendritic integration I have used patterned two-photon glutamate uncaging *in vitro* in combination with somatic whole cell recordings. My findings suggest that the principal neurons of MEC are highly excitable, exhibiting supralinear summation of near-simultaneous inputs and fast and slow dendritic spikes. Supralinear summation is timing-dependent and inputs are summated in a linear manner if separated by 8 ms time intervals. In order to understand the biophysical mechanisms of supralinear summation I blocked NMDA receptors and voltage-gated sodium channels (VGSCs) with D-AP5 and TTX respectively. Both supralinearity and dendritic spikes were abolished in the presence of both blockers, while TTX alone reduced supralinearity and abolished fast but not slow dendritic spikes. This suggests that fast dendritic spikes are largely mediated by VGSCs and slow dendritic spikes by NMDA receptors.

Furthermore, I have assessed dendritic integration in physiologically relevant conditions by injecting current waveform to produce *in vivo*-

like membrane potential dynamics, recorded when an animal was crossing a firing field of a MEC II principal neuron in a virtual environment (Schmidt-Hieber & Häusser, 2013). *In vivo*-like membrane potential dynamics increased supralinearity of the integral of EPSPs and probability of dendritic spikes.

These findings have been integrated in a continuous attractor network model of grid cell firing by Christoph Schmidt-Hieber, to assess their relevance for the grid cell rate and temporal code, that revealed that supralinear dendritic integration increases grid cell rate code robustness and fast dendritic sodium spikes increase the precision of the temporal code (phase precession) of grid cells.

To conclude, in this thesis I demonstrated that dendrites of principal neurons of MEC layer II integrate synaptic inputs in a highly supralinear manner, mediated by the VGSCs and NMDARs and boosted by putative dendritic spikes. Both supralinearity and proportion of dendritic spikes are increased under *in vivo*-like membrane potential dynamics. These findings suggest the hypothesis for the intracellular mechanisms that mediate the robustness of grid cell firing.

ACKNOWLEDGEMENTS

The work presented here has been a long journey of mine and many other people I was lucky enough to meet on the way. Some of them contributed to my work directly through supervision, help with troubleshooting experiments and analyses or during the writing process. Others though have been there for me when the going got rough, keeping my spirit up by creating a wonderfully accepting and loving environment where I could truly be who I was and discover my ways.

Firstly, I am extremely grateful to my supervisor Prof. Michael Häusser for the opportunity to do research in his laboratory and for support throughout my PhD. Also, I would like to thank my wonderful collaborator Dr. Christoph Schmidt-Hieber, who has always been there time after time, offering me assistance, encouragement and invaluable support in troubleshooting the experiments and analyses. Moreover, he has shown me the beauty and creativity of programming mainly by his own example and his own love for it. His integrity, responsibility and care for my success were the cornerstones of this thesis and helped ensure that it saw the light of day.

I am also very grateful to other current and prior postdoctoral and permanent researchers in the lab: Christian Willms, Adam Packer, Tiago Branco, Martine Groen, Dara Sosulski, And Roth and Beverly Clarks for many fruitful discussions and lots of help with troubleshooting in experiments and analyses. I am also extremely grateful to a wonderful community of current and former PhD students from the lab: Charlotte Arlt, Sarah Rieubland, James Cottam, Alex

Matthy, Yuya Kanemoto, Lisa Beeren and Kate Powell. A distinctively big thank you goes to Matej Macak, my partner in crime for MNI-glutamate uncaging and rig troubleshooting matters. Also, I am very grateful to the Lab support team consisting of Matthew Hoddinott, Arifa Naeem and So Yon Chun for their caring assistance in creating great conditions for the experiments and eliminating lots of practical worries.

I am very grateful to the Wellcome Trust for the 4-year scholarship that allowed me to undertake this wonderful research journey without a financial worry. Moreover, I am thankful to the Gatsby Charitable Foundation, the Alexander von Humboldt Foundation and the European Research Council for their financial support of my experiments.

I am extremely thankful to the proofreaders of this thesis Christoph Schmidt-Hieber, Martine Groen, Dara Sosulski, Mark Shuttleworth, Anna Wilton, Tomas Adejumo and Richard Abbott.

Last but not leaset I am very grateful to my amazing family, who have always been there to support me with their unconditional love and belief in me. A distinctively big thank you goes to my Mum, who by her own example showed me that the sky is the limit. Thanks to my beautiful Dad, who unfortunately passed away six months before this thesis saw the light of day. Huge thanks to my little brother Algirdas, also a PhD student at the UCL, and his wife Justina, for being my precious family in London and for the best gift they could have possibly ever given me – my wonderful niece and goddaughter Julija. Thanks to my older brother Zigmantas, who was the first of our quintet to have received a PhD (from the University of Copenhagen), for such a perfect example of determination and persistence, and his wife Rasita and gorgeous son Mykolas for supporting him throughout. A big thank you to my truly beautiful and strong sisters Jadvyga and Ursule for being wonderfully loving and supporting through all the years.

Moreover, huge thanks to my fantastic flatmates Charlotte Arlt, Karolina Dirgelaite and Filipa Quitero for such a wonderful home.

Finally, I am very grateful for three exceptional activities, which I was blessed to find during my PhD: coaching, climbing and cycling, which kept me sane and happy through all these years. Also, I am very grateful to my mentors and coaches Cathy Lasher, Lucia Labouchere and Povilas Petrauskas for their care and guidance when I needed it the most.

Only with the help of the people mentioned here and many more this long and challenging project has reached the light of day.

THANK YOU ALL!

TABLE OF CONTENTS

DECLARATION 2
ABSTRACT 4
ACKNOWLEDGEMENTS 6
TABLE OF CONTENTS 9
LIST OF FIGURES 12
ABBREVIATIONS 16
1. INTRODUCTION 17
1.1 Hippocampal formation and parahippocampal region 19
1.1.1 HF and PHR anatomy 19
1.1.2 HF and PHR connectivity 21
1.2 Grid cells 23
1.2.1 Firing properties 24
1.2.2 Phase precession 31
1.2.3 Membrane potential dynamics 33
1.3 Grid cell models 35
1.3.1 Oscillatory interference models 35
1.3.2 Continuous attractor network models 38
1.4 MEC II cell types 41
1.4.1 Stellate cells 41
1.4.2 Pyramidal cells 45
1.4.3 Cellular phenotype of grid cells 49
1.5 DENDRITIC INTEGRATION 50
1.5.1 Factors influencing dendritic integration 51
1.5.2 Input location 52
1.5.3 Active conductances 53
1.5.4 Dendritic spikes 54
1.5.5 Dendritic integration in different cells 58
1.5.6 Dendritic integration and spatial navigation 59
1.6 Aims of this thesis 61
2. MATERIALS AND METHODS 62

2.1 Electrophysiology 62
2.1.1 Slicing and experimental solutions 62
2.1.2 Slicing procedure 62
2.1.3 Whole-cell patch clamp recordings 63
2.1.4 Cell type identification 64
2.2 Two-photon imaging and uncaging 67
2.2.1 MNI-glutamate uncaging 67
2.2.2 Uncaging on single dendritic branch 68
2.2.3 Uncaging on two dendritic branches 69
2.3 *In vivo*-like membrane potential dynamics 69
2.4 Data analysis 72
2.4.1 Input-output function 72
2.4.2 Identification of fast and slow dendritic spikes 74
2.4.3 Statistics 76
3. DENDRITIC INTEGRATION IN STELLATE CELLS OF MEC II 77
3.1 Introduction 77
3.2 Results 79
3.2.1 Characteristics of uncaging-evoked EPSPs 79
3.2.2 Stellate cell input-output function of simultaneous synaptic inputs 81
3.2.3 Dendritic integration of non-simultaneous synaptic inputs 91
3.3 Discussion 95
4. MECHANISMS UNDERLYING SUPRALINEAR DENDRITIC INTEGRATION IN MEC II STELLATE CELLS 97
4.1 Introduction 97
4.1.1 Mechanisms of nonlinearity in other cell types 97
4.1.2 Dendritic spikes 98
4.1.3 Active conductances in the MEC II stellate cells 99
4.2 Results 102
4.2.1 Dendritic spikes 102
4.2.2 Pharmacology 105
4.3 Discussion 109

5. INTEGRATION OF INPUTS FROM MULTIPLE DENDRITES AND DURING *IN VIVO*-LIKE MEMBRANE POTENTIAL DYNAMICS IN STELLATE CELLS 111

5.1 Introduction 111

5.2 Results 112

5.2.1 Dendritic integration of inputs to a single dendritic branch during somatic *in vivo*-like membrane potential dynamics 112

5.2.2 Dendritic integration of inputs from two dendritic branches .. 118

5.3 Discussion 124

6. DENDRITIC INTEGRATION IN MEC II PYRAMIDAL CELLS 126

6.1 Introduction 126

6.2 Results 127

6.3 Discussion 132

7. GENERAL DISCUSSION AND FUTURE DIRECTIONS 133

7.1 Two-photon uncaging of MNI-glutamate Dendritic integration in MEC II principal neurons 133

7.2 Dendritic integration in MEC II principal neurons 135

7.3 Dendritic integration under in vivo like membrane potential dynamics 139

7.4 Dendritic integration and grid cell activity 140

7.5 Future directions 141

REFERENCES 143

LIST OF FIGURES

Figure 1.1. Location of HF and PHR in the rat brain 20
Figure 1.2. Location of the HF and the PHR areas in the horizontal cross section 21
Figure 1.3. PHF-HF connectivity..... 22
Figure 1.4 Firing pattern of MEC II grid cells..... 26
Figure 1.5 Grid cell firing in novel environments 27
Figure 1.6 Grid cell firing in the dark and after modifications of the environment visual cues..... 28
Figure 1.7 Grid cells firing after size modification of environment..... 29
Figure 1.8 Co-localized grid cell were shifted in phase 30
Figure 1.9 Dorsoventral gradient in grid spacing..... 31
Figure 1.10 Grid cell phase precession..... 32
Figure 1.11 Grid cells show membrane potential depolarization in grid fields 34
Figure 1.12 Oscillatory interference model of grid cell activity..... 36
Figure 1.13 CAN models of grid cell activity 40
Figure 1.14 Morphology of MEC II stellate cells 42
Figure 1.15 Variability in MEC II stellate cell morphology..... 43
Figure 1.16 Dendritic spines of MEC II stellate cells..... 43
Figure 1.17 Electrophysiological profile of MEC II stellate cells..... 45
Figure 1.18 Morphology of MEC II pyramidal cells 46
Figure 1.19 Variability in MEC pyramidal cell morphology..... 47
Figure 1.20 Dendritic spines of MEC II pyramidal cells..... 47
Figure 1.21 Electrophysiological profile of MEC II pyramidal cells..... 48
Fig. 1.22 Dendritic filtering of EPSPs 53
Fig. 1.23 NMDA and Na^+ spikes in basal dendrites of layer V pyramidal cells..... 57

Figure 2.1 Morphology and electrophysiology of the stellate cell of MEC II 65
Figure 2.2 Morphology and electrophysiology of the pyramidale cell of MEC II 66
Figure 2.3 Creating *in vivo*-like membrane potential dynamics *in vitro* .. 71
Figure 2.4 Measuring dendritic integration on single dendrites of the stellate cells of MEC II 72
Figure 2.5 Identification of a slow dendritic spike 74
Figure 2.6 Identification of a fast dendritic spike by d^2V/dt^2 peak 75
Figure 3.1 MNI-glutamate two-photon uncaging evoked EPSPs were at physiological amplitudes 80
Figure 3.2 Supralinear integration of synaptic inputs in single dendrites of MECII stellate cells 82
Figure 3.3 Some recordings showing saturation of increase in EPSP amplitude 83
Figure 3.4 Supralinearity of dendritic integration in MEC II stellate cells does not depend on dendritic location 86
Figure 3.5 EPSPs evoked in proximal dendrites show a faster rate of rise than distally evoked EPSPs 87
Figure 3.6 Amplitude of EPSPs evoked in different locations of the dendrite 88
Figure 3.7 Supralinearity of dendritic integration does not depend on distance from the soma, EPSP amplitude, number of uncaging spots and spread of them 89
Figure 3.8 The majority of recordings were performed in the ventral half of MEC 90
Figure 3.9 Dendritic integration in MECII stellate cells depends on the time interval between uncaging pulses 92
Figure 3.10 Dendritic integration in stellate cells at different dendritic locations with varying uncaging intervals 94
Figure 4.1 Summary of intrinsic electrophysiological properties of MEC II stellate cells 99

Figure 4.2 Some dendrites exhibit fast dendritic spikes, which are often followed by slow dendritic spikes..... 103
Figure 4.3 Fast and slow dendritic spikes are present only during near-synchronous stimulation 104
Figure 4.4 Fast and slow dendritic spikes can be generated at various locations along the dendrite..... 105
Figure 4.5 Dendritic integration after blocking VGS channels and NMDA receptors..... 105
Figure 4.6 Supralinear dendritic integration is abolished by blocking VGS channels and NMDA receptors..... 107
Figure 4.7 Dendritic spikes are blocked by TTX and APV..... 108
Figure 5.1 Figure 5.1 Generating *in vivo*-like membrane potential dynamics *in vitro*..... 113
Figure 5.2 Uncaging *in vitro* during *in vivo*-like membrane potential dynamics 115
Figure 5.3 Uncaging during *in vivo*-like membrane potential dynamics boosts supralinearity of integrals of EPSPs..... 116
Figure 5.4 Nonlinearity of dendritic integration is significantly larger in terms of integrals but not amplitudes of EPSPs during *in vivo*-like ramps 117
Figure 5.5 *In vivo*-like membrane potential dynamics results in increased occurrence of dendritic spikes..... 118
Figure 5.6 Uncaging on 2 dendrites results in substantially increased supralinearity of dendritic integration..... 119
Figure 5.7 Action potentials could be evoked by uncaging on two dendrites 120
Figure 5.8 Comparison of dendritic integration during stimulation of single or multiple dendritic branches..... 121
Figure 5.9 Near-simultaneous stimulation of inputs on two dendrites .. 123
Figure 5.10 Dendritic integration of inputs on two dendrites 123
Figure 6.1 MEC II pyramidal cells were located within calbindin positive cell patches..... 128

Figure 6.2 MEC II pyramidal cells summate near-synchronous inputs in a supralinear manner..... 129
Figure 6.3 MEC II pyramidal cells and stellate cells summate inputs in a similar manner 130
Figure 6.4 Fast and slow dendritic spikes can be evoked in MEC II Pyramidal cells by near-synchronous stimulation 131

ABBREVIATIONS

AMPA - α -amino-3-hydroxy-5-methyl-4-isoxazolepropionic acid

AMPARs – AMPA receptors

AP – action potential

APV – (2*R*)-amino-5-phosphonovaleric acid (NMDA receptor antagonist)

EPSP – excitatory postsynaptic potential

HCN channels – hyperpolarization-activated cyclic nucleotide mediated channels

HF – fippocampal formation

I_h current – hyperpolarization-activated current

MEC – medial entorhinal cortex

MEC II – medial entorhinal cortex layer II

mEPSPs – miniature EPSPs

NMDA – N-methyl-D-aspartate

NMDARs –NMDA receptors

PHR – parahippocampal region

TTX – tetrodotoxin (sodium channel blocker)

VGSC – voltage-gated sodium channels

ZD7288 – HCN channel blocker

1. INTRODUCTION

The hippocampal formation (HF) and parahippocampal region (PRH) has long been proposed to play a role in various functions, including episodic memory (Lipton & Eichenbaum, 2008) and spatial navigation (O'Keefe, 1976). The hippocampal formation consists of the canonical hippocampal area (e.g. CA1-CA3), dentate gyrus (DG) and subiculum. The parahippocampal region (PHR) contains the presubiculum, parasubiculum and entorhinal cortex, which is traditionally divided into medial and lateral parts (MEC and LEC, respectively) (Witter et al., 2000).

Two landmarks in hippocampal research were the discoveries of place cells in the hippocampus (O'Keefe & Dostrovsky, 1971) and grid cells in the medial entorhinal cortex (MEC) (Hafting et al., 2005), which provided a possible neural basis for spatial representation in the brain. The importance of these findings has been marked by the award of the Nobel Prize in Medicine or Physiology 2014 for three scientists who played key roles in these discoveries: John O'Keefe, Edvard Moser and May-Britt Moser (Nobel Media AB 2014, 2014).

The work of John O'Keefe demonstrated that a given hippocampal place cell is active at a particular location in space (O'Keefe, 1976). The Mosers' research group revealed that entorhinal grid cells are active at multiple locations with regular intervals in space, giving rise to a grid-like arrangement of firing fields (Fyhn et al., 2004; Hafting et al., 2005). In contrast to place cells, grid cell firing is stable within the same environment, even if visual cues are altered or completely absent (Hafting et al., 2005). Moreover, grid cell hexagonal firing parameters: angle, phase and spacing, are maintained across different environments

(Hafting et al., 2005). Therefore, grid cells have been proposed to be key players in self motion based navigation, commonly referred to as path integration (McNaughton et al., 2006; Hafting et al., 2005).

While several theoretical models have been developed to explain how this canonical pattern of grid cell firing arises from intrinsic cellular conductances, network connectivity and synaptic activity (Burgess, 2008; Burgess et al., 2007; Hasselmo et al. 2007; McNaughton et al., 2006), the intrinsic mechanisms mediating grid cell activity remain poorly understood. We have therefore performed a thorough analysis of the cellular properties of grid cells, in particular how they integrate inputs arriving to their dendritic tree, as well as how these inputs are converted into somatic action potential output. Moreover, we have used the results of this work to refine some of the traditional theoretical models of grid cell firing to understand how the cellular properties we observed may enable canonical grid cell activity.

In this chapter, I will briefly review the anatomy and connectivity of the hippocampal formation and parahippocampal region (Chapter 1.1). Later I will discuss the properties of the grid cells (Chapter 1.2) and theoretical models proposed to explain grid cell activity (Chapter 1.3). I will then discuss the morphology and electrophysiology of principal neurons of MEC II (Chapter 1.4), where grid cells have been found. Then, I will review the phenomenon called dendritic integration (Chapter 1.5). At the end of this chapter I will propose my hypothesis, which leads to the research presented in this thesis (Chapter 1.6).

1.1 Hippocampal formation and parahippocampal region

In this chapter I will briefly cover anatomy, connectivity and functional role of hippocampal formation (HF) and parahippocampal region (PHR).

1.1.1 HF and PHR anatomy

The entorhinal cortex (EC), which is divided in medial and lateral parts, (MEC and LEC) is part of a 6-layered structure called the parahippocampal region (PHR). The parahippocampal region also contains the presubiculum, parasubiculum, perirhinal cortex (PER) and postrhinal cortex (POS) (Fig. 1.1 and Fig. 1.2) (van Strien, Cappaert, & Witter, 2009). The PHR is adjacent to the hippocampal formation (HF), a 3-layered structure that is divided into the hippocampus proper (HP; CA1, CA2 and CA3 regions), dentate gyrus (DG) and the subiculum (van Strien et al., 2009). The PHR and HF are situated in the caudal part of the brain (Fig. 1.1) and are abundantly interconnected (Fig. 1.3).

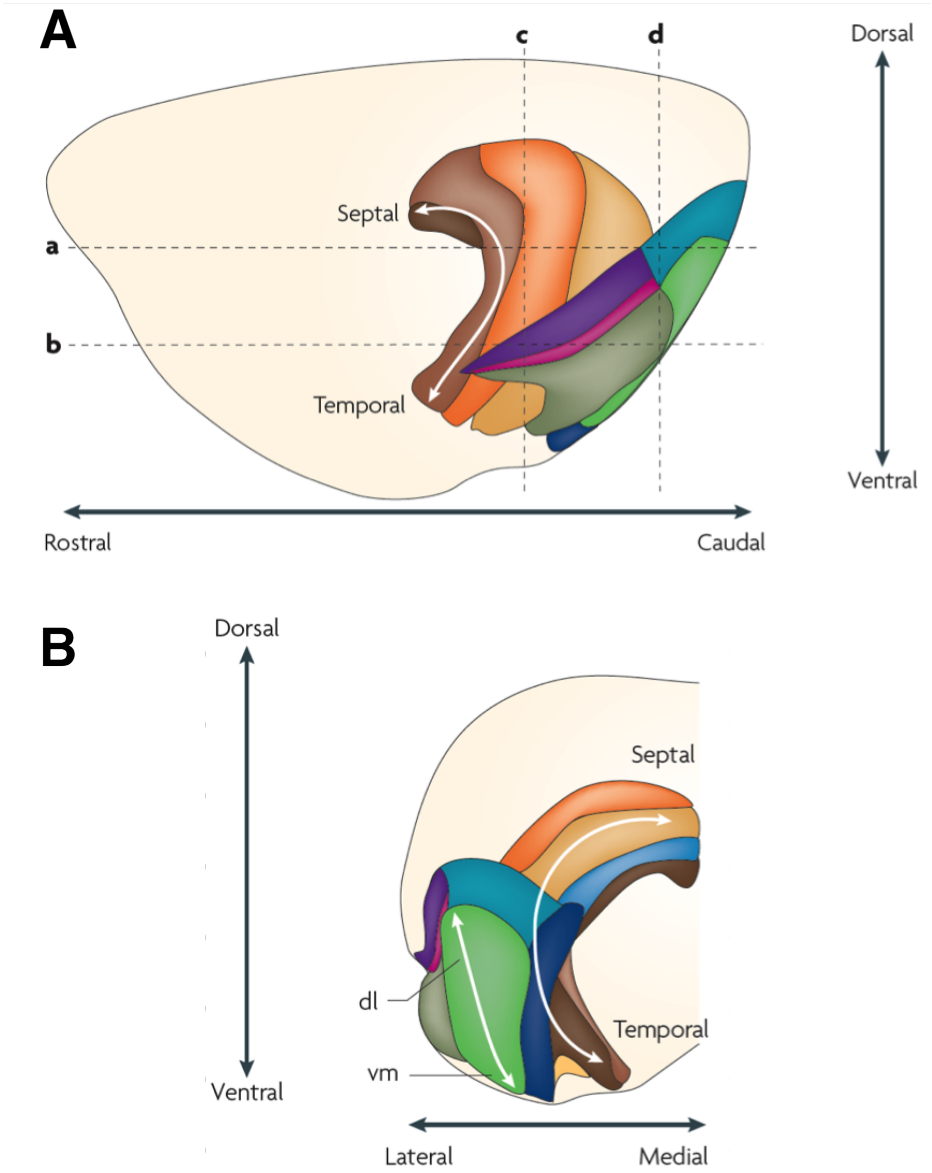

Figure 1.1. Location of HF and PHR in the rat brain

Lateral (**A**) and caudal (**B**) view of the rat brain with areas of HF and PHR coloured. HF: dentate gyrus (DG) – dark brown, CA3 – medium brown, CA1 – orange, subiculum – yellow. PHR: presubiculum (PrS) – medium blue, parasubiculum (PaS) – dark blue, lateral entorhinal cortex (LEC) – dark green, medial entorhinal cortex (MEC) – light green, perirhinal cortex Brodmann areas 35 and 36 – pink and purple, respectively, postrhinal cortex (POR) – turquoise. (Adapted from (van Strien et al., 2009))

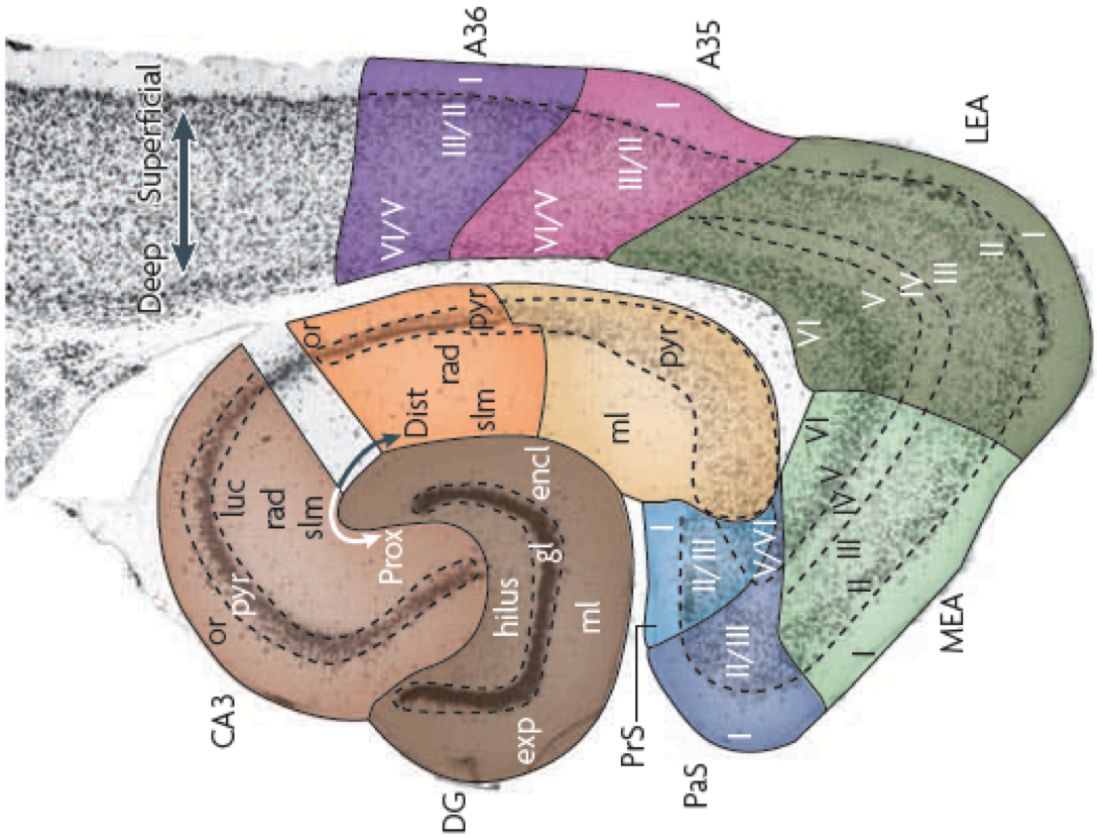

Figure 1.2. Location of the HF and the PHR areas in the horizontal cross section

Horizontal Nissl-stained section, from the location marked "b" in Fig. 1.1A with brain areas and layers indicated. Colour code represents the same areas as in Fig. 1.1. (Adapted from (van Strien et al., 2009))

1.1.2 HF and PHR connectivity

Information from the neocortex is sent to the parahippocampal region (PHR). The PHR is the main input to the hippocampal formation (HF) (Fig. 1.3). EC receives input from the presubiculum (PrS), and in addition, lateral entorhinal cortex (LEC) and medial entorhinal cortex (MEC) receive selective inputs from the perirhinal cortex (PER) and postrhinal cortex (POR), respectively (Fig. 1.3).

The entorhinal cortex (EC) sends inputs to the PER and the POR. MEC and LEC layer II project to the dentate gyrus (DG) and CA3, and layer

III to CA1 and the subiculum (Sub). Also, DG connects to CA3 via mossy fibres, CA3 to CA1 via Schaffer collaterals and CA1 to Sub. CA1 and Sub target EC layers V/VI.

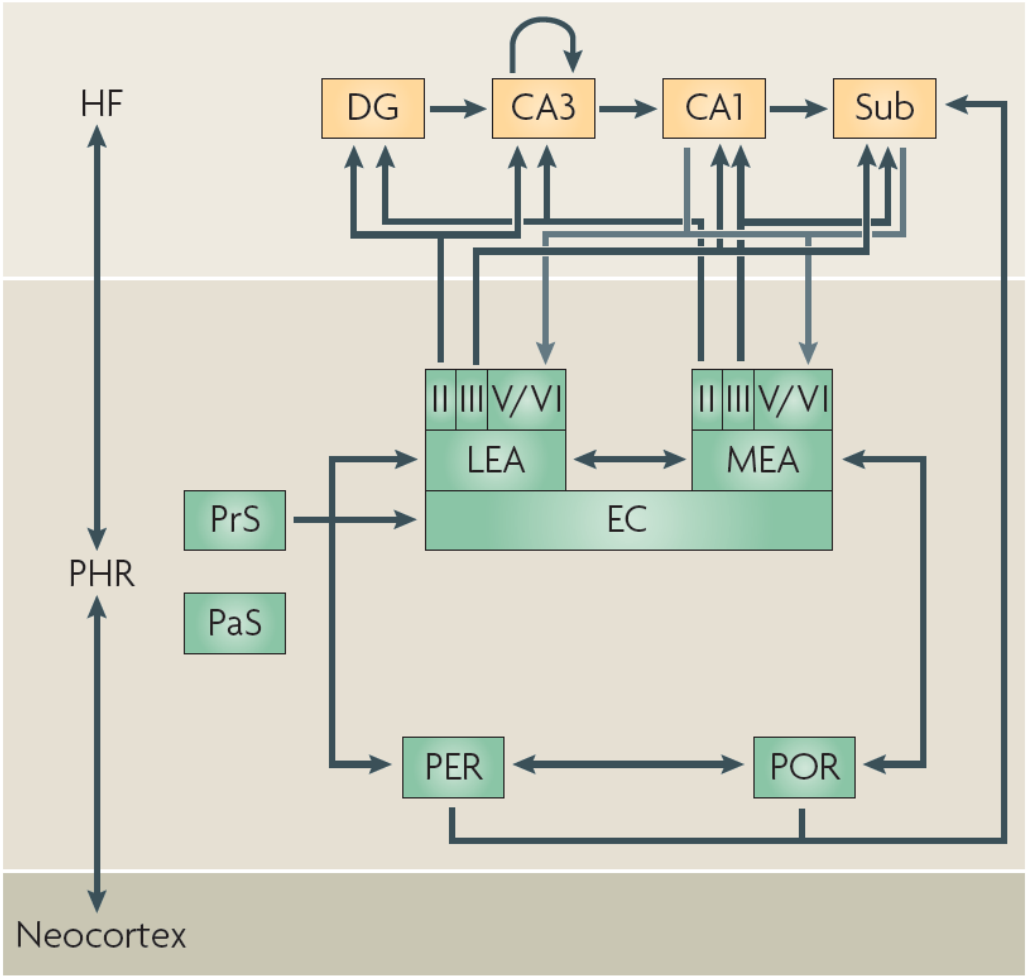

Figure 1.3. PHF-HF connectivity

Schematic diagram of areas within the HF and PHR and prominent connections between them. (Adapted from (van Strien et al., 2009))

1.2 Grid cells

10 years ago Edvard and May-Britt Mosers' group has found MEC layer II neurons with regular firing fields in 2D space forming hexagonal pattern, hence their name grid cells (Fyhn et al., 2004; Hafting et al., 2005). Strikingly periodic grid cell firing fields drawn interest from experimentalists and theoreticians of various research groups which resulted in a large number of further discoveries describing grid cell properties and the proposal of a few theoretical models to explain the mechanisms underlying their activity. In the subsequent studies grid cells have been not only in layer II but also in layer III and deeper layers (V and VI) of MEC (Sargolini et al., 2006), as well as in parasubiculum and postsubiculum (Boccara et al., 2010). Beside the initial studies of grid cells in rats (Fyhn et al., 2004; Hafting et al., 2005), they have also been found in mice (Fyhn et al., 2008), humans (Doeller et al., 2010) and bats (Yartsev at al., 2011).

Grid cell function is still somewhat controversial. However, most studies are suggesting that grid cells are likely to be a neuronal basis of allocentric representation of self-location in the environment (Hafting et al., 2005). Grid firing fields are thought to be generated based on self-motion information and maintained via the inputs from the hippocampal place cells, since grid cell activity is compromised after pharmacological inactivation of hippocampus (Bonnevie et al., 2013). However, recent study of rats navigating in trapezoid shaped environment suggest that activity of grid cells is shaped by the geometry of environment, therefore cannot provide a universal metrics in all environments (Krupic et al., 2015). Alternative hypothesis suggests that grid cells might be important for goal directed navigation (Erdem and Hasselmo, 2012), what still needs to be tested.

In this chapter I will cover the properties of grid cell firing activity and in the following one – the proposed theoretical models of how grid cell firing fields are being formed.

1.2.1 Firing properties

Tetrode recordings from the MEC II of navigating rats revealed that grid cells were active in multiple locations of the environment, covering all the space in a grid like pattern (Hafting et al., 2005). The hexagonal regularity of the adjacent firing fields of the cell is commonly assessed by calculating a spatial autocorreliogram in the rotations of 30, 60, 90 120 and 150 degrees (Hafting et al., 2005). The gridness score is then calculated as a difference between minimum correlation coefficient for rotations of 60 and 120 degrees and maximum correlation coefficient for rotations of 30, 90 and 150 degrees (Hafting et al., 2005).

The gridness of each cell was maintained between environments even if they differed in size (Fig. 1.4) or were novel to the animal (Fig. 1.5A) (Hafting et al., 2005). However, grid scale was larger in the new environments and gridness score lower, which was improved as the animal became more familiar with the environment (Fig. 1.5 B and C) (Barry et al., 2012). Moreover, even though in novel environments grid scale is roughly preserved, however orientation and offset relative to the environment are not (Barry et al., 2012). This challenges the idea of grid cells being the universal metrics of space, and suggests that dynamics between self-motion and grid representation is more complex (Barry et al., 2012).

The grid firing was maintained if the visual cues of the environment were eliminated (Fig. 1.6A). The grids were locked to environment features, which changed the orientation but not scaling or firing rate of the cell (Fig. 1.6B). Changing the size of the environment preserved the

gridness of the firing, however, spacing between active fields was stretched or compressed correlating with the modification of the environment (Fig. 1.7). Grid cells from the same location in the MEC II had the same grid scaling and were out of phase with each other, so that the firing fields of as little as 3 cells could cover the whole environment (Fig. 1.8).

Grid cells from different locations in the MEC II differed in the spacing of the grid firing fields, with the dorsal neurons having the smallest spacing and the ventral ones the largest, thereby forming a dorsoventral gradient of grid spacing (Fig. 1.9) (Hafting et al., 2005). Grid cells cluster into small number of discrete modules with distinct scale, orientation and theta frequency modulation (Stensola et al., 2011) possibly originating from self-organizing network dynamics (Pilly and Grossberg, 2014). These topological modules are functionally autonomous since scale, offset and orientation relative to other grids in same module is preserved in novel environments (Barry et al., 2012).

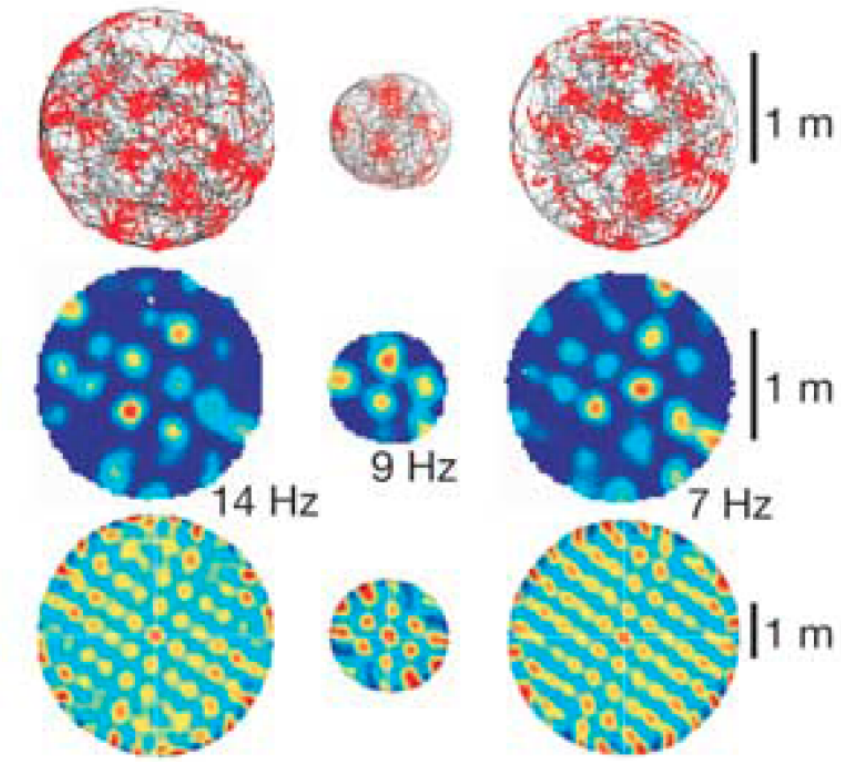

Figure 1.4 Firing pattern of MEC II grid cells

MEC II grid cells were active in multiple locations of the environment forming a hexagonal pattern and this pattern is maintained across enclosures that differ in size. Action potentials (red dots) plotted on the animal running trajectory (black) (top row), firing rate map (middle row) and autocorrelation map (bottom row). (Adapted from (Hafting et al., 2005))

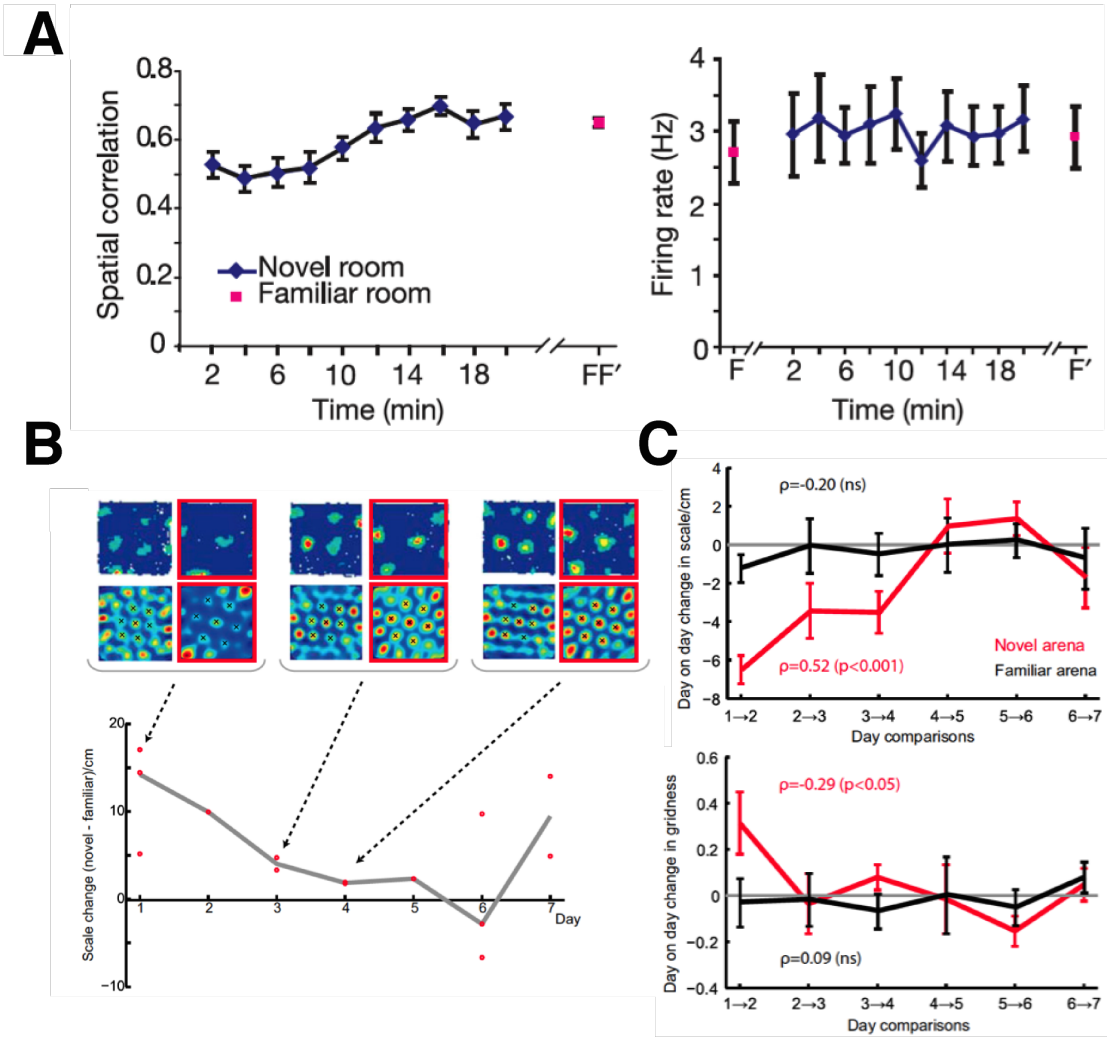

Figure 1.5 Grid cell firing in novel environments

Grid cells expressed grid patterns in novel environments; however, grid scale and gridness change over days. **A**. Plots of spatial correlation and firing rate (mean ± SEM) against time reveal that grids are formed immediately as an animal explores an environment. (Adapted from (Hafting et al., 2005)) **B**. Grid spacing is larger in novel environments (red squares) compared to familiar ones and decreases to the baseline as the animal familiarizes itself with the environment over a period of days. (Adapted from (Barry et al., 2012)) **C**. Grid scale keeps changing over first 4 days as an animal is exploring a novel environment, while it does not change in the familiar environment (top panel). Gridness improves most within the first 2 days during exploration of a novel environment and does not change in a familiar environment. (Adapted from (Barry et al., 2012))

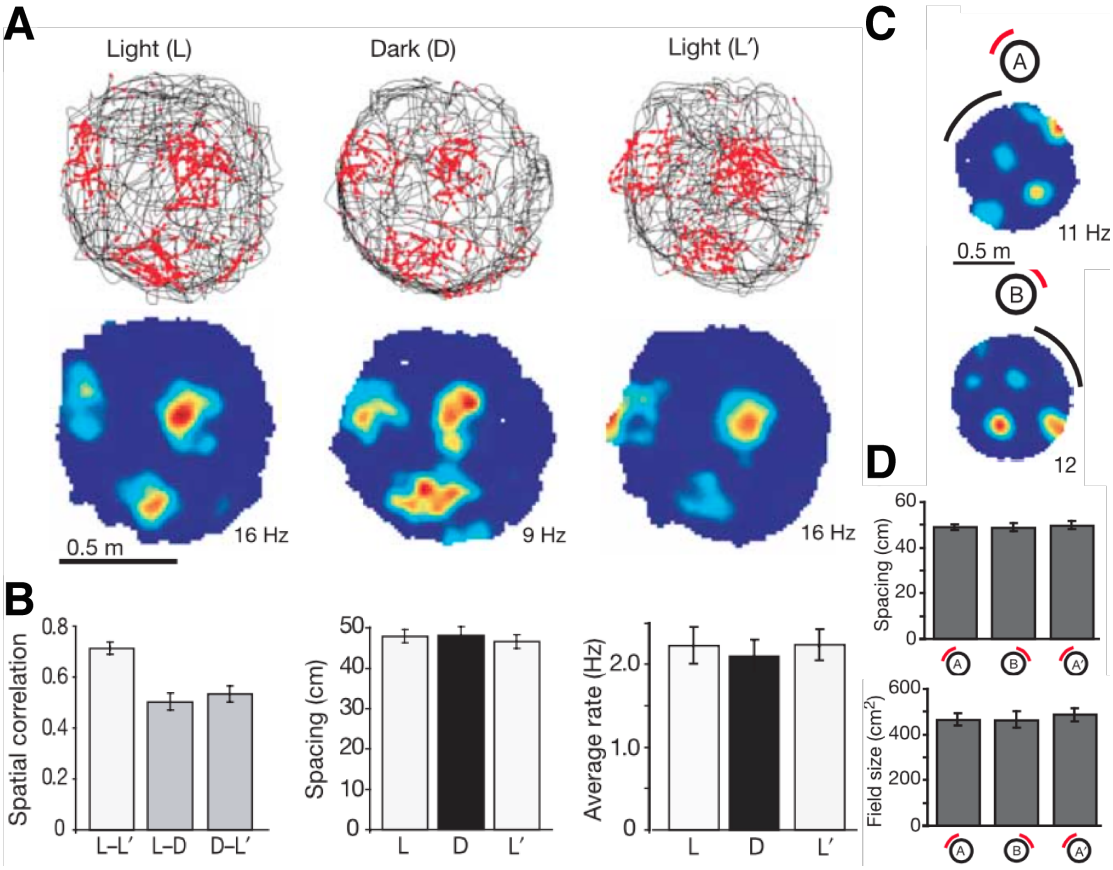

Figure 1.6 Grid cell firing in the dark and after modifications of the environment visual cues

A. Grid cells maintained their firing pattern in the dark. Trajectory (black line) with action potentials (red dots) (top panel) and the firing rate maps (bottom panel) for 10 mins before the onset of darkness (left panel), 10 mins during darkness (middle panel) and 10 mins after darkness (right panel). **B.** Spatial correlation, grid spacing and firing rate were comparable before, during and after the onset of darkness. **C.** Grid cell firing rate maps in a familiar environment (A) and after rotation of cue card by 90° (B). **D.** Grid spacing and field size remained the same after the rotation of the cue card. (Adapted from (Hafting et al., 2005))

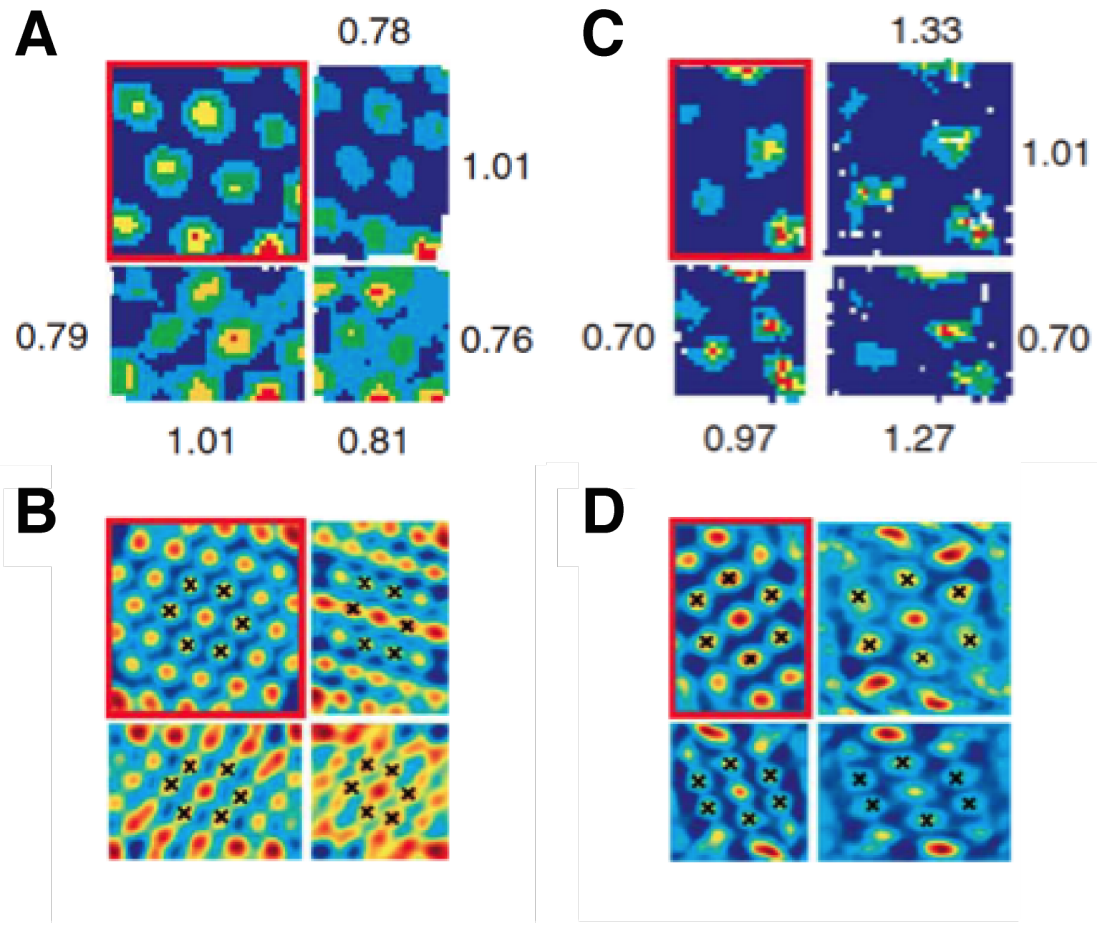

Figure 1.7 Grid cell firing after size modification of environment. Grid cells rescale in response to modifications of the size of the environment. Firing rate maps (A and C) and spatial autocorrelograms (B and D) in 2 different environments (outlined by red square and rectangle in left and right panels, respectively) and in the modifications of them. Environments were scaled in size in either x (right of the original environment), y (bottom of the original environment) or both axes (right bottom corner) in each panel. Numbers in A and C indicate the proportion of the environment's original size in that axis. (Adapted from (Barry et al., 2007))

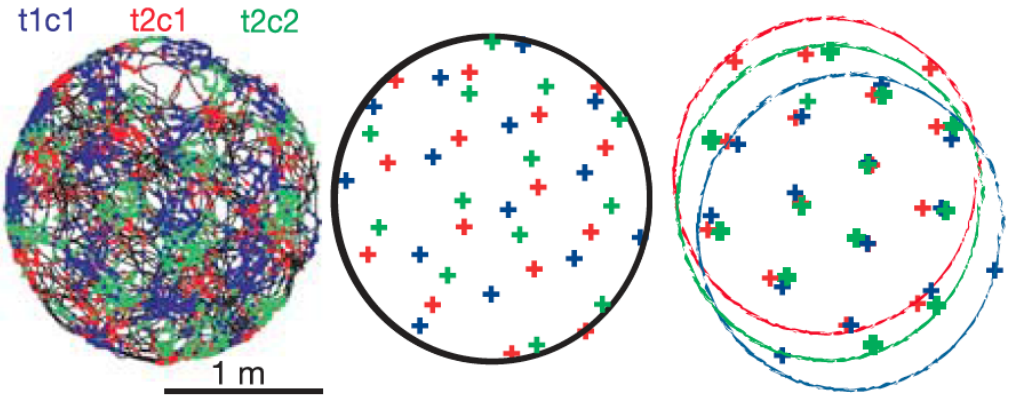

Figure 1.8 Co-localized grid cells were shifted in phase

Grids of 3 cells represented by different colours on top of the animal trajectory (left panel). Locations of peaks of firing fields indicated in coloured "+" for each cell (middle panel). Different cells have similar grid size and orientation (right panel), grids are illustrated offset for better comparison. (Adapted from (Hafting et al., 2005))

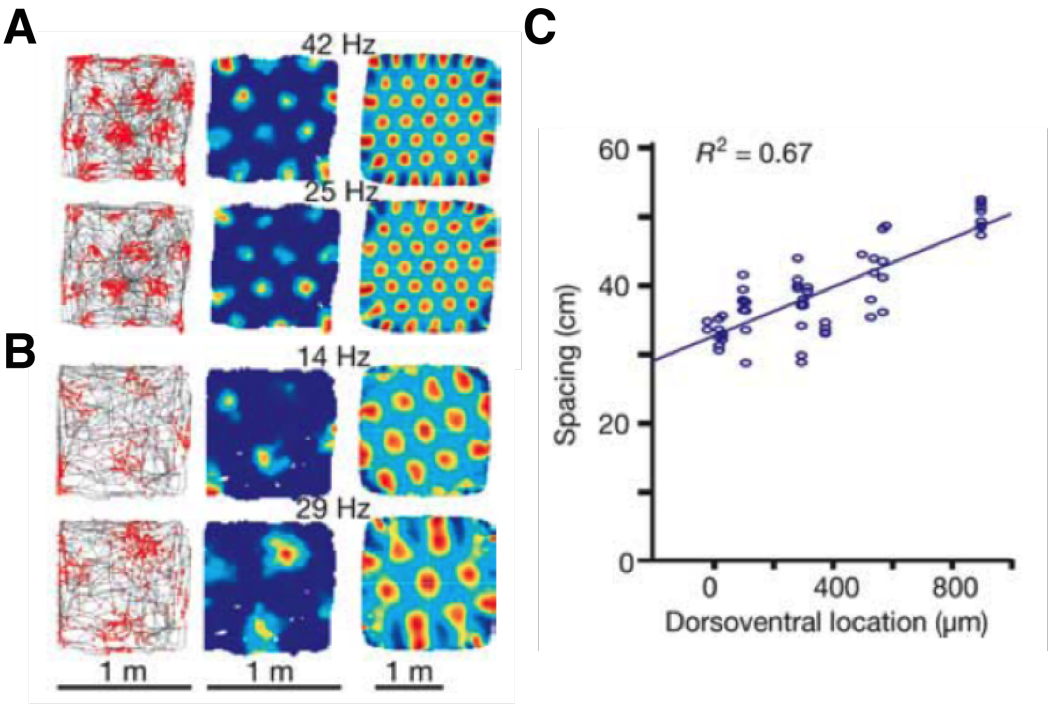

Figure 1.9 Dorsoventral gradient in grid spacing

Grid cells show a dorsoventral gradient in grid spacing.

A. Recording from a grid cell in the dorsal part of MEC. **B.** Recording from a grid cell in the ventral part of MEC. **C.** Grid spacing correlates with the dorsoventral location of a cell within MEC. (Adapted from (Hafting et al., 2005))

1.2.2 Phase precession

Network oscillations at theta frequency (4-11 Hz) found in both hippocampus and medial entorhinal cortex and have been suggested to play an important role in memory (Mizumori et al., 1990, Givens et al., 1994). Moreover, both hippocampal place cells (O'Keefe & Recce, 1993) and MEC grid cells (Hafting et al., 2008) code space by action potential firing occurring at increasingly earlier phases of the theta rhythm of the local field potential while the animal crosses a firing field, what is called theta phase precession (Fig. 1.10).

Some of the models propose that network theta oscillations are essential for formation of spatial periodicity of grid cells (Burgess et al., 2007, Burgess et al., 2008). In agreement with that spatial scale of grid cell firing correlates with frequency of inner rhythmicity along the dorsoventral axis of MEC (Hafting et al., 2005, Garden et al., 2008). Moreover, ablating theta rhythm oscillations in hippocampus and entorhinal cortex by pharmacological inactivation of medial septum resulted in disrupted grid cell spatial periodicity (Brandon et al., 2011).

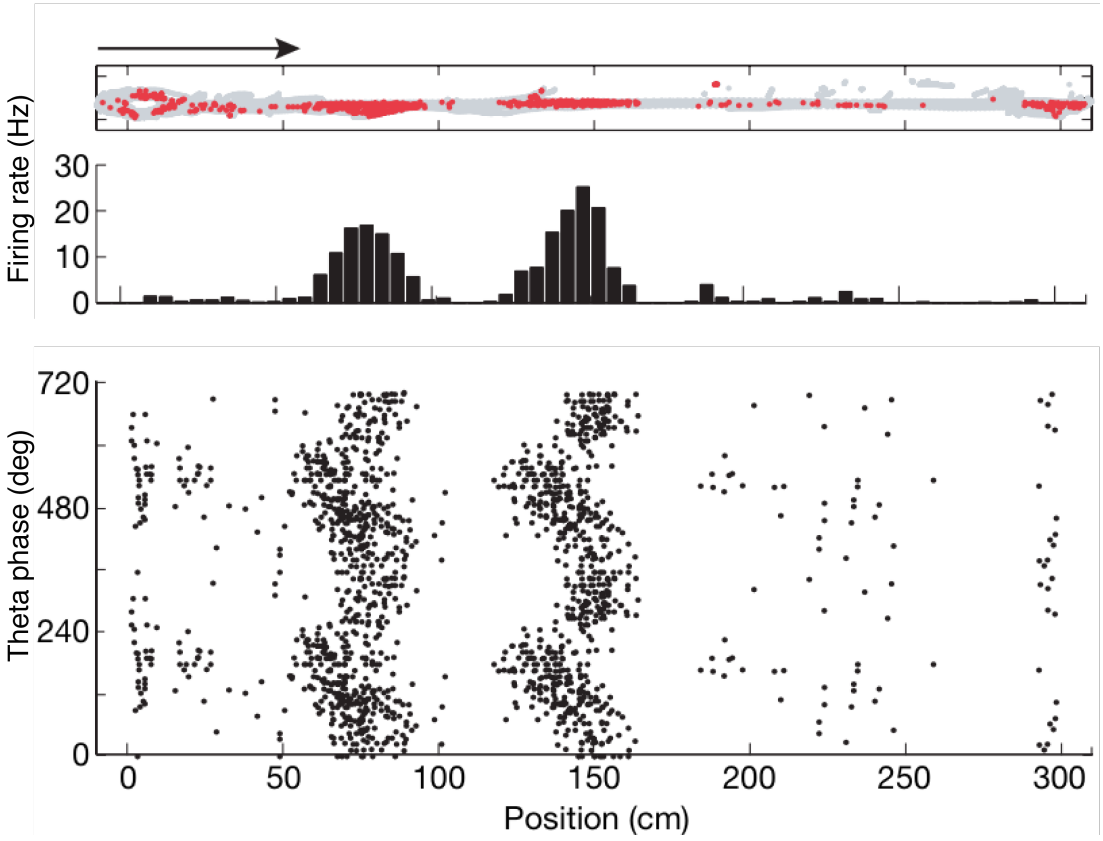

Figure 1.10 Grid cell phase precession

Grid cells exhibit phase precession of action potentials with respect to LFP theta. (Adapted from (Hafting et al., 2008))

1.2.3 Membrane potential dynamics

Cells showing grid-like firing have also been found in mice navigating along a 2D virtual linear track (Domnisoru, Kinkhabwala, & Tank, 2013; Schmidt-Hieber & Hausser, 2013), enabling whole cell patch clamp recordings of grid cells, which led to the discovery of membrane potential dynamics of grid cells in behaving animals. Theta membrane potential oscillations were found in MECII stellate cells during animal motion but not at rest (Schmidt-Hieber & Hausser, 2013). Both action potentials and membrane potential oscillations (MPOs) showed phase precession with respect to simultaneously recorded LFP theta during firing field crossings (Fig. 1.19 B). Moreover, as the animal was crossing a firing field, membrane potential depolarized in a ramp-like manner with action potentials riding on top of it (Fig. 1.11 A and C) (Domnisoru et al., 2013; Schmidt-Hieber & Hausser, 2013).

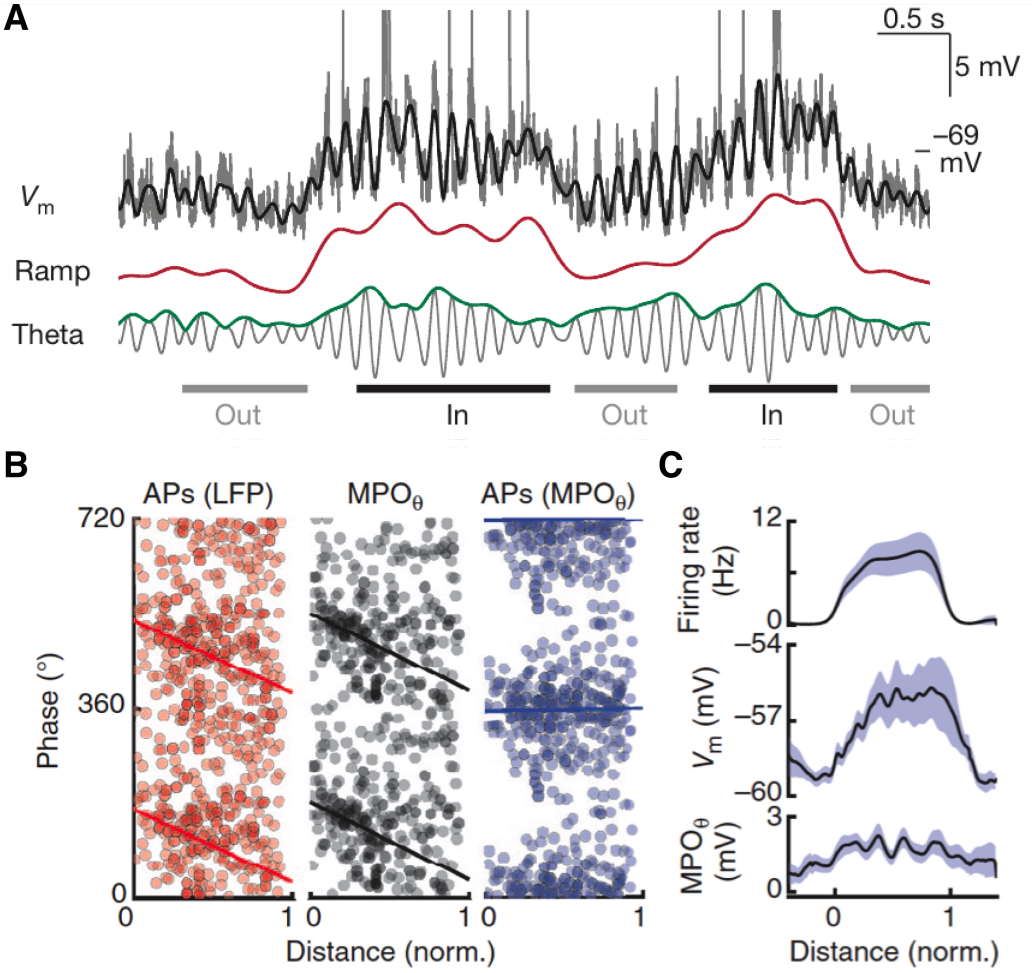

Figure 1.11 MECII principal neurons show sustained membrane potential depolarizations during grid field crossings

A. Membrane potential dynamics with spikes clipped (grey, top panel) as an animal was running through a grid field of a cell can be decomposed into a depolarizing ramp (red) and a theta component (grey, bottom panel). The sum of them (black, top panel) approximates the unfiltered membrane potential trace (grey, top panel) (Adapted from (Domnisoru et al., 2013)) **B.** Phase of action potentials (left panel) and membrane potential oscillations (MPO) (middle panel) with respect to LFP theta and action potentials with respect to MPOs. (Adapted from (Schmidt-Hieber & Hausser, 2013)) **C.** Average (black) ± SEM (coloured area) firing rate (top panel), membrane potential oscillations (middle panel) and MPOs against normalized position in a firing field. (Adapted from (Schmidt-Hieber & Hausser, 2013))

1.3 Grid cell models

A number of theoretical models have been created to explain grid cell activity. These models fall into 2 main classes: oscillatory interference and attractor network models. The first class, oscillatory interference (OI) models use interference of different membrane potential oscillations to explain grid-like firing (Burgess et al., 2007). The second class, continuous attractor network (CAN) models use activity shift in a recurrently connected network of cells to generate a grid-like pattern. In this chapter I will briefly discuss both classes of models, how well they fit the experimental data and the predictions they make.

1.3.1 Oscillatory interference models

The oscillatory interference (OI) model was originally proposed to explain firing pattern and phase precession of place cells (O'Keefe & Burgess, 2005) and later modified for grid cells (Burgess et al., 2007; Burgess, 2008). This model describes grid cell activity resulting from interference of oscillations with different frequencies, where the soma is constantly oscillating at a theta frequency, and the dendrites at a frequency that depends on animal speed and direction (velocity-controlled-oscillators (VCOs); Fig. 1.12) (Burgess et al., 2007). Computational studies have suggested that multiple VCOs (at least 3), with preferred directions differing by 60º project onto a grid cell, resulting in a stable grid-like spatial firing pattern that is relatively robust to noise (Burgess et al., 2007).

VCOs were originally proposed to be implemented in the dendrites (Burgess et al., 2007), however, it has been found that due to biophysical limitations, oscillations within the same cell soon phase-lock (Remme et al., 2010). To overcome this obstacle VCOs were moved to other cells projecting to separate dendrites of one cell in the second generation of

OI models (Burgess, 2008; Giocomo & Hasselmo, 2008; Hasselmo, 2008). Second class of OI model predicts the existence of velocity-controlled oscillators, which have been found in anterior thalamus, medial septum and hippocampus (Welday et al., 2011).

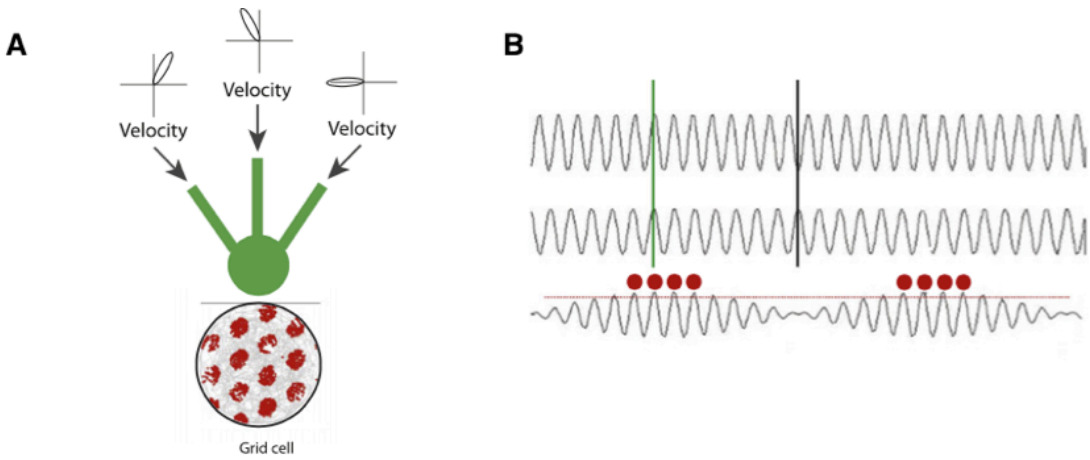

Figure 1.12 Oscillatory interference model of grid cell activity
A. Top: Schematic drawing of the oscillatory interference model of grid cells, where velocity-modulated inputs with different preferred head-direction angles, offset by 60° from one another, project to separate dendrites. Bottom: grid cell pattern produced by oscillatory interference model. **B.** An example of a single dendritic oscillation (top) and somatic oscillation (middle) generating an interference pattern (bottom). When in phase (green) interference of these oscillations increases in amplitude and action potentials are generated (red dots), when it crosses the threshold (red line). (Adapted from (Giocomo et al., 2011))

OI model predicts that grid cells exhibit membrane potential oscillations at around theta frequency, what has been observed in the stellate cells of MEC II (Alonso & Klink, 1993), where majority of grid cells have been found. Secondly, it predicts that theta oscillations are necessary for grid cell activity, which has also been well supported by experimental data. Inactivation of medial septum which disrupts the global theta rhythm resulted in disrupted periodicity of the grid firing (Brandon et al., 2011).

OI models also predict grid expansion to originate from the decrease in theta frequency. There are two lines of experimental evidence to support it. Firstly, increase in grid scale at the dorsoventral axis was found to correlate with decrease in frequency of subthreshold oscillation and intracellular properties of MEC II stellate cells (Giocomo et al., 2007, Garden et al., 2008). Moreover, the frequency of the theta rhythm was found to be more sensitive to changes in running speed in dorsal compared to ventral MEC (Jeewajee et al., 2008). Secondly, both grid expansion and decrease in LFP theta frequency oscillations was found in animals exploring novel environments (Barry eta al., 2012). Moreover, oscillatory interference models inherently explain how grid cell phase precession is formed and maintained with high accuracy in *in vivo* (Hafting et al., 2008).

One obstacle originates from recent findings of grid cells in crawling and flying fruit bats, which do not exhibit theta oscillations in LFP recordings in hippocampus and entorhinal cortex (Yartsev et al., 2011, Ulanovsky and Yartsev, 2011), however crawling bats had low movement speed and low firing rates and flying bats had wing movement artefacts at theta frequency making it difficult to assess for certain if no theta oscillations were detected during the movement at speeds comparable to rodent data.

Another obstacle for OI models lies in the high level of noise and the variability of frequencies in biological oscillators (Dudman & Nolan, 2009; Giocomo & Hasselmo, 2008), which would readily disrupt grid patterns resulting from the OI model (Welinder, et al., 2010). Noise induced drift might be reset by sensory inputs as an animal explores the environment, but that is yet to be explored. To increase OI robustness, a third class of OI models have been created where oscillators, located in separate cells projecting to different dendrites, are coupled by excitatory

and inhibitory connections (Zilli & Hasselmo, 2010), however, it yet remains to be found if these networks exist in the MEC.

1.3.2 Continuous attractor network models

Another class of models, called continuous attractor network (CAN) models, explains grid pattern formation by a velocity-dependent shift of periodic activity bumps in a network of recurrently connected neurons during spatial navigation (Fig. 1.13A). These packets of activity bumps in the flat neuronal activity landscape are shifted by inputs from speed modulated head direction cells or grid cells with head direction cell properties (conjunctive cells) (Fuhs & Touretzky, 2006, McNaughton et al., 2006). So first prediction CAN models make is the existence of these velocity-modulated cells, which in fact have been found in deeper layers of MEC, parasubiculum and postsubiculum with anatomical connections MEC layer II where majority of grid cells have been found (Sargolini et al., 2006, Witter & Moser, 2006). Grid spacing expansion found in animals exploring novel environments (Barry et al., 2012) can potentially be achieved by the change in activity of these cells driving the activity shift within the recurrently connected network of grid cells.

The second prediction CAM models make is topographical clustering of cell with the same grid scale and orientation, which also has been found (Barry et al., 2007). Moreover, recent study of functional cellular-resolution imaging of rats navigating in virtual environment demonstrated that grid cells are arranged in topographical clusters with the distance dependent correlation of activity with grid cells closer to each other having more similar spatial firing phase than those further apart (Heys et al., 2014).

Another prediction attractor network models make is the existence of recurrent connectivity between grid cells. Initially CAN models were

created with recurrent excitatory connectivity (Conklin & Eliasmith, 2005; Samsonovich & McNaughton, 1997), however, paired recording between MEC neurons *in vitro* reported that this connectivity pattern is not common in the MEC II (Dhillon & Jones, 2000). It is not clear yet though if potential connections have been disrupted by the slicing procedure since recording from anesthetized mice revealed connectivity between a small fraction of MEC II neurons (Quilichini et al., 2010). Later implementations of CAN models showed that grid cell firing pattern can be achieved also via inhibitory connections between grid cells (Fig. 1.13B) (Burak & Fiete, 2009). And in fact a study of whole-cell patch clamp recordings *in vitro* from more than 600 neuron pairs revealed that MEC II stellate cells are not directly interconnected by excitatory synapses, but MEC II principal neurons are strongly interconnected by interneurons (Couey et al., 2013). However, recent study using optogenetics and tetrode recording in mice revealed that parvalbumin-expressing interneurons in MEC shown no spatial periodicity and receive inputs from grid cells of various phases, causing broadly tuned spatial firing fields, therefore not likely to create phase-dependent recurrent connectivity needed for CAN models (Buetfering et al., 2014). Therefore more work is needed to assess if the CAN models could provide a realistic explanation for grid cell firing

CAN models can create robust grid firing even in the presence of noise (Burak & Fiete, 2009), however, they do not inherently explain phase precession observed in grid cells (Hafting et al., 2008). Phase precession has been achieved in a model of two interconnected networks, with a conjunctive cell layer that generates theta rhythm, and an integrate and fire grid cell layer with realistic intracellular current dynamics (after-spike hyperpolarization and NMDA conductances) (Navratilova et al., 2011).

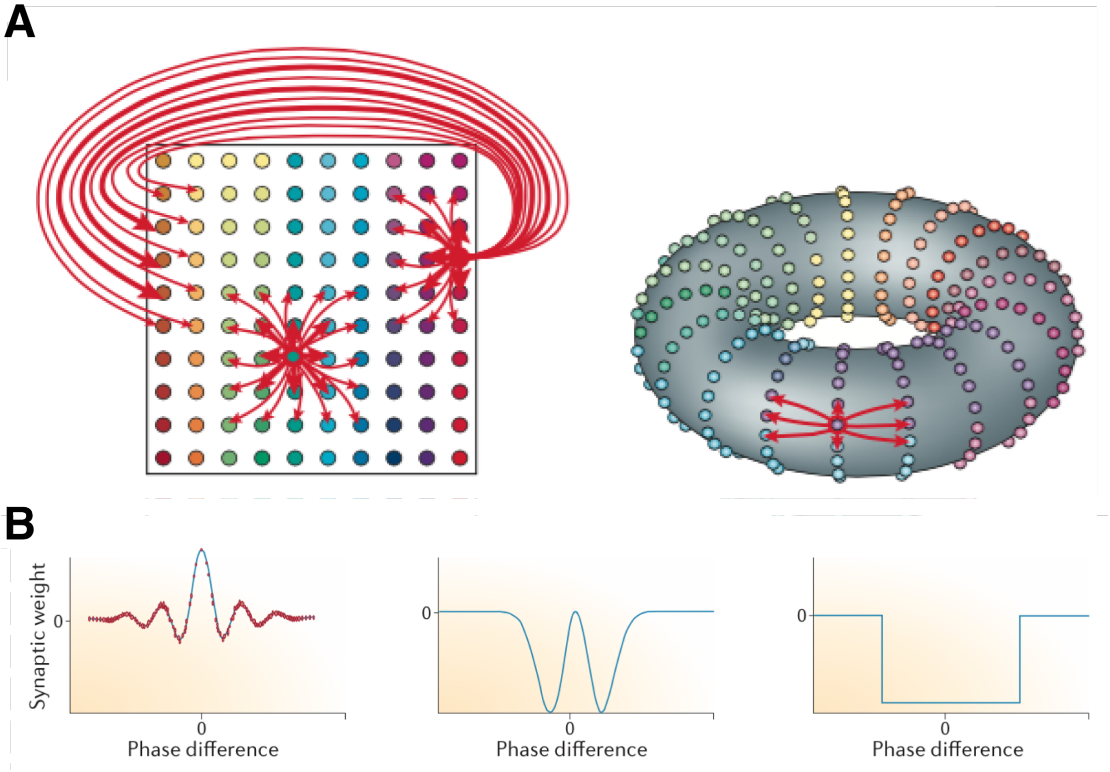

Figure 1.13 CAN models of grid cell activity

A. CAN models explain grid cell firing by a velocity-dependent shift of periodic activity bumps in a recurrently connected neural sheet. Left: neural sheet of interconnected cells, where coloured circles represent individual cells, warm colours represent high firing rate. Right: Solving boundary problem of the neural sheet gives rise to the toroidal topology of the network. (Adapted from (McNaughton et al., 2006)) **B.** Different connectivity patterns have been used in CAN models to generate grid-like firing. Left: Mexican hat connectivity, used by (Fuhs & Touretzky, 2006); middle: Mexican hat-like connectivity, used by (Burak & Fiete, 2009); and step-like inhibitory connectivity, used by (Couey et al., 2013). (Adapted from (E. I. Moser et al., 2014))

1.4 MEC II cell types

Grid cells were initially found in layer II of the medial entorhinal cortex (MEC II) (Fyhn et al., 2004; Hafting et al., 2005). Later research discovered grid cells, with head direction cell properties, in the deeper layers of MEC (Sargolini, 2006), and pre- and parasubiculum (Boccara et al., 2010). However, most putative grid cells have been found in MEC II. Therefore, in this chapter I will cover morphology and electrophysiology of MEC II principal neurons.

MEC II consists of 2 main types of principal neurons: stellate cells and pyramidal cells, the proportion of which seems to be species specific. MEC II of rats contain 38 % ovoid stellate cells, 29 % polygonal stellate cells and 17 % pyramidal cells (Gatome, Slomianka, Lipp, & Amrein, 2010). Mice MEC II contains 52 % ovoid stellate cells, 22 % polygonal stellate cells and 14 % pyramidal cells (Gatome et al., 2010). These cells exhibit vast variability in morphology (Canto & Witter, 2011). The remaining small fraction of cells are horizontal bipolar and tripolar cells, which are not very common in MEC II, thus will not be discussed here.

1.4.1 Stellate cells

Stellate cells have 23 x 13 μm rhomboidal, trapezoid or oval shape soma with elongation positioned perpendicular to the pia within the superficial third of layer II (Fig. 1.13) (Klink & Alonso, 1997). SCs usually have 5 thick primary dendrites (although this number can range from 4-8). Dendrites vary from 2.3 – 4.5 μm and 5.6 – 7.6 μm in diameter for the ones which rise in the surface further from layer I and the surface closer to layer I, respectively, or are uniform diameter (5 – 6 μm) when measured at the base (Klink & Alonso, 1997). (Fig. 1.14) (Klink & Alonso, 1997). The morphology of these cells vary, correlating with their location within layer II (Fig. 1.15) (Klink & Alonso, 1997). The main

dendrites directed towards layer I are elongated (often reaching the pial surface) and divert widely (310 – 720 μm apart in the medio-lateral axis) forming a V-shape dendritic arbour (Klink & Alonso, 1997). Basal dendrites also divert widely but to a lesser extent, ranging 120 – 350 μm in medio-lateral axis. SC dendrites gradually taper and are evenly covered in well-pronounced dendritic spines with a distinct head and a long, thin neck (Fig. 1.16) (Klink & Alonso, 1997).

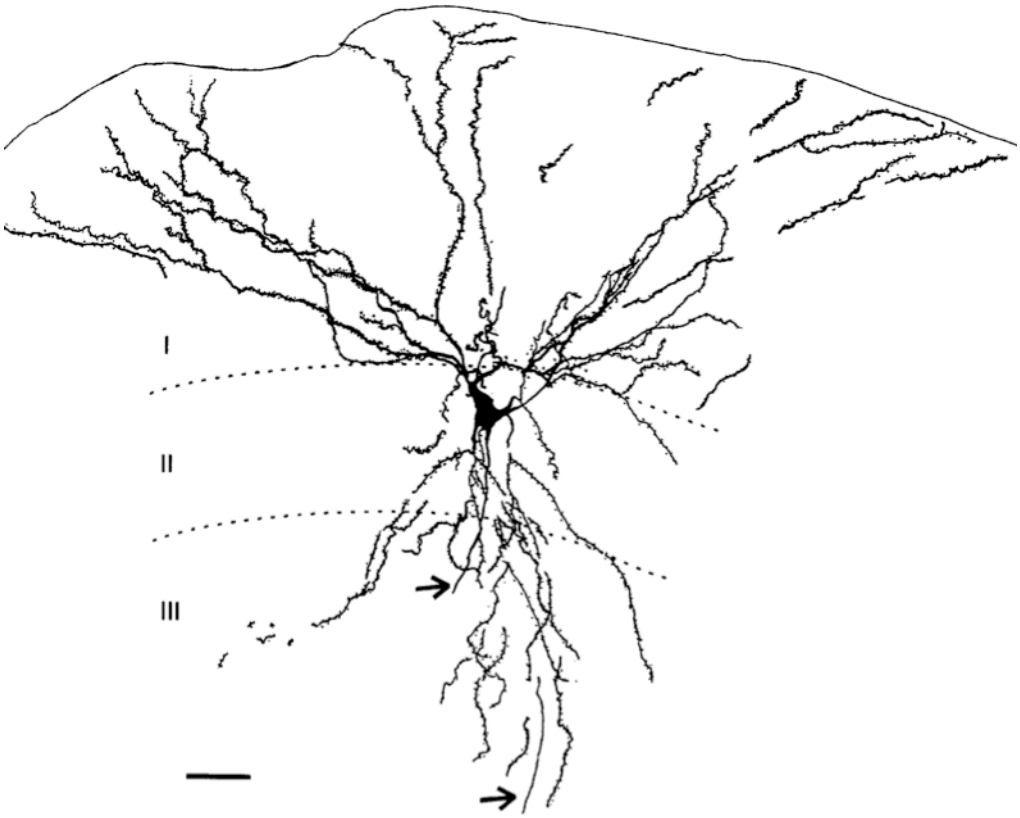

Figure 1.14 Morphology of MEC II stellate cells

Camera lucida reconstruction of an MEC II stellate cell. Scale bar = 40 μm. (Adapted from (Klink & Alonso, 1997))

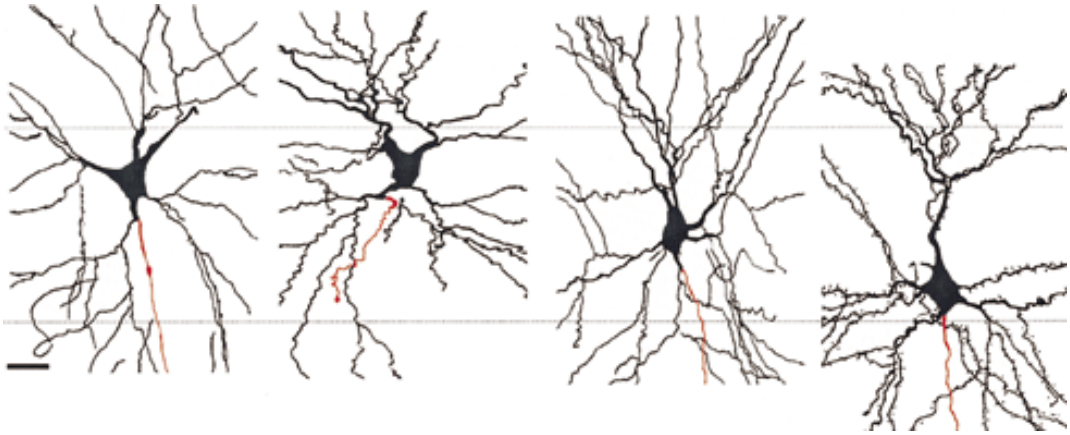

Figure 1.15 Variability of MEC II SC morphology

Camera lucida reconstruction of 4 SCs located at different positions within layer II. Scale bar = 40 μm. (Adapted from (Klink & Alonso, 1997)).

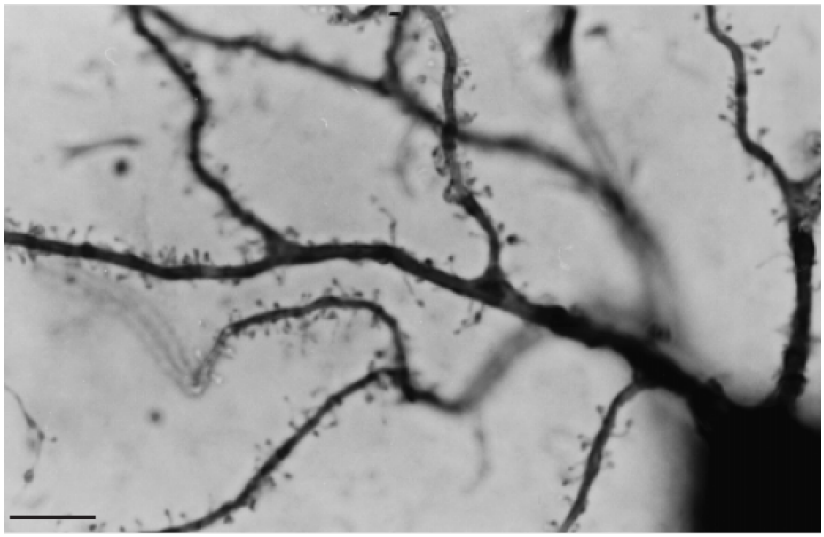

Figure 1.16 Dendritic spines of MEC II stellate cells

Photomicrograph of a cell, showing gradually tapering SC dendrites, with evenly distributed dendritic spines. Scale bar = 10 μm. (Adapted from (Klink & Alonso, 1997))

Stellate cells have a resting membrane potential of – 62.4 ± 3.1 mV and action potential threshold of – 50.9 ± 2.4 mV (Alonso & Klink, 1993). Under depolarizing or hyperpolarizing steady state current injection, membrane potential reaches an early peak (Vp) and later decays to a

lower level (Vs), resulting in a “sag” (Fig. 1.17 A and B); notably, even a small current injection caused a pronounced “sag” (Fig. 1.17B) (Alonso & Klink, 1993). The termination of current injection always resulted in an overshoot of resting membrane potential (Fig. 1.17 A and B) (Alonso & Klink, 1993), and repolarization overshoot after the end of highly hyperpolarizing current could occasionally evoke action potentials (Fig. 1.16 A). Depolarized to about – 55.6 ± 2.1 mV, stellate cells exhibited persistent subthreshold oscillations (Fig. 1.17D) at a frequency in the theta range (8.6 ± 2.1 Hz) (Fig. 1.17D) (Alonso & Klink, 1993), potentially mediated by an interplay between hyperpolarization-activated cyclic nucleotide-gated (HCN) channels and persistent sodium channels (Dickson et al., 2000).

Action potentials were initiated early during depolarizing current injection (Fig. 1.17A). Spikes were followed by triphasic membrane potential fluctuations, consisting of fast after hyperpolarizing potential (fAHP), depolarizing afterpotential (DAP) and medium after hyperpolarizing potential (mAHP) (Fig. 1.17C) (Dickson et al., 2000).

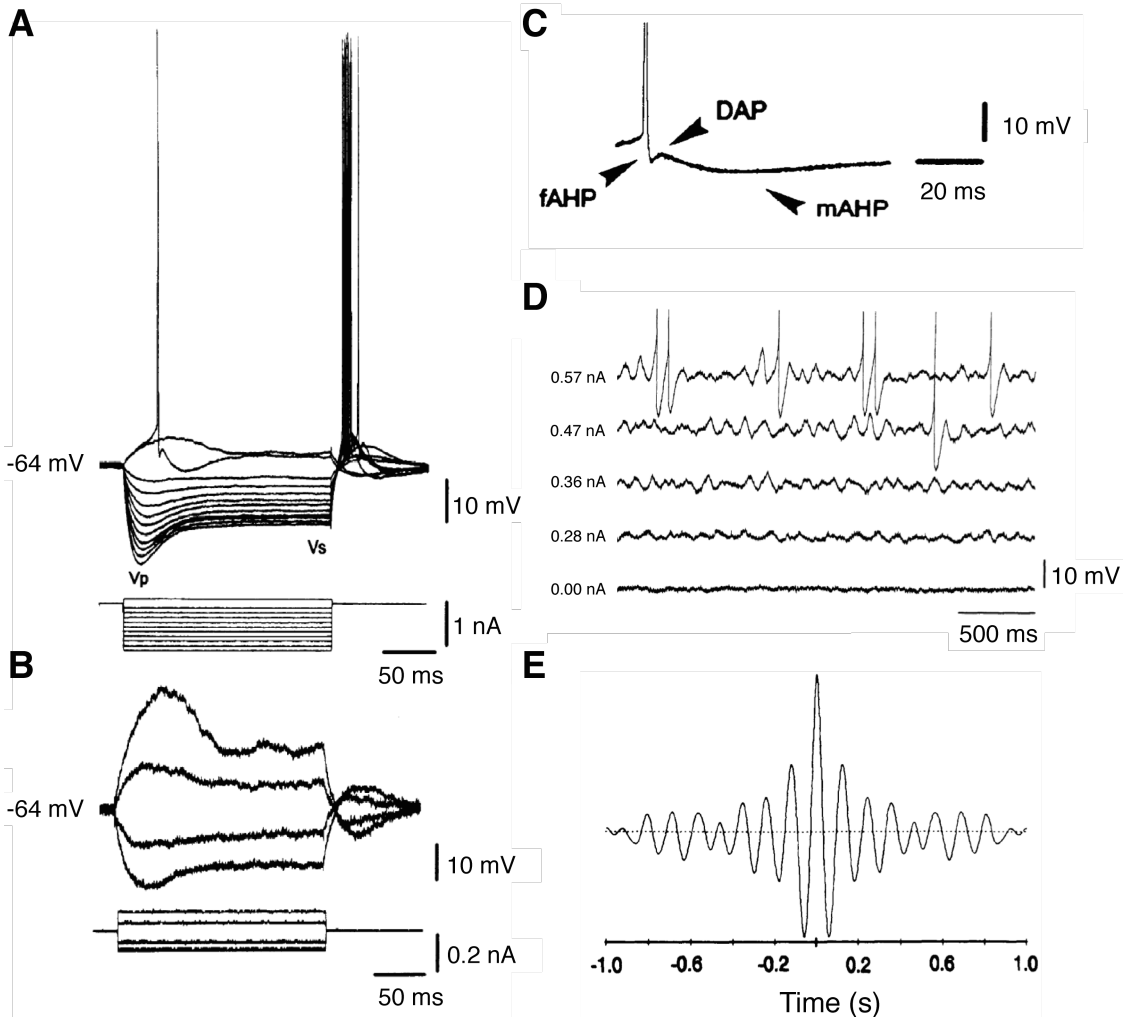

Figure 1.17 Electrophysiological profile of MEC II stellate cells

A and **B.** V-I relationship of stellate cells. **C.** Triphasic after action potential shape of SC. **D.** Persistent subthreshold membrane potential oscillations can be evoked in SCs by subthreshold depolarization. **E.** Autocorrelogram of oscillations in D are at theta frequency (8.6 Hz). (Adapted from (Alonso & Klink, 1993))

1.4.2 Pyramidal cells

MEC II pyramidal cells (PCs) have an average of 21 x 11 μm triangular soma and are usually located within the deepest third of layer II. PCs usually have one thick (4.3 ± 1.5 μm) apical dendrite (in rare cases 2), which is perpendicular or diagonal to the pia (Fig.1.19) and bifurcates just above layer II, and many short basal dendrites, which branch

extensively around the soma (Fig. 1.18) (Klink & Alonso, 1997). Upper and lower dendritic fields expand 184 ± 75 μm and 185 ± 35 μm in medio-lateral axis, creating a rectangular appearance (Klink & Alonso, 1997). PC dendrites are densely covered in short dendritic spines (Fig. 1.20) (Klink & Alonso, 1997).

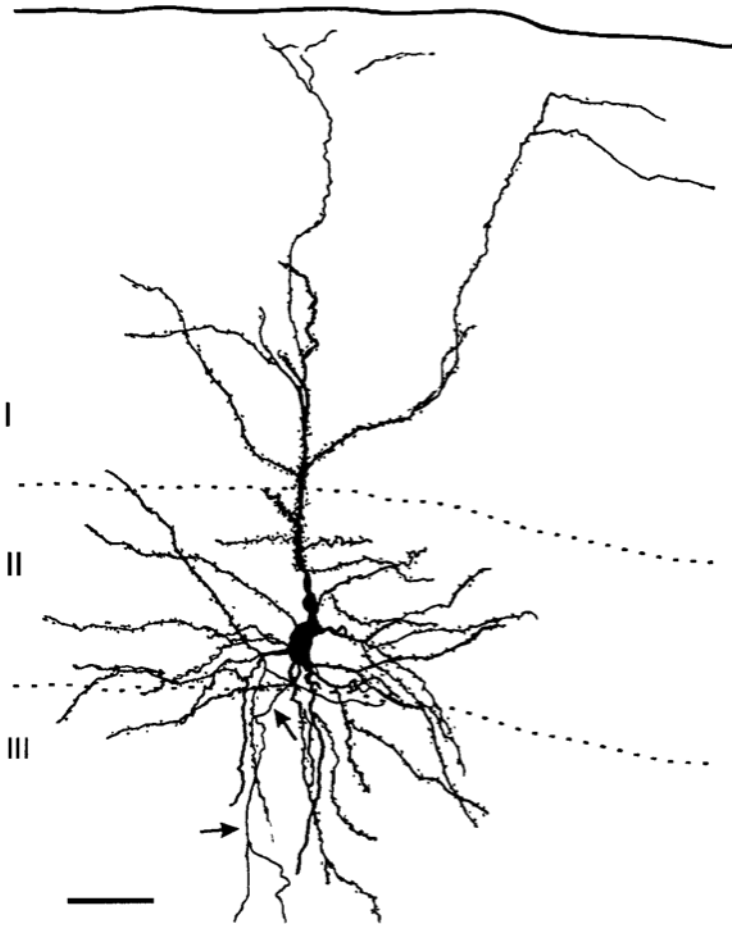

Figure 1.18 Morphology of MEC II pyramidal cells

Camera lucida reconstruction of the MEC II pyramidal cell. (Adapted from (Klink & Alonso, 1997))

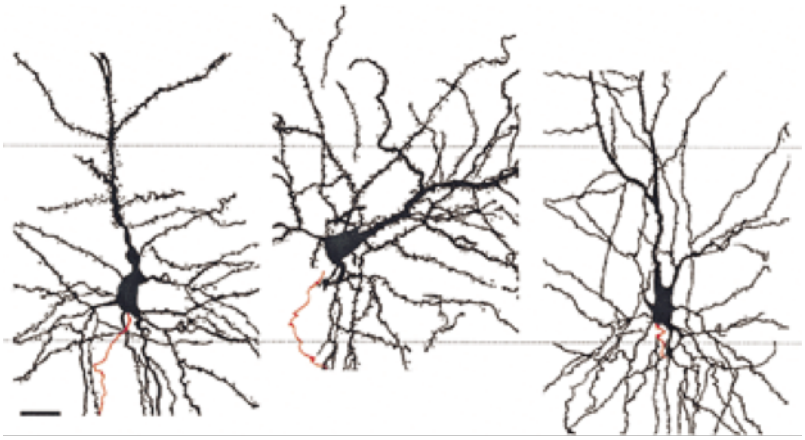

Figure 1.19 Variability of MEC pyramidal cell morphology
(Adapted from (Klink & Alonso, 1997))

Figure 1.20 Dendritic spines of MEC II pyramidal cells
Photomicrograph of the cell, showing PC dendrites, densely covered in short dendritic spines. Scale bar = 10 μm. (Adapted from (Klink & Alonso, 1997))

MEC II pyramidal cells have a resting membrane potential of – 63.7 ± 4.1 mV and action potential threshold of – 48.7 ± 2.5 mV. Injection of a large hyperpolarizing steady-state current can result in a "sag" (Fig. 1.21 A and B) (Alonso & Klink, 1993). In contrast to stellate cells, pyramidal cells do not exhibit persistent subthreshold theta membrane potential oscillations (Fig. 1.21D and E) (Alonso & Klink, 1993). Action potentials are evoked later than in SCs during depolarizing current injection (Fig. 1.21A). Sometimes, spikes are followed by a triphasic after action potential phase (Fig. 1.21C), but this is less pronounced than that seen in stellate cells (Alonso & Klink, 1993).

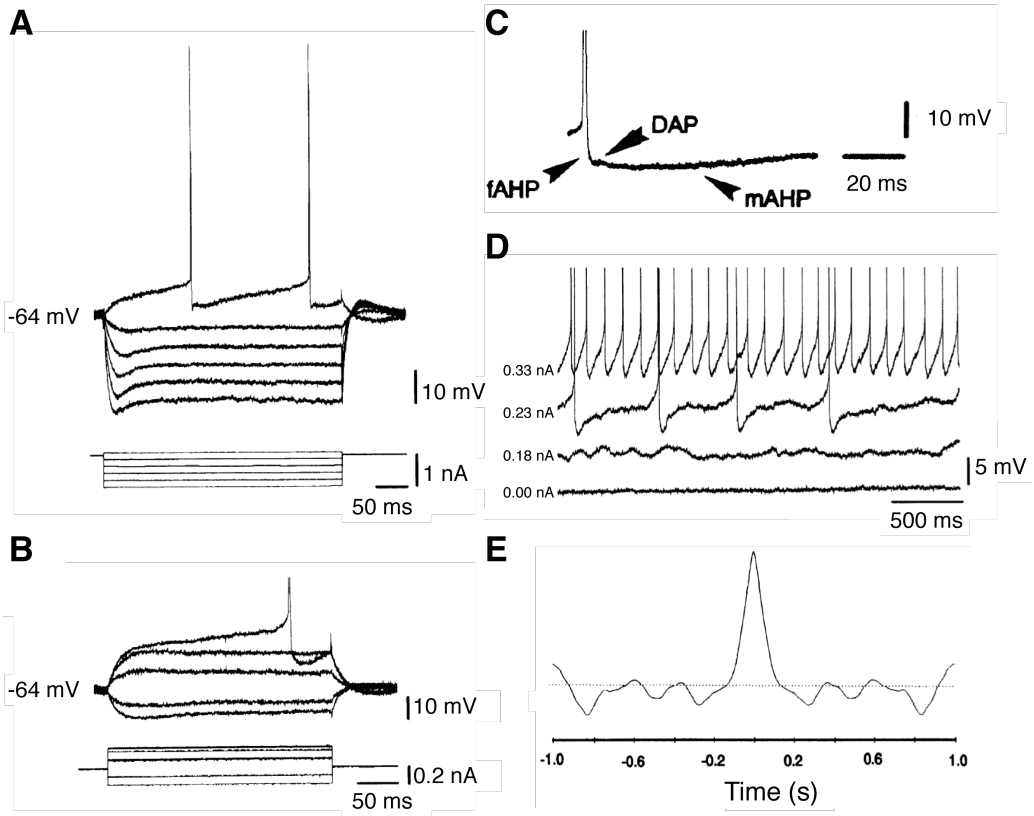

Figure 1.21 Electrophysiological profile of MEC II pyramidal cells

A and **B.** V-I relationship of pyramidal cells. **C.** Less pronounced triphasic after action potential shape than in SCs. **D** and **E.** Persistent subthreshold membrane potential oscillations cannot be evoked in pyramidal cells by depolarization. (Adapted from (Alonso & Klink, 1993))

1.4.3 Cellular phenotype of grid cells

Grid cell phenotype seems not to be confined to a single cell type, as neurons throughout all layers of MEC, presubiculum and parasubiculum display grid cell firing (Boccara et al., 2010; Sargolini, 2006). Since majority of grid cell data comes from tetrode recordings there is an outstanding debate if grid cells of MEC II are stellate cells or pyramidal cells or combination of both morphological types.

There is strong evidence for stellate cells representing a large fraction of the grid cell population for a few reasons. Firstly, they make up the majority of MEC II principal cell population (Gatome et al., 2010). Secondly, they have been found to show grid-like firing pattern (Burgalossi et al., 2011; Domnisoru et al., 2013; Schmidt-Hieber & Hausser, 2013; Zhang et al., 2013). Thirdly, stellate cell morphology and electrophysiology seems to be well suited to convey grid cell functions, since they have 4-6 independent dendrites which join each other at the soma (Klink & Alonso, 1997) potentially allowing independent computations in different dendrites, and exhibit subthreshold membrane potential oscillations at theta frequency (Alonso & Klink, 1993), what is used by oscillatory interference models for generating grid like firing activity (Burgess et al., 2007) and easily explain phase precession observed in grid cells *in vivo* (Hafting et al, 2008). Moreover, *in vitro* patch clamp recordings of more than 600 pairs of neuronal in MEC II revealed that stellate cells are interconnected with each other via inhibitory interneurons, with this connectivity sufficient to result in grid-like firing using attractor network model (Couey et al., 2013)

Recently there has been some evidence that MEC II pyramidal neurons may also contribute to the grid cell population (Ray et al., 2014; Tang et al., 2014). These cells form anatomical clusters and are calbindin antibody positive (CB+) in immunohistochemical stainings (Ray et al.,

2014; Kitamura et al., 2014). Two-photon calcium imaging of mice navigating in virtual environment has shown that grid cells are topologically clustered as opposed to nongrid cells (Heys et al., 2014). Another study used spike locking to theta oscillations in the extracellular recordings to identify stellate cells from pyramidal cells in freely moving animals and revealed that both cell types exhibit weak hexagonal activity in the environment, but that stronger hexagonal discharges were mainly found in pyramidal cells (19/99 pyramidal cells vs. 3/94 stellate cells) and stellate cells were mainly border cells (10/94 stellate cells vs. 3/99 pyramidal cells) (Tang et al., 2014).

To sum up, it seems that grid cells are not restricted to one morphological type of cells in MEC II and both pyramidal cells and stellate cells exhibit grid-like firing activity.

1.5 DENDRITIC INTEGRATION

Receiving inputs from other cells and converting them to output in the form of frequency and timing of action potentials (APs) is the main computational function of a neuron. This so called input-output function of the cell depends largely on the cell morphology and membrane properties. Findings in the last decade in cellular neuroscience indicate that dendrites can act as highly nonlinear devices, expanding computational properties of neurons to a great extent.

Different cell types within the central nervous system have a large variety of dendritic arbours as well as a differing arrangements (and even properties in some cases) of neurotransmitter receptors and voltage-gated ion channels, suggesting potential differences in input-output transformation properties adapted to the variety of functions they perform. In this chapter I will discuss the cellular factors

influencing dendritic integration in various cell types within central nervous system.

1.5.1 Factors influencing dendritic integration

Most neurons receive multiple excitatory and inhibitory inputs on the dendritic arbour and perisomatic region. Excitatory and inhibitory inputs induce excitatory postsynaptic potentials (EPSPs) and inhibitory postsynaptic potentials (IPSPs), respectively. According to the simple model of synaptic integration, action potentials are generated when excitation substantially exceeds inhibition at a given time, bringing the cell to the AP threshold. To achieve this, both EPSPs and IPSPs must propagate from the site where they are generated to the action potential initiation zone, therefore, the factors influencing this "journey" significantly influence the input-output function of the cell. The most significant of those known so far are the passive properties of the membrane, composition and properties of active conductances, the presence or absence of dendritic spikes (D-spikes), properties of back propagating action potentials (bAPs) and the spatial arrangement of inputs to the cell and the temporal pattern of their activation.

Each cell type has a unique resting membrane potential (V_{rest}) and action potential threshold (V_{thr}). For example, MEC II stellate cell V_{rest} *in vitro* is ~ – 63 mV and V_{thr} is ~ – 51 mV (Alonso & Klink, 1993), creating a gap between resting and firing of ~ –11.5 mV. The significance of each synaptic potential in bringing the cell closer to the AP generation threshold depends on the size of the local PSP and how much it attenuates when propagating to the AP generation site (there is some debate about where exactly it is, but the majority of evidence suggests it being in the axon initiation segment) (Clark et al., 2005; Colbert & Johnston, 1996; Stuart & Sakmann, 1994).

1.5.2 Input location

The local EPSP amplitude at the synapse site depends on the input impedance of a compartment. As the input impedance is higher in distal dendrites, local EPSPs evoked by the same synaptic conductance are larger in amplitude in distal compared to proximal dendrites or the soma (Fig.1.22). Because of cable filtering, distal EPSPs are more strongly attenuated while propagating to the soma. For given local EPSP amplitude at the synaptic site, distal EPSPs are smaller in amplitude than proximal ones in somatic recordings (Fig.1.22). Moreover, due to cable filtering somatically recorded EPSPs evoked in distal dendrites have a larger half-width than proximally evoked EPSPs, resulting in more efficient temporal summation (Fig.1.22). Therefore, different dendrites have been suggested to perform distinct computations with proximal dendrites acting as coincidence detectors and distal dendrites as temporal integrators (Magee, 2000).

Moreover, in some, but not all, synapses of CA1 pyramidal neurons distal EPSPs are also scaled by higher synaptic conductance to compensate for attenuation of EPSPs resulting in comparable somatic EPSPs originated in distal and proximal dendrites (Magee & Cook, 2000). This synaptic scaling in Schaffer collaterals of CA1 was mediated by higher density of AMPA, but not NMDA receptors in distal parts of the dendrite (Nicholson et al., 2006), suggesting synaptic inputs with different properties in different parts of the dendritic tree.

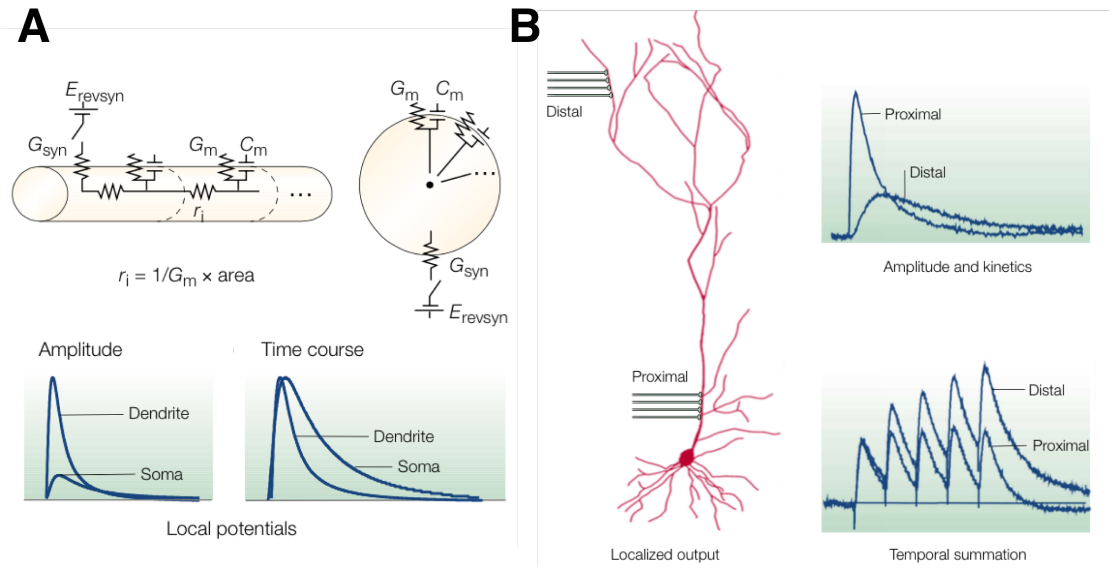

Fig. 1.22 Dendritic filtering of EPSPs

A. Top: electric circuit analogy of the dendritic cable (left) and somatic sphere (right). Bottom: predictions of the amplitude (left) and time course (right) of EPSPs at the site of origin. **B.** Left: schematic view of the CA1 pyramidal neuron with location of proximal and distal excitation indicated. Right: somatic recordings of EPSPs originating in proximal and distal dendrites (top) and temporal summation differences between them (bottom). (Adapted from (Magee, 2000))

1.5.3 Active conductances

Dendrites of some cells were found to express various voltage-gated channels. Composition, properties and distribution of these channels is cell type specific. For instance Na^+ channels are distributed uniformly across the dendritic tree for most cell types (Spruston, 2008), but A-type K^+ channels (Hoffma et al., 1997) show somatodendritic gradient in CA1 but not layer 5 pyramidal neurons (Bekkers, 2000). Hyperpolarization-activated cation (HCN) channels are expressed with a somatodendritic gradient in CA1 and layer V pyramidal neurons (Lörincz et al., 2002), but are uniformly distributed in cerebellar Purkinje cells (Angelo et al., 2007) and are absent in dendrites of CA3 and layer II/III neurons

(Lörincz et al., 2002). Evidence for HCN mediated hyperpolarization-activated (I_h) current has also been detected in MEC II stellate cells and to much smaller extent in some of MEC II pyramidal neurons using somatic whole-cell recordings (Alonso & Klink, 1993), however, the distribution of it across the dendritic tree is not yet known.

How different active conductances influence dendritic integration of synaptic inputs? I_h has been proposed to mediate location independent temporal summation of EPSPs in CA1 pyramidal (Magee, 1999) and cerebellar Purkinje cells (Angelo et al., 2007; Williams & Stuart, 2000). Dendritic Na^+ and Ca^{2+} channels can amplify EPSPs at the site of generation (Lipowsky et al. , 1996; Schwindt & Crill, 1996). Moreover, dendritic Na^+, K^+ and Ca^{2+} channels support backpropagating action potentials (bAPs) (Stuart, et al, 1997). Strong activation of Na^+ and Ca^{2+} channels can also generate dendritic spikes (Amitaiet al., 1993; Waters et al., 2003).

Moreover, it seem that subthreshold membrane potential can alter AMPA and NMDA contribution to synaptic currents, changing the temporal dynamics of EPSP and calcium concentration at the spine (Seong et al., 2014). $GABA_B$ receptors were also found to have an influence on NMDA receptor mediated calcium signals in dendritic spines (Chalifoux et al., 2010).

1.5.4 Dendritic spikes

Both theoretical and experimental studies showed the possibility of regenerative events in dendrites boosting local summation. These dendritic events have all-or-none activation dynamics, the summation after the threshold being noticeably bigger or substantially different, followed by inactivation phase, thus, called dendritic spikes (D-spikes). However, activation threshold, amplitude and time course of D-spikes

can vary in different cells, different dendrites of the same cell or even at the different activation times of the same dendrite (Major et al., 2013). Dendritic spikes can be mediated by various ion conductances, however, 3 main types of dendritic spikes can be identified based on major conductance mediating the spike generation.

Dendritic spikes are predominantly mediated by sodium channels (Na^+ spikes), calcium channels (Ca^{2+} spikes) (Schwartzkroin & Slawsky, 1977, Schiller et al., 1997) or NMDA receptors (NMDA spike) (Schiller et al., 2000a), although multiple types of channels are usually activated during each of those events. These types dendritic spikes are distinct in their onset conditions and temporal decay dynamics, making them identifiable from dendritic recordings (Fig.1.23). However, dendritic spikes do not propagate well to the soma, making them harder to detect in somatic recordings (Fig.1.23).

First type of dendritic spikes detected was Ca^{2+} spike. It was initially found in sharp microelectrode recordings during strong synaptic excitation of Purkinje cells in cerebellum and pyramidal cells in hippocampus (Schwartzkroin and Slawsky, 1977), and later confirmed via dual dendritic and somatic patch-clamp recordings and calcium imaging (Waters et al., 2003). Ca^{2+} spikes have a long duration and relatively slow onset, consistent with slow kinetics of Ca_v channels. Ca^{2+} spike also occur when weaker synaptic inputs are paired with back propagating action potential, thus, called "backpropagaring action potential evoked Ca^{2+} spike" (BAC spikes) (Larkum et al., 1999) which might mediate coincidence detection mechanism in cells. Since Ca^{2+} spikes last to up to 50 ms and have 50ms refractory period after, they can be evoked at 10 Hz max frequency (Golding et al., 1999).

Dendritic Na^+ spikes have much faster kinetics than Ca^{2+} spikes due to fast activation and quick inactivation of Na_v channels (1ms open and

1ms inactivated), thus, they can be activated at high frequencies, as often as 500 Hz (Smith et al., 2013). They do not propagate reliably out of the branch they originated, thus, are difficult to detect in somatic patch-clamp recordings (Losonczy & Magee, 2006). Na^+ spikes can be abolished with the Na_v channel blocker tetrodotoxin (TTX) (Fig.1.23) (Nevian et al., 2007). Dendritic Na^+ spikes can be evoked by nearly simultaneous activation of clustered inputs on as little as 10 synapses in pyramidal neurons of hippocampus (Losonczy & Magee, 2006) and neocortex (Branco et al., 2010).

NMDA spikes were found in basal and oblique dendrites but not apical tuft dendrites of cortical pyramidal cells (Schiller et al., 2000a). NMDA spikes result from glutamate binding to NMDA receptors, which are voltage sensitive, since they need initial depolarization of cell membrane to remove Mg^{2+} block from the channel pore, making them coincidence detectors. NMDA receptors have regenerative properties since activation of them increases depolarisation of the cell membrane relieving more NMDA receptors from Mg^{2+} block, what subsequently causes more depolarisation and eventually resulting in NMDA spike if large enough numbers of NMDA receptors are activated. NMDA spikes can be abolished with the NMDA receptor antagonist (2R)-amino-5-phosphonovaleric acid (APV) (Fig.1.24). Differently than Ca^{2+} and Na^+ spikes NMDA spikes cannot propagate into the regions of dendrites where NMDA receptors are not activated by glutamate.

Na^+ and NMDA spikes but not Ca^{2+} spikes can be evoked in basal dendrites of layer 5 pyramidal neurons (Nevian et al., 2007), suggesting differential excitability of different dendrites.

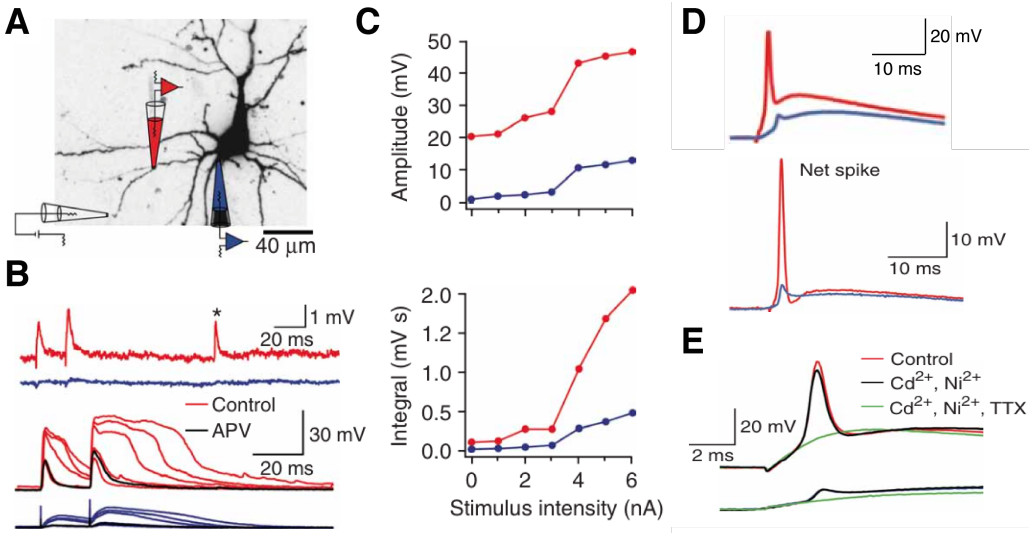

Fig. 1.23 NMDA and Na^+ spikes in basal dendrites of layer 5 pyramidal cells

A. Experimental set up with somatic and dendritic recording electrodes in blue and red, respectively, and synaptic stimulation electrode in white. **B.** Upper traces: EPSPs evoked by 2 pulses of 50 Hz stimulation and spontaneous EPSP (asterisk), measured in dendrite (red) and soma (blue). Bottom traces: Dendritic NMDA spikes in dendrite (red) and soma (blue), which was blocked with APV (black). **C.** NMDA spike caused a boost in amplitude and integral. Increasing stimulus intensity resulted in an amplitude, but not integral plateau. **D.** EPSP with dendritic Na^+ spike (top) and net Na^+ spike (subthreshold voltage subtraction) in dendritic (red) and somatic (blue) recordings. **E.** Na^+ spike was blocked with TTX. (A, B, C and D adapted from Fig. 7 and E, F from Fig. 5 from (Nevian et al., 2007))

Dendritic spikes were proposed to increase the local computational properties of the cell. Majority of studies of dendritic spikes were done *in vitro* and evoking them required highly clustered synchronous inputs to the dendritic tree, raising the doubts if that synaptic activation pattern was common *in vivo*. However, more and more experiments are demonstrating dendritic spikes *in vivo* in different cell types and under different behavioural tasks (Larkum & Zhu, 2002; Waters et al., 2003, Smith, et al., 2013), suggesting their functional importance. By now

dendritic spikes have been shown to be relevant in various functions such as touch perception (Xu et al., 2012), processing of sensory inputs (Palmer et al., 2014), angular tuning in barrel cortex (Lavzin et al., 2012), and orientation tuning in visual cortex (Smith et al., 2013) motor behaviour (Ghosh et al. 2011) and spatial navigation (Sheffield and Dombeck, 2014).

1.5.5 Dendritic integration in different cells

Based on differences in morphology and properties and distribution of active conductances different cell types or the same cell type of different brain areas might integrate inputs in different manner. Here I will briefly compare the rules governing dendritic integration in different cells.

Majority of these studies have assessed dendritic integration using two-photo glutamate uncaging, which allowed synaptic activation of single spine resolution, together with whole-cell patch clamp recordings, to assess the individual and multiple synapse activation to the soma. This also allowed constructing so called linear sum EPSPs from the responses of individual synapses, what later could be compared to measured EPSPs while activating these synapses together. Based on that integration was called linear, sublinear or supralinear.

Supralinear integration and dendritic spikes have been reported in majority of pyramidal cells of neocortex layer II/III and layer V (Branco et al., 2010; Branco & Häusser, 2011), and hippocampus CA1 (Losonczy & Magee, 2006) and CA3 (Makara & Magee, 2013) areas while activating highly spatially clustered synapses over the short period of time. Spreading the synapses across the dendrite or activating them over a longer period of time decreased supralinearity or even made inputs to be integrated in a linear manner (Branco et al., 2010; Branco

& Häusser, 2011). Supralinear summation of synaptic inputs of pyramidal cells of neocortex and hippocampus is mediated by voltage-gated sodium channels and NMDA receptors, thus, can be reduced with spatiotemporal spreading of activated synapses, and blocked via bath application of TTX and APV for VGSCs and NMDA receptors, respectively (Branco et al., 2010; Branco & Häusser, 2011, Losonczy & Magee, 2006).

Granule cells of the dentate gyrus were found to integrate inputs in a linear manner with the absence of dendritic spikes and strong attenuation of EPSPs (Krueppel et al. , 2011).

Pyramidal cells of the neocortex layer II/III and V can integrate both distal and proximal inputs in a supralinear manner, however, distal inputs are integrated more efficiently and via longer time interval (Branco & Häusser, 2011). Location on the dendrite dependent integration has been also found in the principal neurons of layer V of medial entorhinal cortex, where unitary event of synapses activation is larger distally and dendritic spikes can be evoked only at the distal, but not proximal dendrites (Gasparini, 2011; Medinilla et al., 2012)

1.5.6 Dendritic integration and spatial navigation

It is not clear yet if firing fields of grid cells emerge from network activity or intrinsic properties of the cell. There is some evidence thought that intrinsic properties of hippocampal place cells are important for formation of spatially modulated firing fields. Firstly dendritic spikes have been found in place cells of hippocampus during two-photon calcium imaging of dendritic branches while head restrained mice were navigating in virtual environment (Sheffield and Dombeck, 2014). Prevalence of dendritic spikes throughout dendritic arbour was not only highly variable depending on animal's location in virtual

environment but also was a good indicator of spatial precision and persistence or disappearance of place fields (Sheffield and Dombeck, 2014). Another study has shown that a small and spatially uniform depolarization of spatially untuned somatic membrane potential of silent cells lead to a sudden and reversible emergence of a spatially tuned subthreshold response and firing fields, suggesting the importance of postsynaptic cell excitability in formation of place fields (Lee et al., 2012).

Dendritic spikes might be well suited to explain grid cell activity. Firstly, fast onset Na^+ spikes, might increase the precision of grid cell phase precession, increasing the robustness of the temporal code of grid cells. Secondly, long lasting NMDA spikes might function as coincidence detectors since both depolarization of cell membrane and abundant release of glutamate in multiple co-localized synapses are needed to evoke NMDA spikes, what might mediate the precision and robustness of grid cell firing. These hypothesis need to be tested in well controlled environment, which can be achieved by *in vitro* whole-cell patch clamp recordings together with synaptic activation at single spine resolution provided by two-photon uncaging of MNI-glutamate, what was chosen to be methods of this thesis. Moreover, *in vitro* experiments allow determining active conductances mediating dendritic integration of synaptic inputs of these cells via bath application of selective channel antagonists such as TTX for voltage-gated sodium channels and APV for NMDA.

1.6 Aims of this thesis

This thesis aims to describe dendritic integration in the principal neurons of the MEC II by addressing the following questions:

1. What is the input-output conversion of MEC II stellate cells?
Are dendrites of stellate cells passive or active? Is integration linear, sublinear or supralinear? Do distal dendrites integrate inputs in a similar manner to proximal dendrites? How does input timing effect integration? These questions will be address in the Chapter 3 of the thesis.

2. Which cellular mechanisms mediate dendritic integration in MEC II stellate cells? Do stellate cells exhibit dendritic spikes? This will be addressed in the Chapter 4 of the thesis.

3. How do stellate cells integrate inputs under *in vivo*-like conditions? How are inputs to multiple dendrites summated? How many dendrites need to be activated to evoke action potentials? This will be address in the Chapter 5 of the thesis.

4. Do MEC II pyramidal cells integrate inputs similarly or differently from stellate cells? This will be addressed in the Chapter 6 of the thesis.

2. MATERIALS AND METHODS

2.1 Electrophysiology

2.1.1 Slicing and experimental solutions

All experiments were performed using acute horizontal brain slices from 26-30 day-old C57/BL6 mice. Slicing was performed in an ice-cold sucrose solution, containing (in mM): NaCl (87), sucrose (75), glucose (25), $NaHCO_3$ (25), $MgCl_2$ (7), KCl (2.5), NaH_2PO_4 (1.25), $CaCl_2$ (0.5). For a period of 30 min immediately after slicing, slices were stored in preheated (32°C) artificial cerebrospinal fluid (ACSF), with low Ca^{2+} and high Mg^{2+} concentrations, containing (in mM): NaCl (125), glucose (25), $NaHCO_3$ (26), $MgCl_2$ (5), KCl (2.5), NaH_2PO_4 (1.25), $CaCl_2$ (0.5), preheated to 32°C. Slices were subsequently stored at room temperature.

Experiments were performed in ACSF, containing (in mM): NaCl (125), glucose (25), $NaHCO_3$ (26), $MgCl_2$ (1), KCl (2.5), NaH_2PO_4 (1.25), $CaCl_2$ (2) at a temperature of 32-34°C. In addition, 50 µM of D-APV and 0.5 µM of TTX were added to the regular ACSF solution to block NMDA receptors and voltage gated sodium channels, respectively. All extracellular solutions were equilibrated with carbogen (95% O_2, 5% CO_2) and had a pH of 7.3.

2.1.2 Slicing procedure

All procedures were performed in agreement with the regulations of the Home Office.

Animals were briefly anesthetized with isoflurane prior to decapitation. After decapitation with sharpened scissors, fur was removed from the skull, and 1 sagittal and 2 lateral cuts at the caudal and rostral parts of the skull were made with fine surgical scissors. Following this, the skull was opened with curved surgical forceps to free the brain. Careful cuts to the posterior side of cerebellum and rostral part of the brain were made with a scalpel and the brain was transferred into an ice-cold slice storage solution with a surgical spatula.

The brain was then cut sagittally to separate the hemispheres. Each hemisphere was then trimmed dorsally to make a flat surface to attach it to a metal plate using super glue for slicing. The plate was then placed into a slicing chamber and ice-cold ACSF was poured over it. This chamber was then fixed onto a vibrating slicer (Leica VT1200S), calibrated to minimize vibrations in z-axis. Wilkinson Sword blades were used to slice the brain after carefully removing the manufacturing lubricant. Slices (5-6), each 350 μm thick, were produced from each hemisphere starting when dentate gyrus became visible. Slicing was performed at a speed of 0.7mm/s and vibration amplitude of 1.5mm. Slices were immediately placed into pre-heated (32-34°C) ACSF for a 30 min incubation period. During experiment slices were placed in the experimental chamber with a constant exchanging perfusion of carbonated ACSF at 32-34°C.

2.1.3 Whole-cell patch clamp recordings

In the recording chamber MEC was identified by visually visible landmarks indicated in Mouse Brain Atlas for the horizontal slices (http://www.mbl.org/atlas232/atlas232_frame.html). Somatic whole-cell recordings were obtained from stellate and pyramidal cells in layer 2 of the medial entorhinal cortex. Axograph software was used to apply hyperpolarizing and depolarizing current to obtain an IV curve, which

was used to confirm the cell type. Further electrophysiological recordings were acquired with custom-made software written in Matlab at 50 kHz sampling frequency using a Multiclamp 700B amplifier (Molecular Devices). Patch pipettes of 5MΩ resistance were filled with internal solution containing (in mM): $KMeSO_4$ (140), HEPES (10), KCl (7.4), $MgCl_2$ (0.3), EGTA (0.1), NaGTP (0.3), Na_2ATP (3), sodium phosphocreatine (1) – and used for somatic whole cell recordings. 50 μM Alexa 594 dye was added to this solution to visualize cell morphology. The series resistance of recordings was typically less than 30MΩ.

2.1.4 Cell type identification

MEC II consists of 2 types of principal neurons: stellate cells and pyramidal cells. They differ in both cell morphology and electrophysiology. Stellate cells of MEC II were identified using their morphological and electrophysiological signatures described below. Initial identification of stellate cells was done under the inverted light microscope with 50x magnification. Stellate cells have trapezoid or oval-shaped soma (as opposed to the triangular soma of pyramidal cells), oriented perpendicular to the pia, and they are more abundant in the superficial third of MEC II (closer to the pial surface) (Klink & Alonso, 1997). After a cell was whole-cell patched and filled with Alexa 568 fluorescent dye (present in the internal solution of the patch pipette), the morphology of the dendritic arbour is visible under a fluorescent microscope. Stellate cells have a star-like shaped dendritic tree consisting of 4-6 primary dendrites spreading in different directions (Fig 3.1A). Moreover, after dendrites are filled with fluorescent dye, the dendritic spines, which are abundant and evenly distributed throughout the entire dendritic tree, can be seen. Due to the cell morphology, dendrites rarely occur parallel to the slice surface, which provided us with only short stretches of dendrite available in a single Z plane.

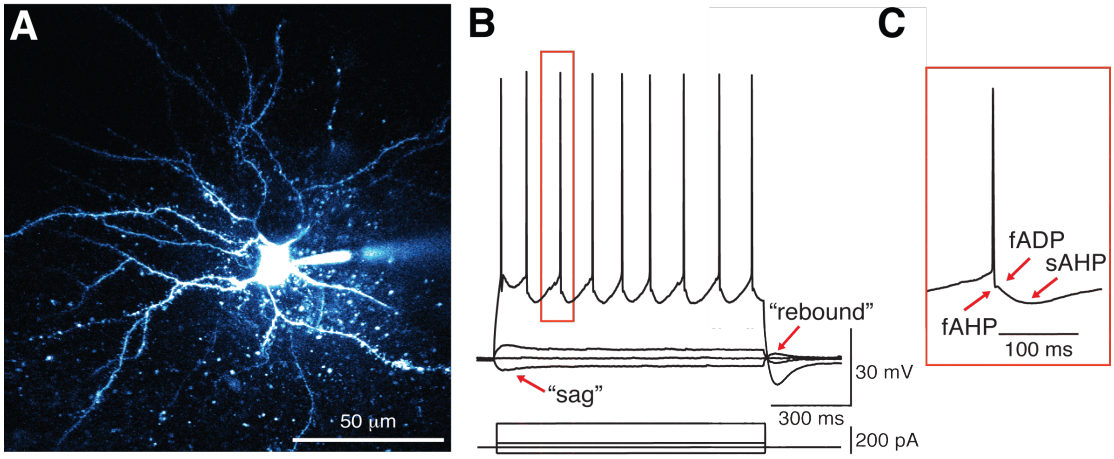

Figure 2.1 Morphology and electrophysiology of an MECII stellate cell

A. A stellate cell in MEC II was whole-cell patched and filled with Alexa 568. The dendritic arbour displays a star-like morphology. **B.** SC response to hyperpolarizing and depolarizing somatic current step injection. **C.** Triphasic shape of membrane potential dynamics following the action potential.

In addition to morphology, stellate cells differ from MEC II pyramidal cells in terms of their electrophysiological properties, as was assessed by injecting steady state hyperpolarizing and depolarizing current steps. Both depolarizing and hyperpolarizing subthreshold current injections caused the membrane potential to reach an early peak and then decay to a lower level, resulting in so called "sag" (Alonso & Klink, 1993) Fig 3.1B). At the end of the current pulse the membrane response transiently overshot the resting membrane potential ("rebound") (Alonso & Klink, 1993) Fig 3.1B). These membrane potential dynamics are thought to be caused by the hyperpolarization activated current (I_H) (Krüppel, 1993). Moreover, stellate cells show triphasic membrane potential dynamics response following an action potential, consisting of fast afterhyperpolarizing potential (fAHP) leading by slow afterdepolarizing potential (sADP) and then slow afterhyperpolarizing potential (sAHP) (Alonso & Klink, 1993) Fig 3.1C. The "sag", "rebound" and triphasic stages following action potential are characteristic of

stellate cells of MEC II and are not typical of pyramidal cells of MEC II (Alonso & Klink, 1993). These membrane potential dynamics are mediated by I_H and can be blocked by drugs targeting hyperpolarization-activated cyclic nucleotide-gated (HCN) channels (Gasparini & DiFrancesco, 1997; Harris & Constanti, 1995; Krüppel, 1993), abundant in the membranes of MEC II stellate cells but not in pyramidal cells (Alonso & Klink, 1993; Nolan et al., 2007).

Pyramidal cells of MEC II exhibit a triangular-shaped soma with a clear apical dendrite projecting towards the pia (Fig. 2.2A). Moreover, they do not show "sag" and "rebound" responses to the hyperpolarizing and depolarizing steady state current injection (Fig.2.2B).

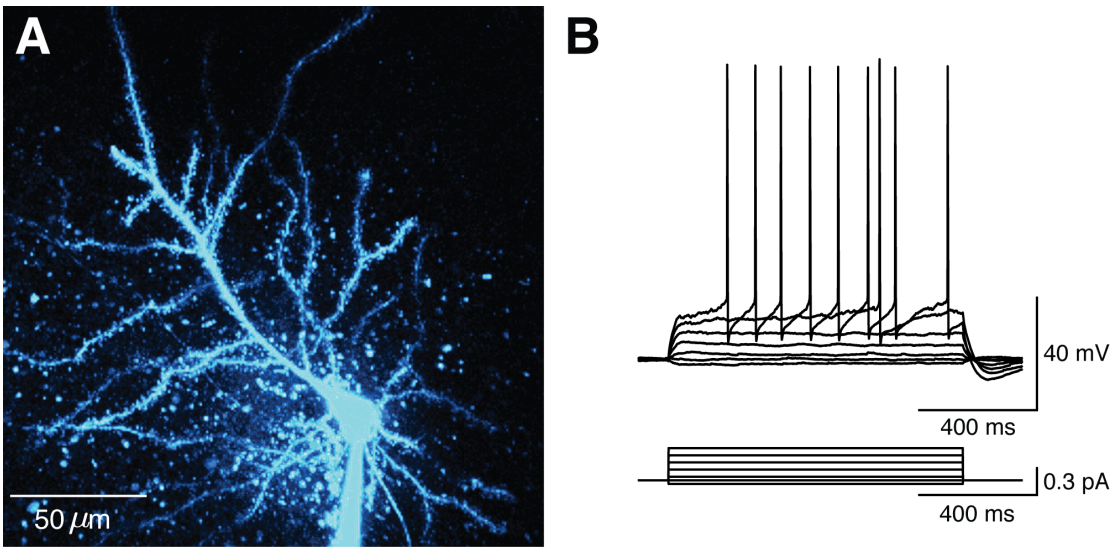

Figure 2.2 Morphology and electrophysiology of pyramidal cells of MEC II

A. Pyramidal cell whole-cell patched and filled with Alexa 594.

B. Pyramidal cell response to the hyperpolarizing and depolarizing somatic current step injection (same cell as in A).

In some case intermediate cell types were detected with a combination of either pyramidal cell morphological and stellate cell

electrophysiological features or the other way around. They were not as common (> 10%) and experiments were not carried out on them.

2.2 Two-photon imaging and uncaging

To test dendritic integration fast local activation of synapses is needed. Two-photon photoleases of MNI-glutamate enables these very properties mimicking presynaptic release of isolated inputs, with high concentrations of locally restrained glutamate, which can freely bind glutamate receptors on individual spines (Matsuzaki et al. 2001; Carter & Sabotini, 2004; Losonczy & Magee, 2006). MNI-glutamate shows no interference with glutamate receptors however it is known to interfere with synaptic activation of $GABA_A$ receptors, what was not a problem in experiments since we did not look at the effects of inhibitions for dendritic integration.

2.2.1 MNI-glutamate uncaging

Simultaneous two-photon imaging and dendritic stimulation at single-synapse resolution by uncaging MNI-caged-L-glutamate was performed with two Ti-sapphire lasers (MaiTai, Spectra-Physics) tuned to 810nm and 720-730nm for imaging and uncaging, respectively (Branco et al., 2010; Branco et al., 2011). After the soma of the cell was patched and filled with internal solution containing a fluorescent dye (Alexa 594), dendrites and dendritic spines became visible using two-photon microscopy. Healthy dendrites relatively close to the surface of the slice were selected for uncaging with MNI-caged-L-glutamate solution - 24 mM of MNI-caged-L-glutamate (Tocris Cookson, UK) dissolved in a solution containing (in mM): NaCl (125), glucose (25), KCl (2.5), HEPES (10), $CaCl_2$ (2), $MgCl_2$ (1), applied locally via a glass pipette.

2.2.2 Uncaging on single dendritic branch

Multiple spines were selected in a pseudo random manner, distributed by the experimenter's choice along the dendrite (Fig.2.4A). First, individual EPSPs of each spine were assessed by stimulating them independently (at 300 ms intervals) (Fig. 2.4B). Then an increasing number of synapses were stimulated at 10 s intervals between each trial (Fig.2.4D). To assess the sum of the hypothetical linear summation, traces were constructed from the individual EPSP traces with the same time shift as the interval in the stimulation of the multiple synapses experimentally (Fig.2.4C).

To assess dendritic integration in the stellate cells, two-photon MNI-glutamate uncaging on single dendritic branches was used. In brief, I selected an intact dendrite that was superficial enough as to be well accessible by MNI-glutamate, which was applied to the surface of the slice by a large tip pipette. Then I selected 10-17 dendritic spines (Fig 2.2A) on that branch and uncaged MNI-glutamate on each of them separately, recording single synapse evoked EPSPs (sEPSPs) (Fig 2.2B) in the soma. Then I uncaged combinations of these spines in increasing numbers (1, 2, 3, 4 etc. until all were included) while recording EPSPs in the soma (Fig. 2.2D). Spines were selected in a pseudo random manner by an experimenter in order to exclude a potential sequence effect (Branco et al., 2010).

Experiment on the cell was terminated if there was a photodamage to the dendrite, detectable by the "swelling" to the dendrite and depolarisation of the cell membrane. Recordings of photodamaged dendrites excluded out of analyses. Recordings were also excluded in cases of physical drift of the slice due to slice swelling or inconsistency of

perfusion. This usually was detectable either by imaging or sudden big changes (usually decrease) in EPSP size.

Uncaging laser exposure time was 0.5 ms with laser power adjusted to evoke EPSPs at physiologically relevant amplitudes (Fig. 3.1). Uncaging timing and location was controlled by custom-made software written in Matlab. The uncaging interval was 0.6-1ms for the majority of recordings. To assess the temporal integration window, the interval was increased to 4ms or 8ms. Uncaging was performed on distal, medial and proximal parts of the dendrites defined by the distance of the soma by 0-70 μm, 70-140 μm and < 140 μm, accordingly. The distance from the soma of the stimulated part of dendrite was measured using the Simple Neurite Tracer of ImageJ of image stack acquired after experiment.

2.2.3 Uncaging on two dendritic branches

To assess dendritic integration across two dendrites, uncaging spots were distributed in an interleaved manner on two nearby dendrites. In a number of recordings (n = 11) the input-output function of both individual dendrites and the dendrites activated together was assessed. Recordings exhibiting the input-output function of one dendrite, the other dendrite or the sum of the two dendrites were interleaved in time to ensure comparable conditions.

2.3 *In vivo*-like membrane potential dynamics

In the experiments described above, recordings were performed by stimulating one or two dendrites. However, multiple dendrites are probably being activated under realistic conditions when the animal is behaving in the environment. To assess how the inputs on one dendrite are integrated under more physiological conditions, I injected membrane

potential dynamics taken from *in vivo* whole-cell patch clamp recordings in head restrained animals crossing the active field of a grid cell in a virtual reality environment (Schmidt-Hieber & Hausser, 2013).

To determine the current that needs to be injected to reproduce these membrane potential dynamics whilst in current clamp mode, I injected a filtered and averaged membrane potential during the *in vivo*-like ramp into the soma of stellate cells *in vitro* under voltage clamp mode as a custom wave-form current via Axograph (Fig. 2.3A). I averaged the recordings from 5 different stellate cells with low series resistance (< 15 MΩ) to produce the current profile needed to be injected into the stellate cell to produce *in vivo*-like membrane potential dynamics.

In addition to the uncaging protocol for assessment of dendritic integration described above, I created depolarizing *in vivo*-like ramp (Fig. 2.3). Uncaging was performed at the peak of the ramp for both single and multiple synapse activation at exact same location in between little subthreshold wavelets riding on top of the ramp since subthreshold currents can alter the contributions of NMDA and AMPA receptors to synaptic currents (Seong et al., 2014). If the series resistance of the recording increased to > 15 MΩ, I scaled up the ramp accordingly so as to maintain membrane potential changes comparable to what was recorded *in vivo*.

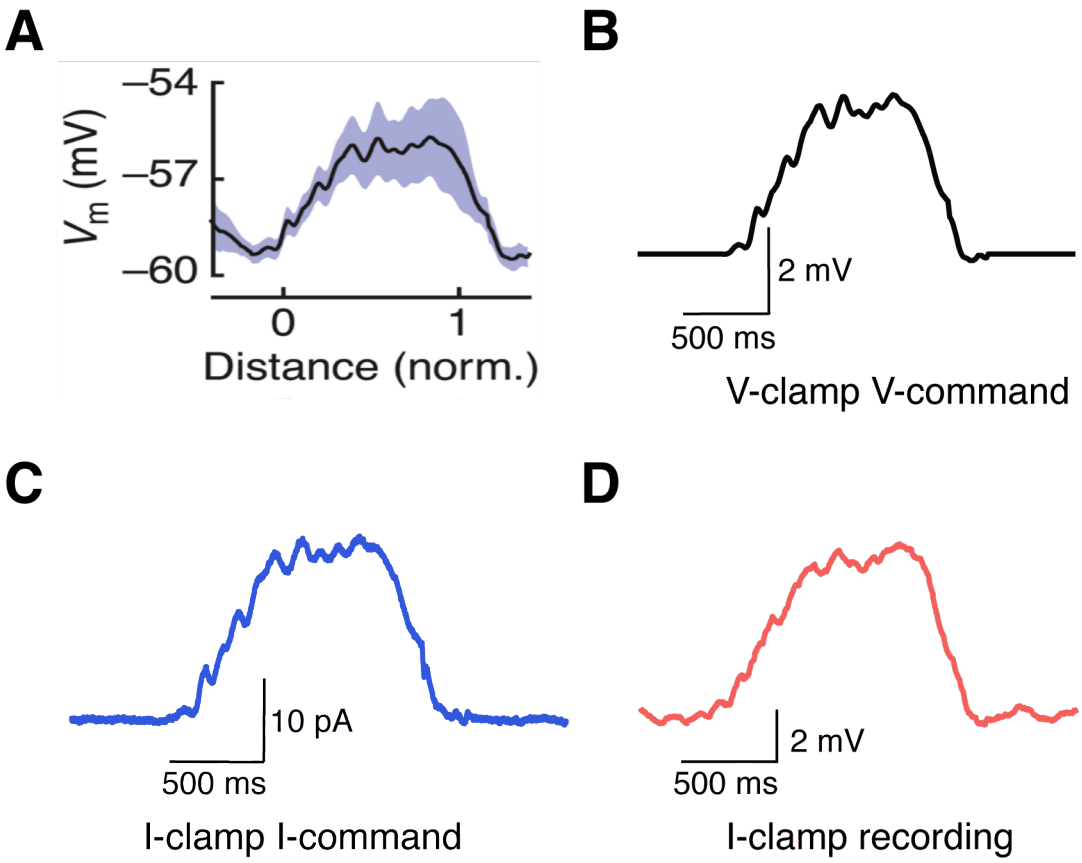

Figure 2.3 Creating *in vivo*-like membrane potential dynamics *in vitro*

A. Average membrane potential dynamics when the mouse crossed the grid cell field in the virtual reality environment (Schmidt-Hieber & Hausser, 2013). **B.** Voltage command (V-command) in voltage clamp (V-clamp), the same as in A. **C.** Current command (I-command), resulting from the V-clamp recording with V-command in B (average of recordings from 5 different cells). **D.** *In vivo*-like membrane potential dynamics induced in the stellate cell *in vitro* by injecting a current command in C (average from 5 traces in the same cell).

2.4 Data analysis

Data analysis was performed with custom code written in Python.

2.4.1 Input-output function

Step sEPSPs were added post-hoc to create hypothetical linear sum responses (Fig. 2.4C). Then linear sum amplitudes were plotted against the amplitudes of measured EPSPs corresponding to the same synapses (Fig. 2.4E) to assess if inputs were summated in a linear (diagonal line), supralinear (above the line) or sublinear manner (below the line). In this recording, summation is linear/slightly sublinear to start with and becomes supralinear activating 4 synapses or more.

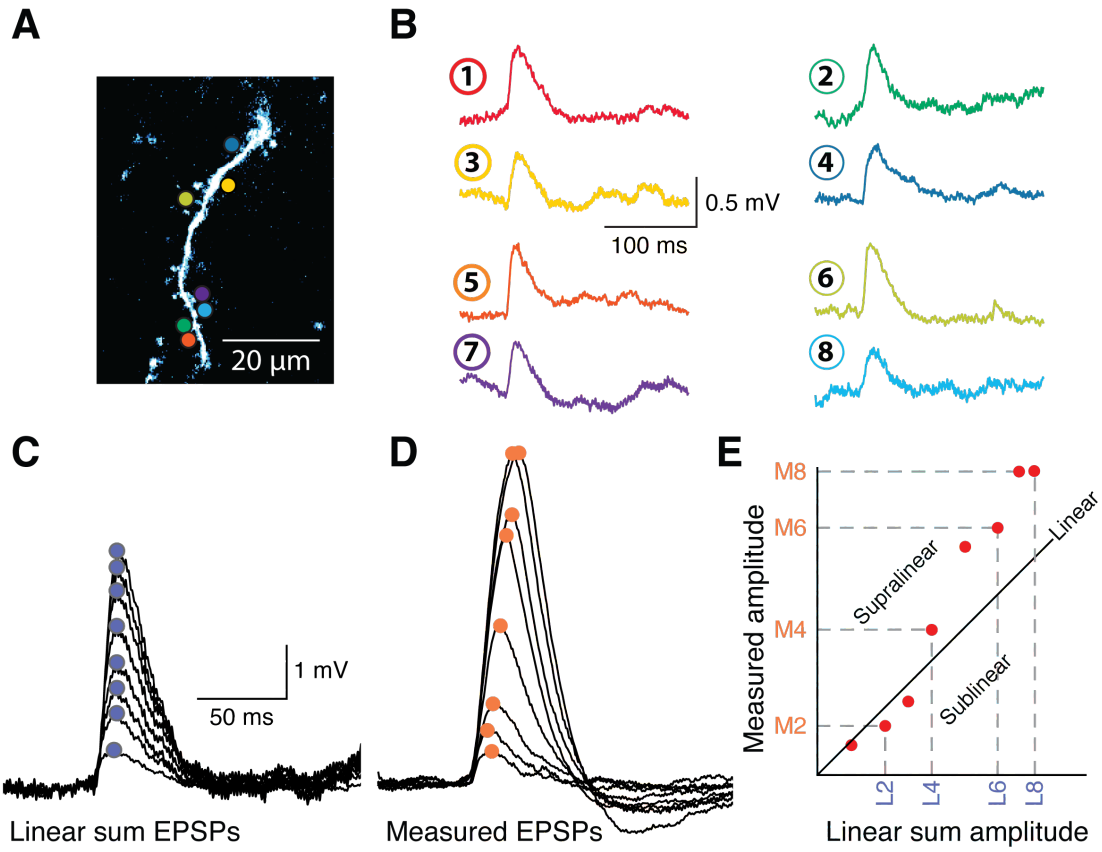

Figure 2.4 Measuring dendritic integration in single dendrites of stellate cells in MEC II

A. An Alexa 594-filled dendritic branch with the spots for uncaging marked in coloured circles. **B.** Single EPSPs (sEPSPs) recorded at the soma while uncaging each synapse individually. **C.** Linear summation of individual EPSPs. The peak of each linear sum EPSP is marked by a blue circle. **D.** EPSPs evoked uncaging on an increasing number of synapses measured at the soma. The peak of each EPSP is marked by an orange circle. **E.** Amplitudes of measured EPSPs plotted against amplitudes of linear sum EPSPs. The diagonal line indicates unity; the data points above that line indicate the recordings where summation was supralinear, those below mark where it was sublinear.

The nonlinearity was quantified by this equation:

$$Nonlinearity = \sum_{i=3}^{n} (\frac{M_i}{L_i} - 1)/(n-2)\ 100\%$$

where M_i was the amplitude of the measured EPSP, L_i was the amplitude of the EPSP constructed by the linear summation of single synapse EPSPs, n was the maximal number of synapses activated.

In some of experiments saturation of dendritic integration was detected, when increasing number of synapses activated no longer resulted in an increase of the EPSP amplitude. This was detected if the slope of linear regression curve (linregress function in scipy stats package in python) of the last 66.67% of recordings was less than 25% of the reference slope assessed by linear regression of the first 66.67% of recordings.

2.4.2 Identification of fast and slow dendritic spikes

Slow dendritic spikes were defined as events where the nonlinearity of the EPSP integral was 25% larger than the nonlinearity of the EPSP amplitude (Fig. 2.5), indicating the longer lasting active dendritic events.

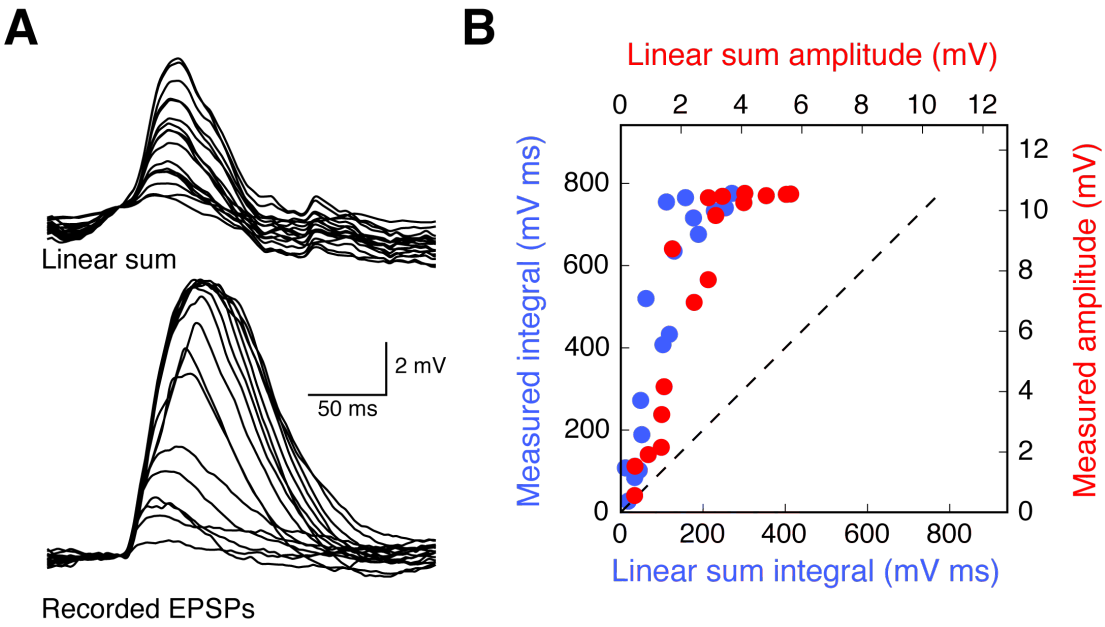

Figure 2.5 Identification of a slow dendritic spike

A. An example recording with a slow dendritic spike. Traces of linear summation (top) and of recorded EPSPs (bottom). **B.** Input-output function of the recording in A, for the integral (blue) and for the amplitude (red) or EPSPs. Here integral shows more supralinearity (left shifted) than amplitude of EPSPs.

Fast dendritic spikes were defined by the clustering of the peak of d^2V/dt^2 vs. time traces (Fig. 2.6). First, the peaks of d^2V/dt^2 traces were clustered using K-means of clustering (scipy.cluster.vq.kmeans2 function using 2 dimensions: time and d^2V/dt^2 value, Euclidean metrics) into 2 data clusters. Then the average and standard deviation were calculated in both dimensions (time (x) and d^2V/dt^2 (y)) for each cluster. A fast dendritic spike was identified if the difference between the means

of clusters was more than double the sum of standard deviations within clusters in both dimensions (equation below).

$$\sqrt{(M_{2x} - M_{1x})^2 + (M_{2y} - M_{2y})^2} > 2\,x\sqrt{SD_{1x}^2 + SD_{1y}^2} + 2\,x\sqrt{SD_{2x}^2 + SD_{2y}^2}$$

Where M_{1x} and M_{2x} were averages of the cluster 1 and cluster 2 in x dimension (time) and M_{1y} and M_{2y}, in y dimension, respectively (d^2V/dt^2). SD_{1x} and SD_{2x} were the standard deviation within cluster 1 and cluster 2 in x dimension, and SD_{1y} and SD_{2y} in y dimension, respectively.

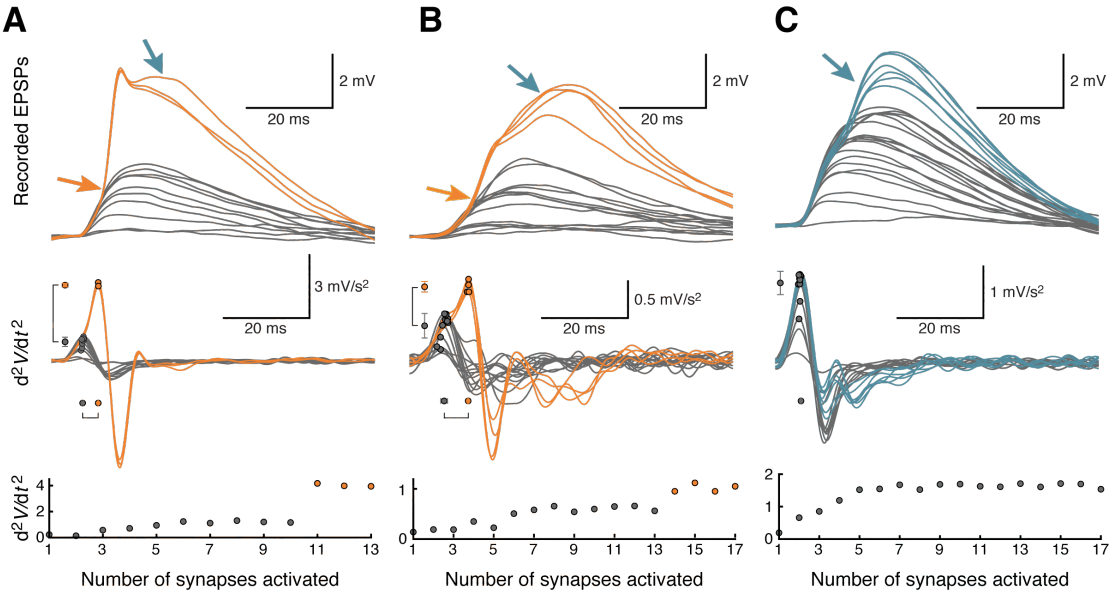

Figure 2.6 Identification of a fast dendritic spike by the d^2V/dt^2 peak

A. Some recordings exhibit very pronounced fast dendritic spikes (top traces in orange), which can be recognized by a big increase in maximal value of d^2V/dt^2 traces (middle and bottom). **B.** Most of recordings of fast dendritic spikes are less pronounced (top traces in orange), thus, can hardly be recognized by an increase in d^2V/dt^2 alone (bottom), but can be identified by taking time of d^2V/dt^2 peak into account by K-means clustering. Slow dendritic spikes often follow fast dendritic spikes (indicated in A and B by blue arrow), however, they can also occur

independently. **C.** Recording with a slow dendritic spike and d^2V/dt^2 traces of it included for comparison to fast dendritic spike traces.

2.4.3 Statistics

Statistical significance in comparisons of two data groups was assessed using Mann-Whitney *U* tests and Wilcoxon signed-rank tests for unpaired and paired data, respectively, with statistical significance defined as $p < 0.05$. Multiple comparisons were done using one-way ANOVA. Categorical data (such as fast and slow spike rates) were compared between the groups with Fisher's exact test. Data are presented as "mean ± SD". Error bars of dendritic spike proportions represent the SD of bootstrap analyses of the experimental data set (1000 repeats).

3. DENDRITIC INTEGRATION IN STELLATE CELLS OF MEC II

3.1 Introduction

The way inputs are summated in a neuron determines its functional suitability to perform specific computational tasks. Dendritic integration depends on factors such as cell morphology, the active and passive properties of the dendrites, the location of the inputs and other cell-type specific properties. Moreover, dendritic integration also depends on the characteristics of the inputs, such as their spatial and temporal distribution (Branco et al., 2010; Branco & Häusser, 2011). In recent years it has been found that dendritic integration of synaptic inputs can be distinct in different cell types. Pyramidal cells in the CA3 (Makara & Magee, 2013) and CA1 areas of the hippocampus integrate inputs in a highly nonlinear manner increased by the presence of dendritic spikes (Losonczy & Magee, 2006) while granule cells of the dentate gyrus show linear integration, strong attenuation of EPSPs and an absence of dendritic spikes (Krueppel et al. , 2011).

The rules governing dendritic integration in principal neurons of MEC II have not yet been assessed. There are two main types of principal neurons: stellate cells and pyramidal cells (Alonso & Klink, 1993), which differ in their morphology and electrophysiology (Alonso & Klink, 1993; Klink & Alonso, 1997). According to their morphological and basic electrophysiological properties, pyramidal cells of MEC II resemble pyramidal cells of other areas of the brain (Alonso & Klink, 1993; Klink & Alonso, 1997); thus, since dendritic integration is largely influenced by these properties, one might expect that MEC II pyramidal cells

should exhibit nonlinear integration as reported for pyramidal cells in CA1 (Losonczy & Magee, 2006), CA3, somatosensory and motor cortex (Branco & Häusser, 2011). However, stellate cells have a different dendritic morphology to pyramidal cells – 4-6 main long and thin dendrites with rather little branching. Stellate cells also have a larger soma (Klink & Alonso, 1997), and abundant expression of I_h current (Alonso & Klink, 1993). Taken together, these properties make it hard to predict the rules governing dendritic integration in these neurons.

Importantly, MEC II is the area where the majority of grid cells have been found (Hafting et al., 2005). When an animal explores an environment, these neurons fire action potentials at multiple locations, and these firing fields form a grid-like pattern. Due to these properties it has been proposed that grid cells play a crucial role in path integration and that they provide the neuronal basis for the "cognitive map" (McNaughton et al., 2006; O'Keefe & Nadel, 1978). Even though grid cells have also been found in other principal cell layers of MEC (Sargolini, 2006) and the pre- and parasubiculum (Boccara et al., 2010), the majority of grid cells are still thought to emerge from MEC II (Hafting et al., 2005).

Whether grid cells are stellate or pyramidal cells of MEC II is not yet known for certain; however, stellate cells are the main type of principal neuron in MEC II (Gatome et al., 2010) and some studies show that they possess grid-like firing properties (Burgalossi et al., 2011; Schmidt-Hieber & Hausser, 2013; Domnisoru et al., 2013; Zhang et al., 2013). Therefore, an investigation of the properties of the stellate cells of MEC II could suggest cellular mechanisms of grid cell firing (Garden et al., 2008; Giocomo et al., 2007). Knowledge about how stellate cells convert input arriving at their dendrites into action potential output is important for constraining existing and future theoretical models of the mechanisms of grid cell activity (Burgess et al., 2007).

In this chapter I describe my investigation of how the stellate cells of MEC II integrate inputs distributed onto their dendrites and how the spatial and temporal properties of the stimuli influence the input-output function of this cell type.

3.2 Results

3.2.1 Characteristics of uncaging-evoked EPSPs

I used two-photon glutamate uncaging to mimic synaptic transmission at single synapses in stellate cells. First, I measured miniature EPSPs in order to determine the properties of physiological EPSPs (Fig. 3.1A). Spontaneous miniature EPSPs (mEPSPs) were recorded at resting potential in stellate cells and had amplitude of 0.22 ± 0.1 mV on average, measured in the presence of tetrodotoxin (TTX). This was comparable to the amplitude of EPSPs triggered by two-photon glutamate uncaging, which averaged 0.33 ± 0.23 mV in control and 0.49 ± 0.32 mV in TTX (Fig. 3.1B and C, respectively).

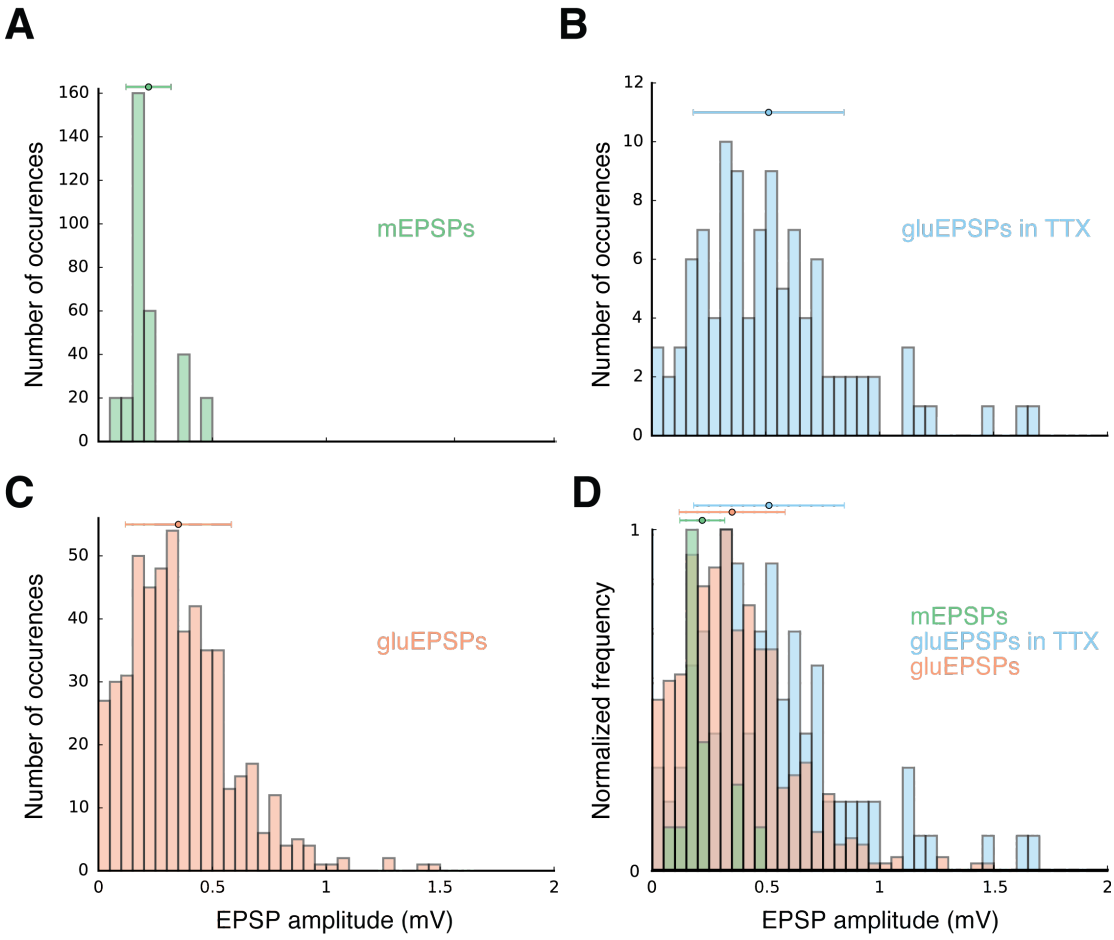

Figure 3.1 MNI-glutamate two-photon uncaging evoked EPSPs were at physiological amplitudes

A. Distribution of peak amplitudes of miniature EPSPs (mEPSPs), recorded in TTX. **B.** Distribution of peak amplitudes of EPSPs evoked by glutamate uncaging on single spines in TTX. **C.** Distribution of peak amplitudes of EPSPs evoked by uncaging on single spines. **D.** Uncaging-evoked EPSPs (blue and red) are comparable to mEPSPs. Frequency normalized to the maximal occurrences in one bin. Coloured dots represent the mean of the population and error bars represent SD.

3.2.2 Stellate cell input-output function of simultaneous synaptic inputs

Dendritic integration can be assessed by producing an input-output function (Fig. 3.2C) for a given dendrite by plotting the linear sum of individual EPSP peak amplitudes (Fig.3.2B top traces), obtained by summing the amplitudes of EPSPs resulting from single spine activation, against the peak amplitudes of measured EPSPs (Fig.3.2B bottom traces) while activating multiple synapses simultaneously (uncaging interval ≤ 1ms). I recorded from the soma while uncaging on 15 spines distributed within a 40 µm of a dendritic stretch (Fig.3.2A bottom image) located >50 µm from the soma of a stellate cell (Fig.3.2A top image). Dendritic integration of the first four sEPSPs was linear and became increasingly supralinear as more synapses were activated (Fig. 3.2C top).

In 34 recordings, I observed supralinear summation with a varying degree of supralinearity (0-200%, where 0% is linear summation) (Fig. 3.2C bottom and Fig. 3.9G). In the following part of this chapter I will be looking into different factors affecting this nonlinear summation with the aim of understanding the diversity and potential mechanisms mediating nonlinear summation, which I will discuss in greater detail in Chapter 4.

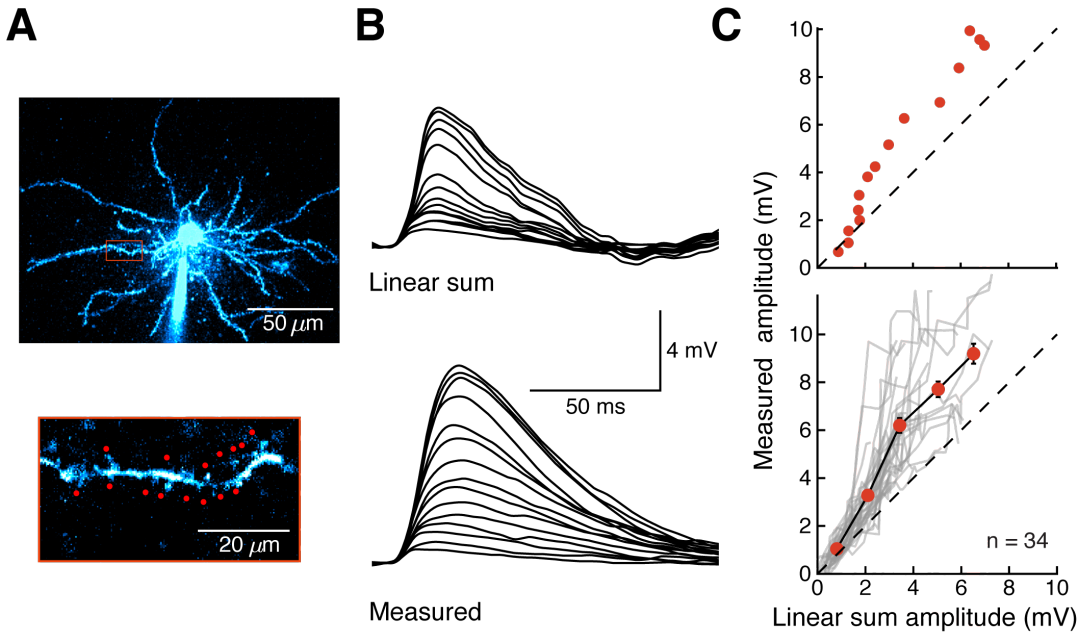

Figure 3.2 Supralinear integration of synaptic inputs in single dendrites of MECII stellate cells

A. A MEC II stellate cell filled with Alexa 594 dye (top) and a selected dendrite (bottom) with uncaging spots (red) at a higher magnification. **B.** Top traces show the linear sum of individual EPSPs (1 to 15 spines). Bottom traces show the responses to uncaging on an increasing number of spines at an interval of 0.6 ms between uncaging events. Amplitudes of measured responses are progressively larger than amplitudes predicted by linear summation. **C.** Amplitudes of somatically measured EPSPs were plotted against the amplitudes of the linear sum of corresponding individual spine responses. The black dashed line indicates unity, while the grey lines represent individual experiments and the solid black line connects averages across experiments (red dots). These averages were calculated for 5 bins equally distributed across the linear sum amplitude value range. Grey traces in the bottom plot shows recordings from 34 dendrites of 29 stellate cells.

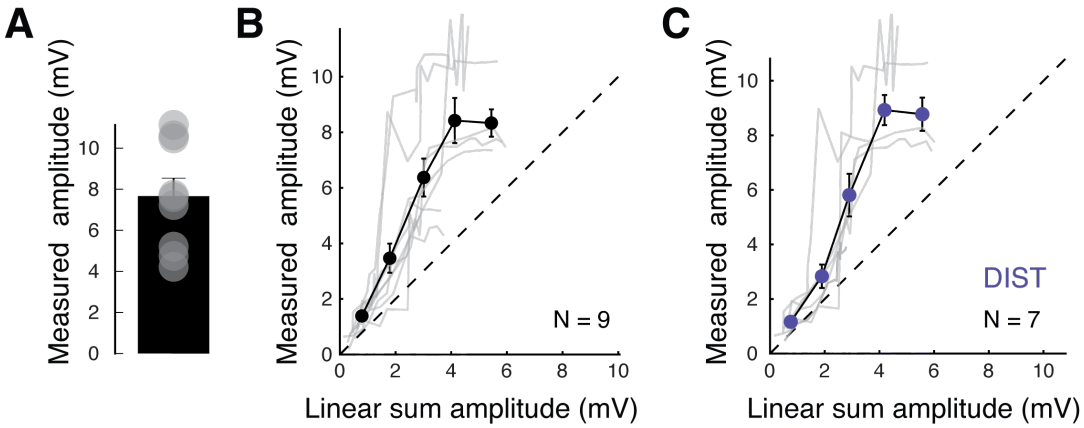

Figure 3.3 Examples of recordings showing saturation of increases in EPSP amplitude

A. Nine out of 34 recordings exhibited saturation, with EPSP amplitudes reaching 7.66 ± 0.88 mV, which was within the range of EPSP amplitudes without saturation (Fig. 3.2C bottom). **B.** Summary plot of nine saturating EPSPs; the grey lines represent individual recordings, the black dots represent binned averages and the error bars show SD. **C.** Summary plot of seven saturating EPSPs resulting from uncaging on distal dendrites; the grey lines represent individual recordings, the blue dots represent binned averages and the error bars show SD.

The somatic recordings were performed while uncaging at different locations along the dendritic tree. I classified dendrites < 60 µm from the soma as proximal (PROX), 60 – 120 µm as middle (MID) and > 120 µm as distal (DIST). Level of supralinearity was not significantly different uncaging on proximal, middle or distal dendrites (Fig. 3.4) (One-way ANOVA: P = 0.75, F = 0.29). Stellate cell dendrites can be longer than 300 µm (as estimated from (Ray et al., 2014) Fig.2), however, I was unable to perform uncaging experiments beyond 250 µm from the soma, since due to the radial morphology of the cell very distal parts of the dendrites were either cut during the slicing procedure (and these dendrites were not used in the experiment) or were located deep in the slice, where MNI-glutamate was not able to reach them. Moreover, I was

not able to obtain paired data from the distal and proximal parts of the same dendrite since due to the radial morphology of the dendritic tree I usually had a very short stretch of the dendrite superficial enough to the slice surface to be able to successfully uncage.

Input-output function of distal dendrites appears to be of a different shape to the proximal ones (Fig. 3.4). Distal inputs are summated with strong nonlinear boosting with saturation (sigmoidal shape) and proximal ones in "linear with gain" manner (similar to what has been reported in DG granule cells (Krueppel et al., 2011)). This has also been reported in neocortex layer II pyramidal cells (Branco & Häusser, 2011). Moreover, nine out of 34 recordings (Fig. 3.3B) exhibited saturation at around 8 mV (Fig. 3.3A), while increasing the number of synapses no longer resulted in an increase of the EPSP amplitude, where the majority of saturating recordings (7/9) were from the distal dendrites (Fig. 3.3C).

Activating a large number of spines (8 – 26, Fig.3.6C) on individual dendritic branches from a holding potential of -65 mV never resulted in the generation of action potentials. This can either suggest that activation of multiple synapses distributed in a longer stretch of the dendrite, or simultaneous inputs onto multiple dendrites are needed to make the cell fire. I have placed uncaging spots within a relatively short stretch of dendrite, which could have caused large local EPSPs, bringing the local membrane potential close to the AMPA and NMDA receptor reversal potential. Stellate cells have long and thin dendrites, and so they might exhibit high EPSP attenuation similarly to the granule cells of the dentate gyrus (Krueppel et al., 2011).

The maximal rate of rise (dV/dt) of EPSPs, evoked activating multiple synapses, was different at the population level between distal, middle

and proximal dendrites (PROX: 0.69 ± 0.29 V/s, MID: 0.56 ± 0.16 V/s, DIST: 0.55 ± 0.59 V/s (One-way ANOVA: $P = 0.02$, $F = 0.18$) (Fig. 3.5).

Uncaging on individual synapses evoked EPSPs of comparable amplitudes along the dendrite (Fig. 3.6). Individual EPSPs were on average 0.29 ± 0.21 mV, 0.37 ± 0.26 mV, 0.32 ± 0.20 mV for distal, middle and proximal dendrites (Fig. 3.6). The difference between EPSPs evoked in proximal and middle, and proximal and distal dendrites was not statistically significant (One-way ANOVA: $P = 0.83$, $F = 6.12$).

There was no correlation between supralinearity and the distance from the soma (Fig. 3.7A) at the range of distances assessed (18-210 μm) (linear regression: r = 0.23, P = 0.294 for 22 recordings). The degree of supralinearity of dendritic integration at proximal, middle and distal dendrites did not differ significantly ($P = 0.542$) and showed great variability within each population (Fig. 3.7D). Dendritic inputs were distributed on a small stretch of dendrite (27-70 μm) and there was no significant correlation (linear regression: r = -0.02, P = 0.920 for 34 recordings) between nonlinearity and maximal spread of uncaging spots (Fig. 3.7B) on nonlinearity. Moreover, there was no significant correlation (linear regression: r = 0.01, P = 0.951 for 34 recordings) between nonlinearity of dendritic integration and neither the maximal number of synapses activated per recording (Fig. 3.7C). EPSP amplitudes were not significantly correlated with nonlinearity of dendritic integration either (Fig. 3.7D) (linear regression: r = 0.11, P = 0.542 for 34 recordings).

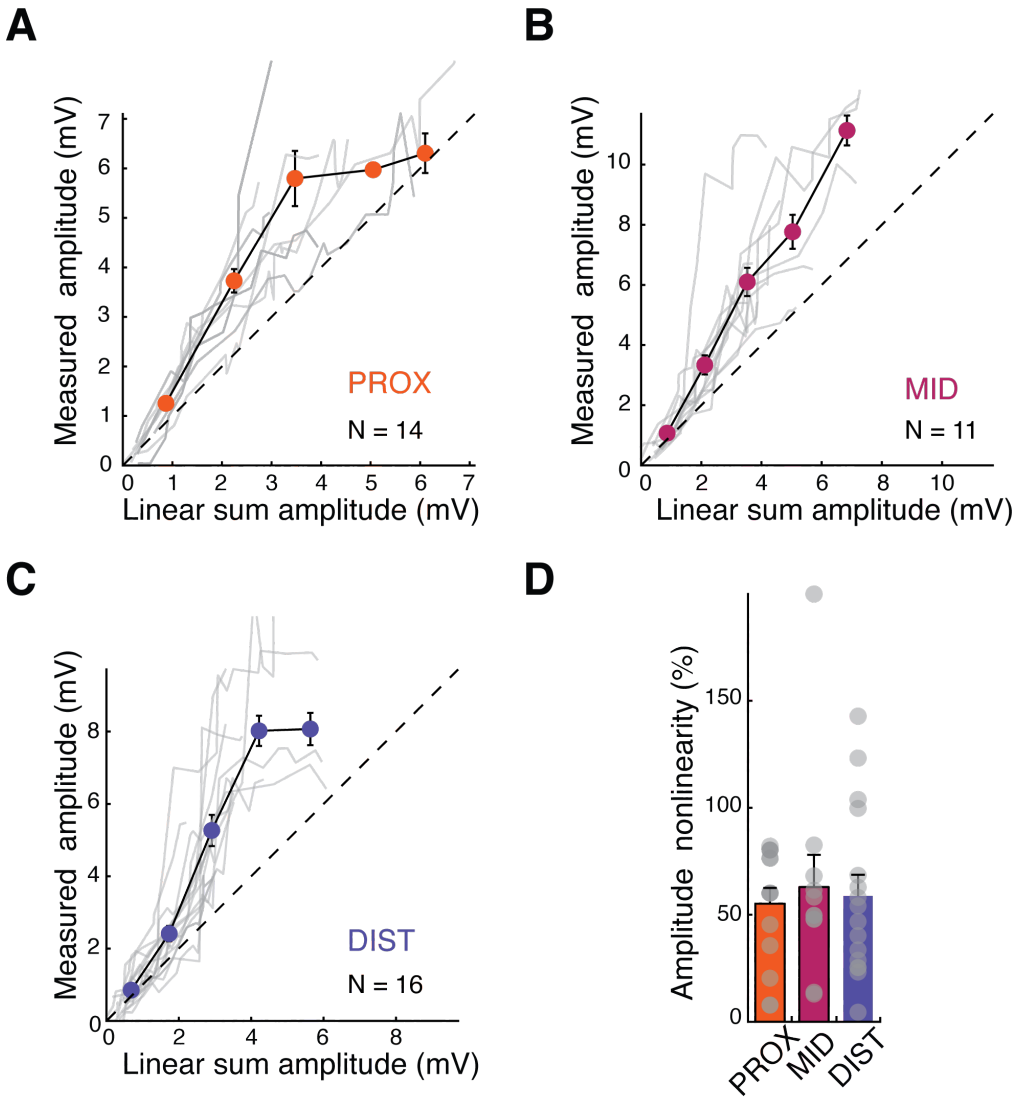

Figure 3.4 Supralinearity of dendritic integration in MEC II stellate cells does not depend on dendritic location

A. Summary of uncaging experiments on proximal dendrites (0 – 60 µm). The grey lines show individual experiments and the black line connects binned averages across 14 experiments. **B.** Summary uncaging experiments on middle dendrites (60 – 120 µm). The grey lines show individual experiments and the black line connects binned averages across 11 experiments. **C.** Summary of uncaging experiments on distal dendrites (< 120 µm). The grey lines show individual experiments and the black line connects binned averages across 16 experiments. **D.** Mean nonlinearity of dendritic integration does not significantly depend on dendritic location (One-way ANOVA: P = 0.75, F = 0.29).

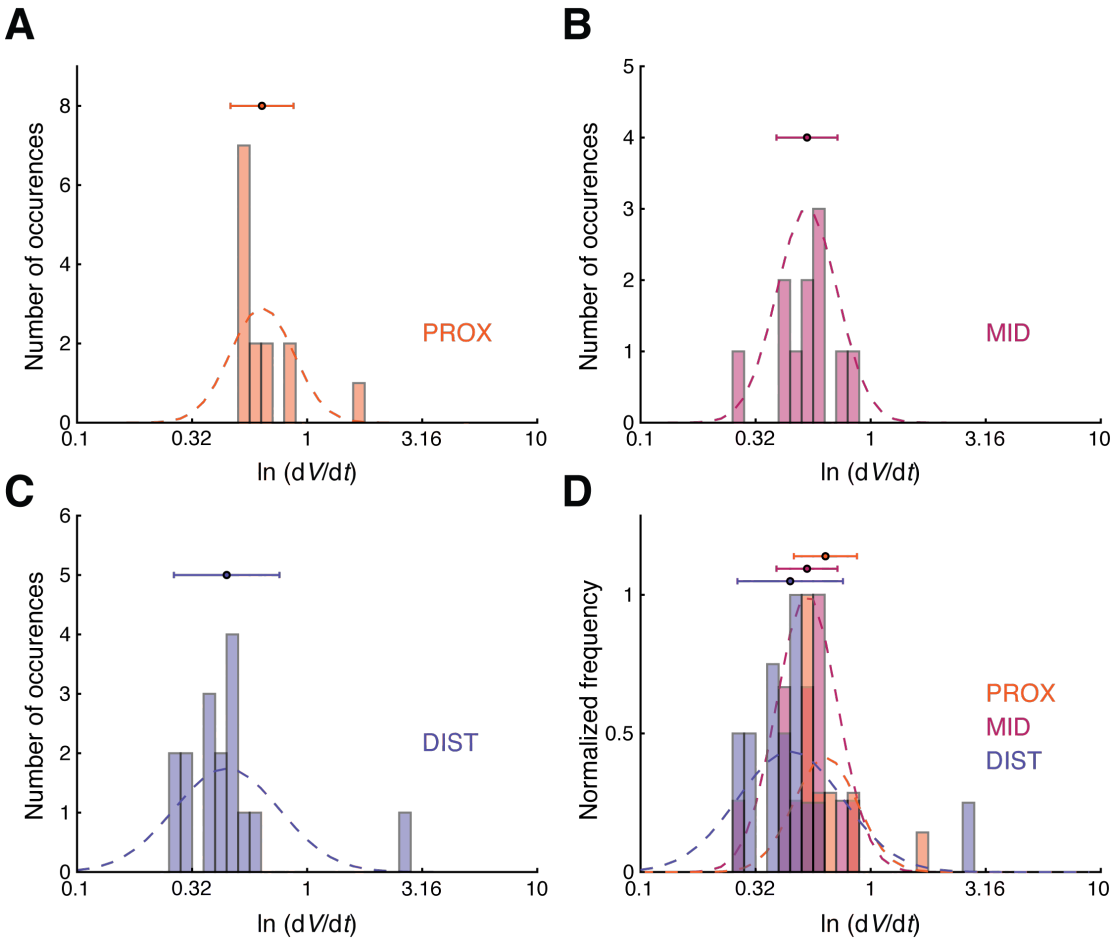

Figure 3.5 EPSPs evoked in proximal dendrites show a faster rate of rise than distally evoked EPSPs at the soma

A. Histogram of maximal rates of rise (d*V*/d*t*) for proximally evoked EPSPs, plotted semi-logarithmically for presentation purposes. **B.** Histogram of maximal d*V*/d*t* for middle dendrites. **C.** Histogram of maximal d*V*/d*t* for distal dendrites. **D.** EPSPs evoked in various locations on the dendrite differed in d*V*/d*t,* PROX: 0.69 ± 0.29 V/s, MID: 0.56 ± 0.16 V/s, DIST: 0.55 ± 0.59 V/s (One-way ANOVA: $P = 0.02$, $F = 0.18$).

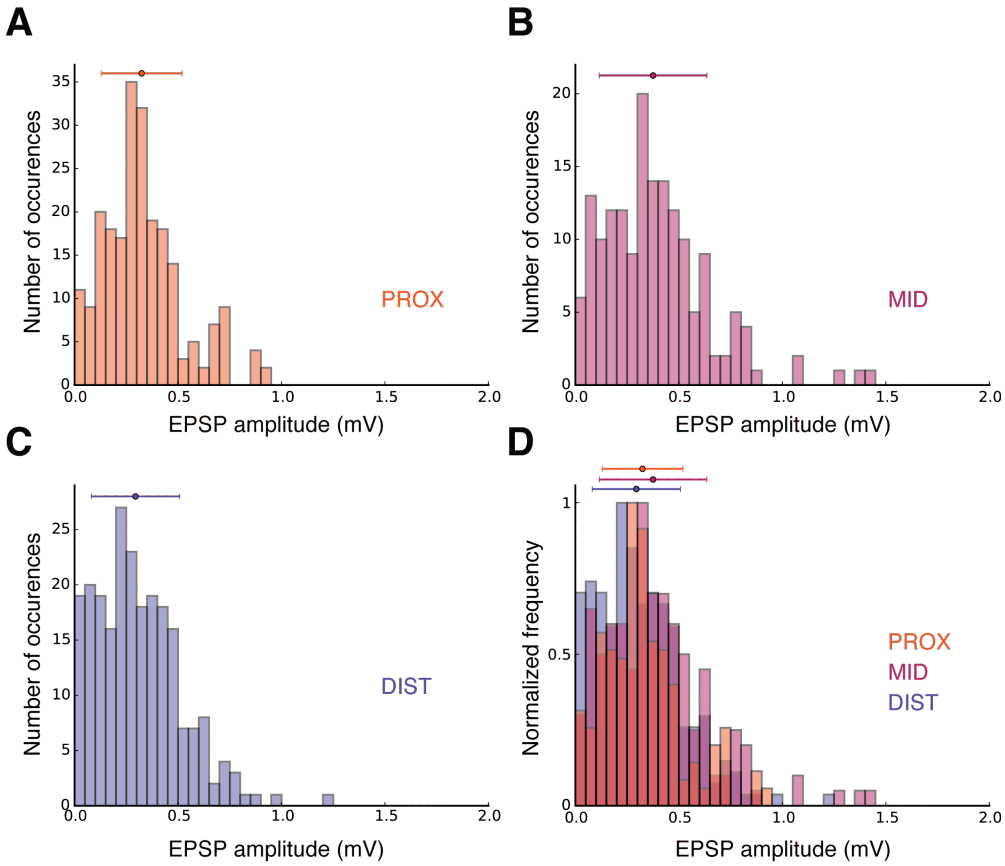

Figure 3.6 Amplitude of EPSPs evoked in different locations of the dendrite

A. Histogram of amplitudes for EPSPs evoked in proximal dendrites, measured at the soma. **B.** Histogram of amplitudes for EPSPs evoked in middle dendrites, measured at the soma. **C.** Histogram of amplitudes for EPSPs evoked in distal dendrites, measured at the soma. **D.** EPSPs evoked at different locations of the dendrite did not differ significantly (One-way ANOVA: $P = 0.83$, $F = 6.12$).

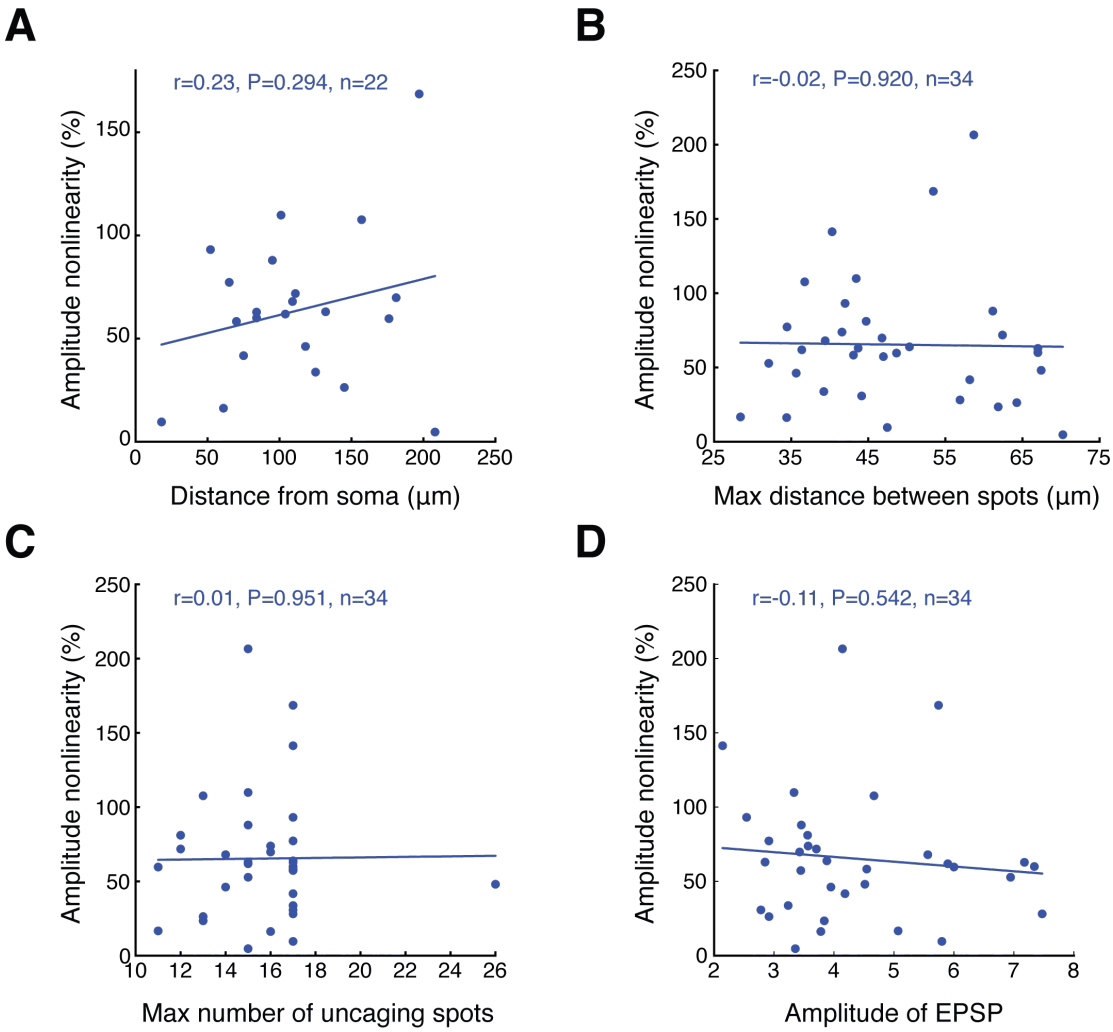

Figure 3.7 Supralinearity of dendritic integration does not depend on distance from the soma, EPSP amplitude, number of uncaging spots and spread of them

A. Amplitude nonlinearity plotted against the distance of the uncaging location from the soma. There was no significant correlation (linear regression: r = 0.23, P = 0.294 for 22 recordings). **B.** There was no significant correlation between amplitude nonlinearity and the maximal distance between uncaging spots (linear regression: r = -0.02, P = 0.920 for 34 recordings). **C.** There was no significant correlation between amplitude nonlinearity and the maximum number of uncaging spots (linear regression: r = 0.01, P = 0.951 for 34 recordings). **D.** There was no significant correlation between amplitude nonlinearity and the average amplitude of EPSP (linear regression: r = 0.11, P = 0.542 for 34 recordings).

Another factor which could influence dendritic integration is the dorsoventral position of the cell within MEC, as it has been shown that membrane properties of stellate cells differ along the dorsoventral axis (Garden et al., 2008). Nevertheless, the majority of recordings presented in this chapter have been obtained from the ventral half of MEC (Fig. 3.8). This mainly resulted from the fact that in my horizontal slices it was easier to find healthy cells with somas close to the surface of the slices in ventral than in dorsal slices. This may be explained by the larger cell bodies and dendritic trees and more widespread axons of the stellate cells (Garden et al., 2008) from dorsal MEC slices, which were consequently potentially easier to damage during the slicing process.

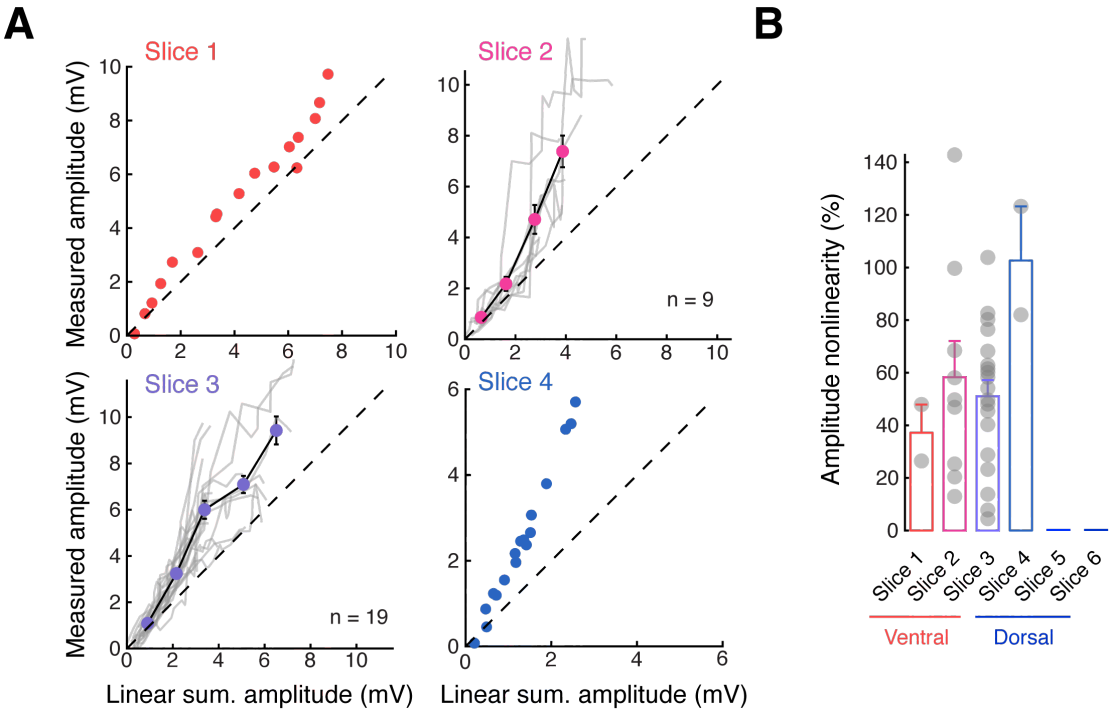

Figure 3.8 The majority of recordings were performed in the ventral half of MEC

A. Recordings from the slices 1, 2, 3 and 4. Due to the low number of recordings individual recordings are shown in the plots for slice 1 (red) and slice 4 (blue). The plots for slice 2 (pink) and slice 3 (violet) show a total of 9 and 19 recordings, respectively. 4 out of 34 recordings were

obtained from slices with dorsoventral location not recorded, thus, not included here. **B.** No significant difference in amplitude nonlinearity of dendritic integration was found within the ventral half of MEC. No successful recordings were obtained from the dorsal slices (5 and 6) since healthy stellate cells were closer to the slice surface in the ventral slices, thus, more suitable for uncaging experiments. Assessing differences between ventral and dorsal slices would require further recordings from dorsal slices, which were not obtained due to better.

3.2.3 Dendritic integration of non-simultaneous synaptic inputs

To better understand the temporal dynamics of the dendritic integration in MEC II stellate cells I increased the interval between uncaging pulses to 4 or 8ms (as opposed to a standard interval of 0.6 – 1ms during near-synchronous stimulation), what significantly reduced supralinearity (One-way ANOVA: P = 0.02, F = 4.22). Activating synapses at an interval of 4ms reduced supralinearity (Fig. 3.9A and B). Responses became linear at an interval of 8 ms (Fig.3.9 C, D and F). The differences at the population level of < 1ms and 8ms and 4ms and 8ms were statistically significant, < 0.001 and < 0.05 respectively (Mann-Whitney U test: P = 0.001, U = 20 and P = 0.04, U = 15).

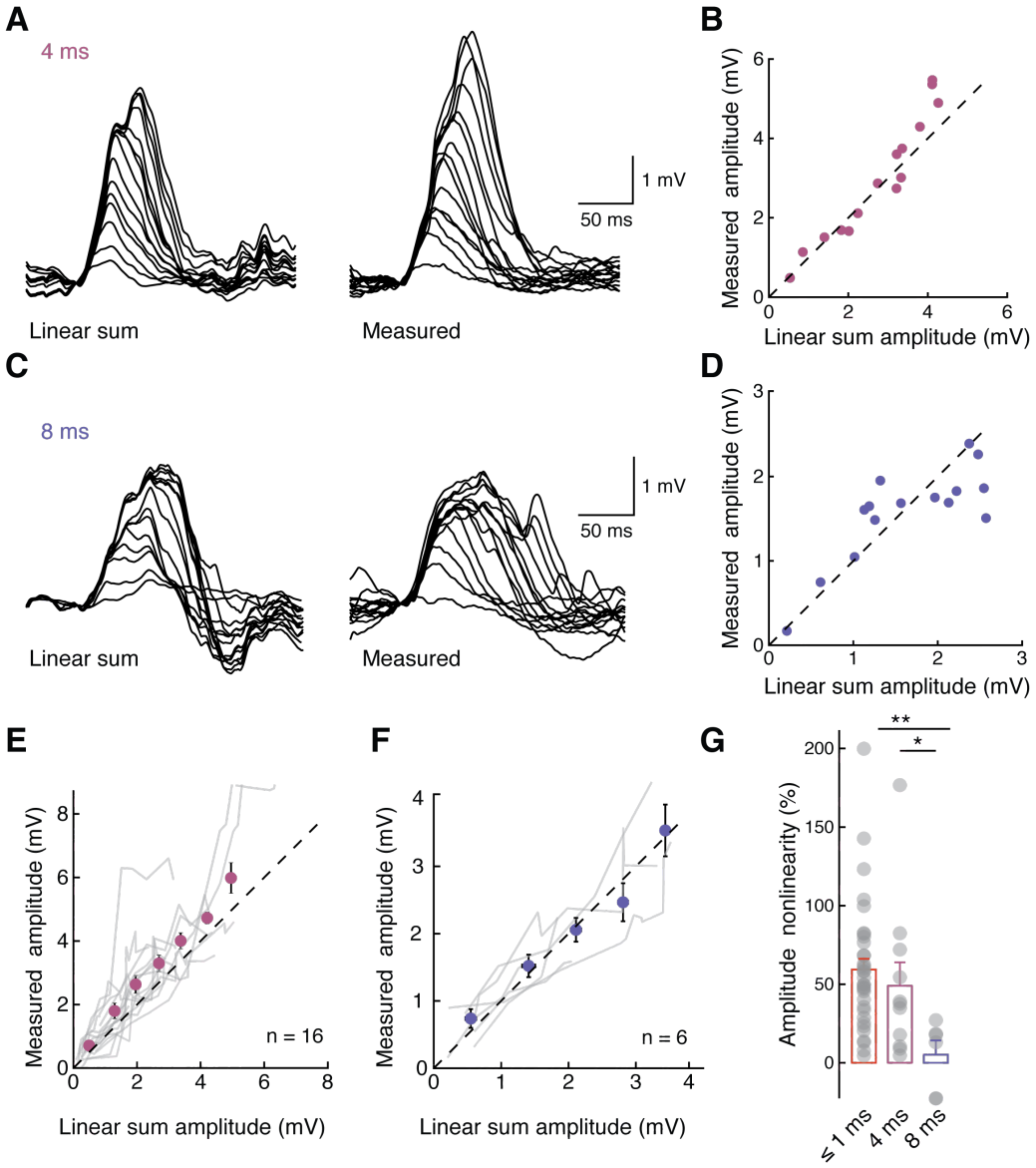

Figure 3.9 Dendritic integration in MECII stellate cells depends on the time interval between uncaging pulses

A. Linear sum and measured EPSPs obtained by uncaging on single dendrites with a time interval of 4 ms between uncaging pulses. **B.** Input-output curve of the recording in (A). **C.** Linear sum and measured EPSPs obtained by uncaging on single dendrites with a time interval of 8 ms between uncaging pulses. **D.** Input-output curve of the recording in (C). **D.** Summary of 16 recordings at a 4 ms time interval. **E.** Summary of 6 recordings at a 8 ms time interval. **G.** Nonlinearity depends on the time interval between uncaging events (One-way ANOVA: $P = 0.02$, $F = 4.22$). Nonlinearity was significantly

reduced between the recordings of 1ms and 8 ms intervals (Mann-Whitney U test: $P = 0.001$, $U = 20$) and 4 ms and 8 ms intervals (Mann-Whitney U test: $P = 0.04$, $U = 15$), but not between 1 ms and 4 ms (Mann-Whitney U test: $P = 0.12$, $U = 142$).

Temporal summation did not depend on the location of uncaging along the dendrite (Fig. 3.10). Proximal, middle and distal dendrites showed comparable amount of supralinearity uncaging at the same interval (Fig. 3.10 A, B and C). Also, there was a significant difference between uncaging at 1 ms and 8 ms interval between middle and distal dendrites (Fig. 3.10 E and F). Statistical significance could not be tested for the proximal dendrites since there was only one recording with 8 ms interval (Fig. 3.10 D).

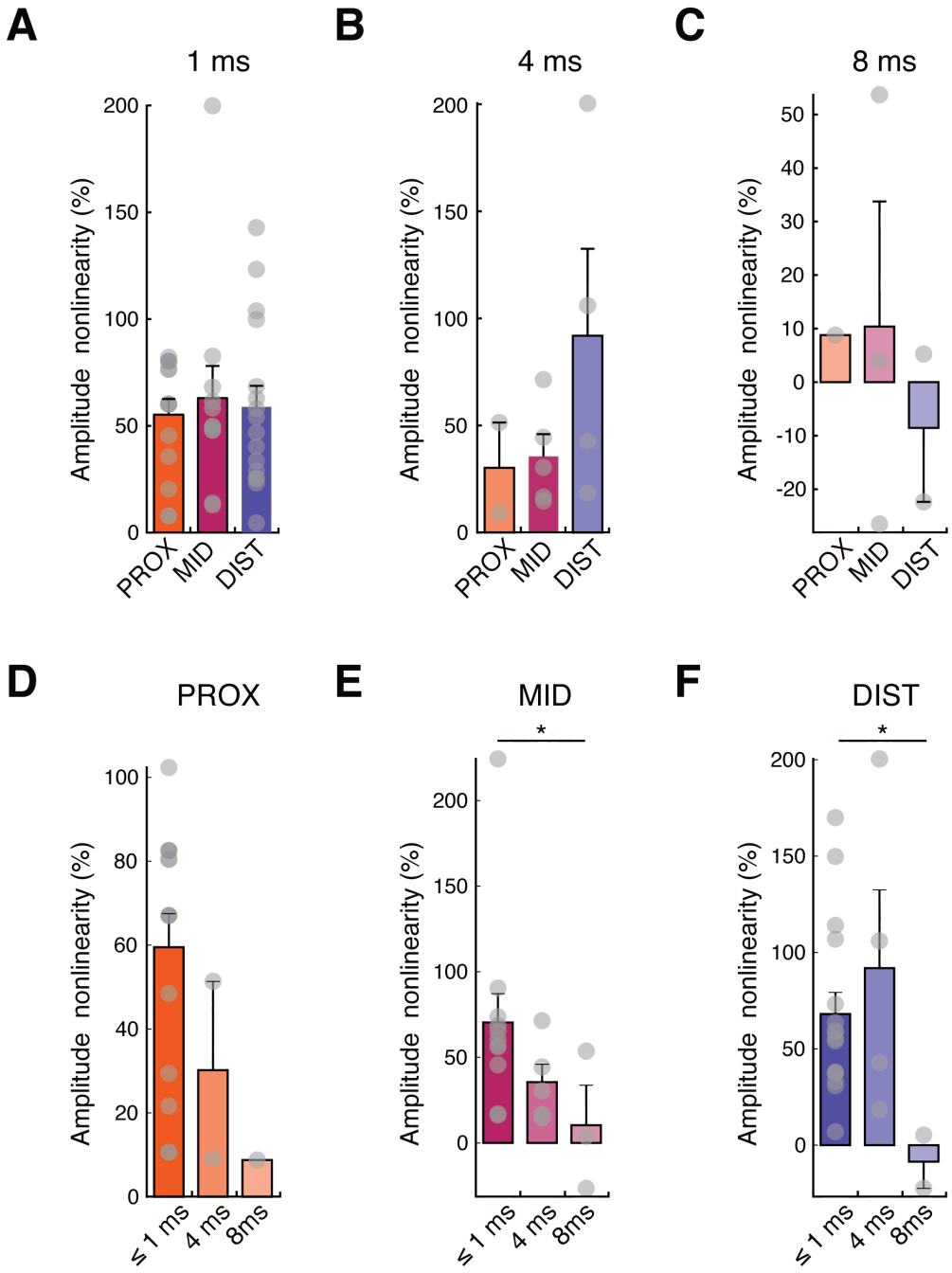

Figure 3.10 Dendritic integration in stellate cells at different dendritic locations with varying uncaging intervals

The nonlinearity of dendritic integration was not significantly different in proximal (PROX), middle (MID) or distal (DIST) dendrites for uncaging intervals of 1ms (One-way ANOVA: P = 0.75, F = 0.29) (**A**), 4ms (One-way ANOVA: P = 0.46, F = 0.85) (**B**) and 8ms (One-way ANOVA: P = 0.94, F = 0.06) (**C**). Nonlinearity was not significantly reduced increasing time interval between uncaging events when

analysing proximal (One-way ANOVA: P = 0.34, F = 1.17) (D) middle (One-way ANOVA: P = 0.12, F = 2.45) (**E**) and distal (One-way ANOVA: P = 0.22, F = 1.66) (**F**) dendrites for 1ms, 4ms and 8ms datasets. However, there was a statistically significant difference between 1 and 8 ms datasets for middle (Mann-Whitney U test: P = 0.03, U = 4) and distal (Mann-Whitney U test: P = 0.05, U = 4), but not proximal (Mann-Whitney U test: P = 0.15, U = 2) dendrites, probably because there was only 1 data point in 8 ms uncaging interval dataset of proximal dendrites.

3.3 Discussion

Here I have described that MEC II stellate cells summate nearly-synchronous inputs arriving at different locations within the dendritic tree in a supralinear manner. This is comparable to previous studies of nonlinear integration in pyramidal cells of neocortex layer II/III and layer V (Branco et al., 2010; Branco & Häusser, 2011), and also in pyramidal cells of the hippocampal CA1 (Losonczy & Magee, 2006) and CA3 (Makara & Magee, 2013) areas. The integration of inputs in MEC II stellate cells is different from the linear integration shown by the dendrites of dentate gyrus granule cells (Krueppel et al., 2011). The mechanisms underlying supralinear dendritic integration in MEC II stellate cells will be discussed in Chapter 4.

Increasing the time intervals between stimuli reduced supralinearity and the integration was linear when inputs were separated by intervals of 8ms. This might suggest stellate cell dendrites acting as coincidence detectors. Pyramidal cells of the neocortex layer II/III and V were reported to integrate distal inputs both more efficiently and via longer time interval (Branco & Häusser, 2011). In contrast, neither integration window nor level of supralinearity was significantly different in the MEC II stellate cells between distal, middle and proximal dendrites.

Moreover, amplitudes of individual EPSPs evoked at different locations were not significantly different, however, max rate of rise of EPSPs, evoked by activation of multiple synapses, were slowest for distal dendrites and fastest for proximal. Location independent EPSP amplitude and temporal summation has been previously reported in the apical dendrites of CA1 (Magee & Cook, 2000) and layer V pyramidal cells (Williams & Stuart, 2002). This phenomenon might be achieved via higher densities of synaptic conductances and higher input impedance in the distal dendrites (Nicholson et al., 2006) in order to normalize their somatic influence (Williams & Stuart, 2003).

Nevertheless, there seemed to be one difference between proximal and distal dendrites. Seven out of sixteen recordings from distal dendrites showed saturation, as opposed to only one out of fourteen of proximal and one out of eleven of middle dendrites. This might indicate that local EPSPs at the distal dendrites were large enough to bring the dendritic membrane potential close to the AMPA and NMDA receptor reversal potential and were strongly attenuated on their way to the soma due to the very long and thin morphology of the dendrites.

Strong attenuation of ESPSs on their path to the soma might also explain why uncaging on multiple synapses located on single branches of the stellate cell dendritic tree did not result in the generation of action potentials in the soma, similar to what has been observed in dentate gyrus granule cells (Krueppel et al., 2011). Other studies have shown that uncaging on single dendrites of neocortical and hippocampal pyramidal cells could evoke action potentials (Branco et al., 2010; Losonczy & Magee, 2006; Makara & Magee, 2013). This finding, together with the short supralinear integration window, suggests that coincident inputs to multiple dendrites of MEC II stellate cells might be needed to produce stellate cell output, what will be discussed in Chapter 5 of this thesis.

4. MECHANISMS UNDERLYING SUPRALINEAR DENDRITIC INTEGRATION IN MEC II STELLATE CELLS

4.1 Introduction

Having described the dynamics of dendritic integration in stellate cells of MEC II, the next step is to investigate the underlying mechanisms. There are a large number of studies investigating the mechanisms of dendritic integration in other cell types, which have been shown to depend on both the specific active and passive properties of each cell type. Here I will briefly describe the key findings of these studies. I will then cover what is known about active conductances in the membranes of MEC II stellate cells.

4.1.1 Mechanisms of nonlinearity in other cell types

Nonlinear dendritic integration has been well described for hippocampal and neocortical pyramidal cells, where dendritic patch clamp recordings have shown the presence of voltage-gated sodium (VGS) channels, voltage-gated calcium (VGC) channels and potassium channels in the apical dendrites of pyramidal cells. Sudden, large increases in dendritic EPSP amplitude in an all-or-none manner have been called dendritic spikes (D-spikes), and different types of D-spikes have been described according to the channels involved in their generation, such as VGS channels (Na^+ D-spike), VGC channels (Ca^{2+} D-spike) and NMDA receptors (NMDA D-spike) (Magee, 2000; Spruston, 2008).

Each type of voltage-gated channel has different voltage-dependent kinetics (activation and deactivation voltage, decay time constant etc.) associated with it. Moreover, there are a number of specific channel blockers, such as tetrodotoxin (TTX) for Na^+ channels, APV for NMDA receptors and Cadmium (Cd^{2+}) for Ca^{2+} channels, that can further help to identify the mechanisms of dendritic integration (Magee, 2000; Spruston, 2008). It is not yet known whether synaptic inputs to stellate cell dendrites can generate dendritic spikes. Below I will briefly discuss the characteristics of the different types of dendritic spikes recorded in other cell types, to provide a reference point for the interpretation of the data presented in this chapter.

4.1.2 Dendritic spikes

Due to the kinetics of VGS channels, Na^+ D-spikes usually have a fast onset, and thus they can be identified by a large increase in the rate of rise of the EPSP. Comparing paired recordings from the dendrite and the soma reveals that the Na^+ D-spike does not propagate well to the soma (Losonczy & Magee, 2006; Nevian et al., 2007) (Larkum et al., 2009), which can make it difficult to identify them from somatic recordings (Nevian et al., 2007).

NMDA D-spikes have a slower onset and decay, which may even be double the membrane decay time constant in some cell types (Larkum et al., 2009; J. Schiller et al., 2000b). Ion flux through NMDA receptor channels requires depolarization (e.g. mediated by AMPA receptor channels) to remove the Mg^{2+} block from the channel pore. Moreover, NMDA D-spikes are much less of an all-or-none phenomenon, instead showing a gradual increase leading to saturation (Antic et al., 2010; Larkum et al., 2009; Major et al., 2013). NMDA spikes also trigger a large influx of Ca^{2+} (J. Schiller et al., 2000b).

4.1.3 Active conductances in the MEC II stellate cells

Even though dendritic integration in MEC II stellate cells is not yet well understood, some research has been conducted on the active properties of these cells. Here I will briefly cover characteristics of the active conductances found in MEC II stellate cells, which are likely to contribute to nonlinear dendritic integration.

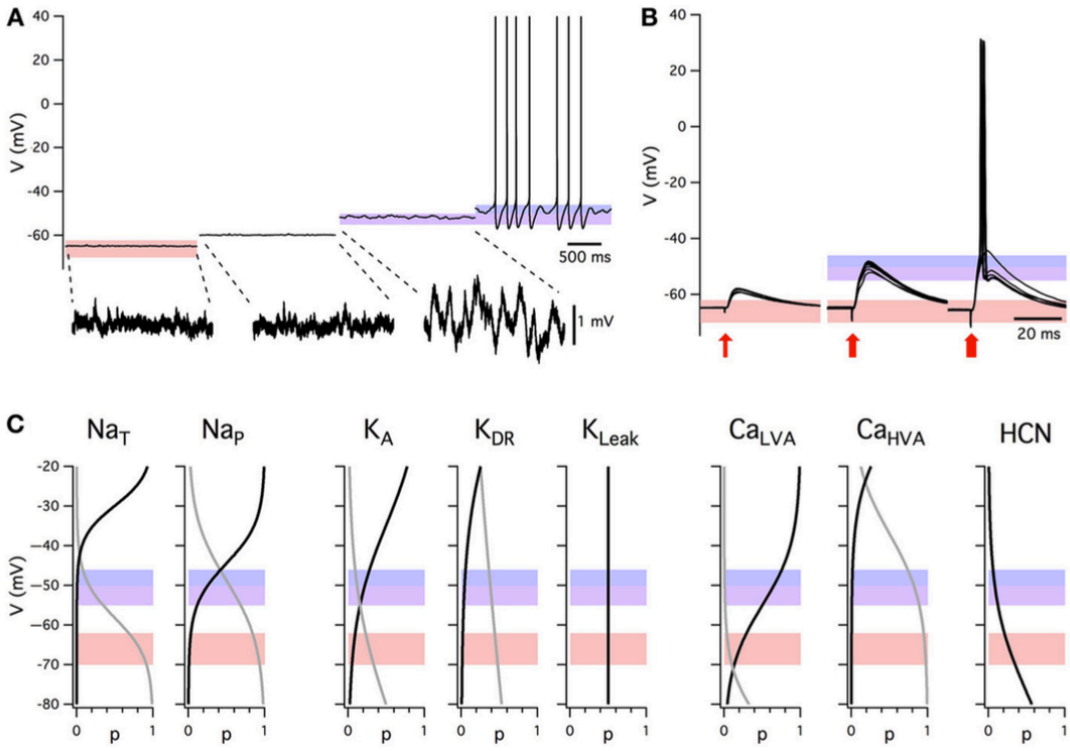

Figure 4.1 Summary of intrinsic electrophysiological properties of MEC II stellate cells

A. Membrane potential activity at rest and during steady state current injection. Pink shading represents the resting membrane potential, purple – under depolarization, blue – the threshold for action potential generation. B. EPSPs evoked by stimuli with increasing amplitude. C. Voltage dependence of different conductances of the MEC II stellate cells.

The black line represents activation, the grey line inactivation. (Adapted from (Pastoll et al., 2012))

Sodium currents in stellate cells

Different types of sodium conductances have been found in MEC II stellate cells to date. Transient sodium current (Na_T) is activated when membrane potential reaches –50mV or more (Fig. 4.1C 1st column), and has TTX sensitive and TTX insensitive components (Alonso & Llinás, 1989). Another type of sodium conductance found in stellate cells is voltage-gated persistent sodium current (Na_p), activating at about 10-15 mV more negative voltages than Na_T (Fig. 4.1C 2nd column). These channels have a larger single channel conductance (Magistretti et al., 1999b), inactivates relatively slowly (Magistretti & Alonso, 1999). Both Na_p and Na_T have been found in the dendrites of MEC II neurons (Magistretti et al., 1999a; 1999b; Pastoll et al., 2012), making them likely candidates for the nonlinear integration of dendritic inputs.

Calcium currents in stellate cells

2 types of calcium currents have been found in MEC II stellate cells so far: high-voltage activated (Ca_{HVA}) and low-voltage activated (Ca_{LVA}) calcium currents, activating at –50 mV and –60 mV, respectively (Fig. 3.1C) (Bruehl & Wadman, 1999; Visan et al., 2002). They both inactivate slowly and have different inactivation dynamics (Fig. 3.1C) (Bruehl & Wadman, 1999; Visan et al., 2002). Similar properties of calcium conductances have been found in both stellate and pyramidal cells of MEC II (Castelli & Magistretti, 2006).

I_h current in stellate cells

From the membrane potential response to current injection, it is known that stellate cells abundantly express hyperpolarization-activated current (I_h) (Fig. 3.1B) (Alonso & Klink, 1993). In fact, pharmacologically blocking hyperpolarization-activated cyclic nucleotide mediated (HCN) channels, which mediate I_h, by ZD7288 (Gasparini & DiFrancesco, 1997; Harris & Constanti, 1995) abolishes subthreshold oscillations (Dickson et al., 2000) that can be evoked in stellate cells by subthreshold depolarization (Alonso & Llinás, 1989). Moreover, a study of the electrical properties of MEC II stellate cells in HCN1 subunit knockout mice (Nolan et al., 2007) has revealed that I_h current shapes the resting membrane properties, since stellate cells in HCN1$^{-/-}$ mice had more hyperpolarized resting membrane potential, increased input resistance, a longer membrane time constant, decreased amplitude, and slower sag and rebound. In addition, I_h also affects the resonant properties of stellate cells by suppressing the responses that fluctuate at frequencies less than 4 Hz (Nolan et al., 2007). I_h is a relatively slow current, and in contrast to the other conductances mentioned, it activates by hyperpolarization (Fig. 4.1C last column) with its activation phase best described by a sum of 2 exponentials with time constants of ~ 80 ms and ~ 400 ms for fast and slow components, respectively, measured at –90 mV (Dickson et al., 2000; Nolan et al., 2007). Also, I_h slowly deactivates under depolarization (Nolan et al., 2007) (Fig. 4.1C last column). Since I_h has slow activation kinetics (> 100 ms) and is therefore unlikely to substantially contribute to the observed supralinearity of dendritic integration of nearly-simultaneously activated synapses.

Synaptic currents

In common with other types of excitatory neurons, EPSPs of MEC II stellate cells have fast AMPA and slower NMDA receptor mediated components, (Jones, 1994). They also receive inhibition via fast $GABA_A$ and slower $GABA_B$ receptors (Jones, 1994). The origin of the excitatory inputs to MEC II stellate cells is not yet well understood, but EPSPs can be elicited by stimulating MEC I (Alonso et al.,, 1990), as well as deeper layers of MEC and parasubiculum (Jones, 1994). How inputs arriving to the stellate cells of MEC II are integrated, and what mechanisms mediate this process is also largely unknown.

In this chapter I will present my findings on the mechanisms mediating nonlinear dendritic integration in MEC II stellate cells. The following experiments focus on active conductances that have previously been found to shape voltage responses in stellate cells.

4.2 Results

In some of the recordings putative dendritic spikes were detected in the somatic recordings, which I will describe in the following chapter. Later I will describe my data on blocking various conductances to identify the origin of supralinear summation and dendritic spikes.

4.2.1 Dendritic spikes

In some of the recordings (26% of recordings with uncaging interval < 1ms, Fig. 4.3A) fast dendritic spikes were observed (Fig. 4.2), which resembled Na^+ D-spikes recorded in other cell types (Losonczy & Magee, 2006). Some of these fast dendritic spikes were distinct and pronounced (Fig. 4.2A traces in orange) and easily detectable by a considerable sudden increase in max dV/dt (Fig. 4.2B). However, in other recordings,

fast D-spikes exhibited only a subtle change in max dV/dt (orange traces in Fig. 4.2C, Fig. 4.2D), thus, I have developed a method based on peak time and peak value of d^2V/dt^2 traces for fast spike identification (Chapter 2). Slow dendritic spikes were identified by 25% larger increase in the integral nonlinearity compared to the amplitude nonlinearity (Chapter 2).

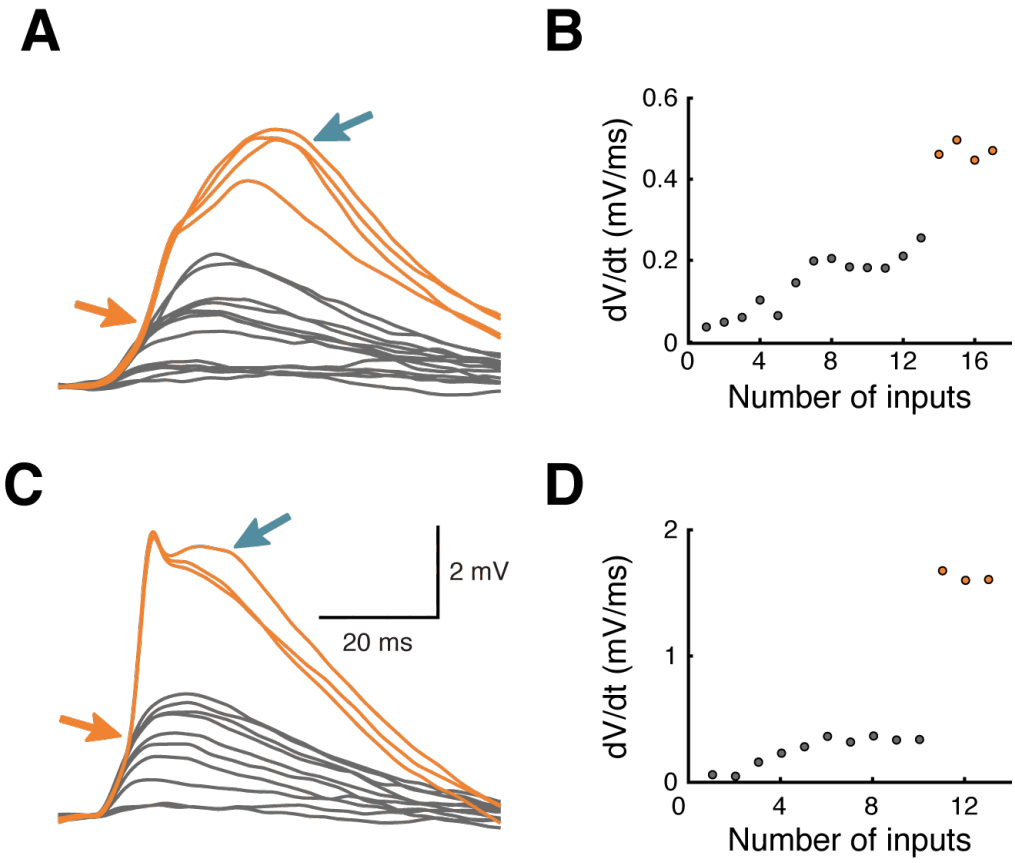

Figure 4.2 Some dendrites exhibit fast dendritic spikes, which are often followed by slow dendritic spikes

In some of somatic recordings fast and slow putative dendritic spikes can be detected, indicated by orange and blue arrows, respectively. In a subset of recordings, fast spikes are pronounced **(A)** and can be identified by an apparent increase in max dV/dt **(B)**. In other recordings, dendritic spikes are less pronounced **(C)** and only a small increase in max dV/dt is visible **(D)**.

Fast dendritic spikes could only be evoked with uncaging intervals ≤ 1 ms (Fig. 4.3A). Slow dendritic spikes were only found for uncaging intervals ≤ 4 ms (Fig. 4.3B).

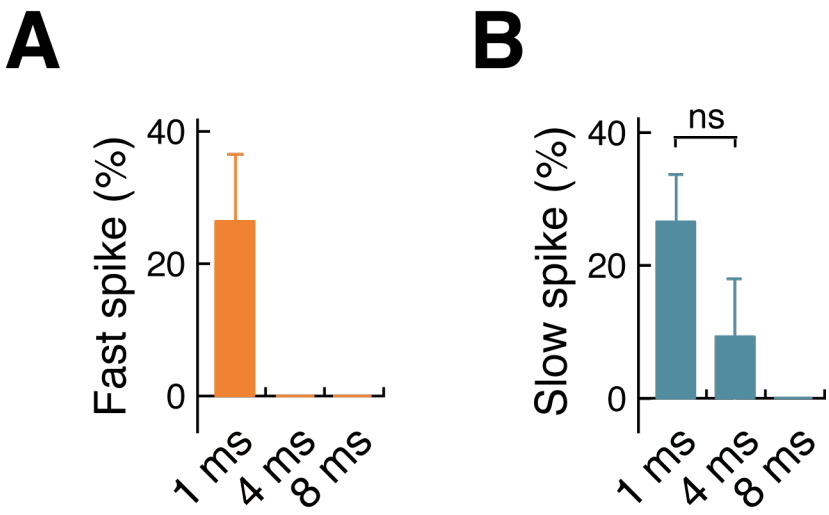

Figure 4.3 Fast and slow dendritic spikes are present only with near-synchronous stimulation

A. Fast dendritic spikes are present in 26% of all recordings at uncaging interval ≤ 1 ms, and are absent when interval is increased to 4 ms and 8 ms. **B.** Slow dendritic spikes are present in 26% of all recordings at uncaging interval ≤ 1 ms and 9% of recordings at 4 ms (Fisher's exact test: $P = 0.41$), and are absent when uncaging interval is increased to 8 ms.

A comparable proportion of slow and fast dendritic spikes were found at different uncaging locations along the dendrites (Fig. 4.4A for fast and Fig. 4.4B for slow spikes).

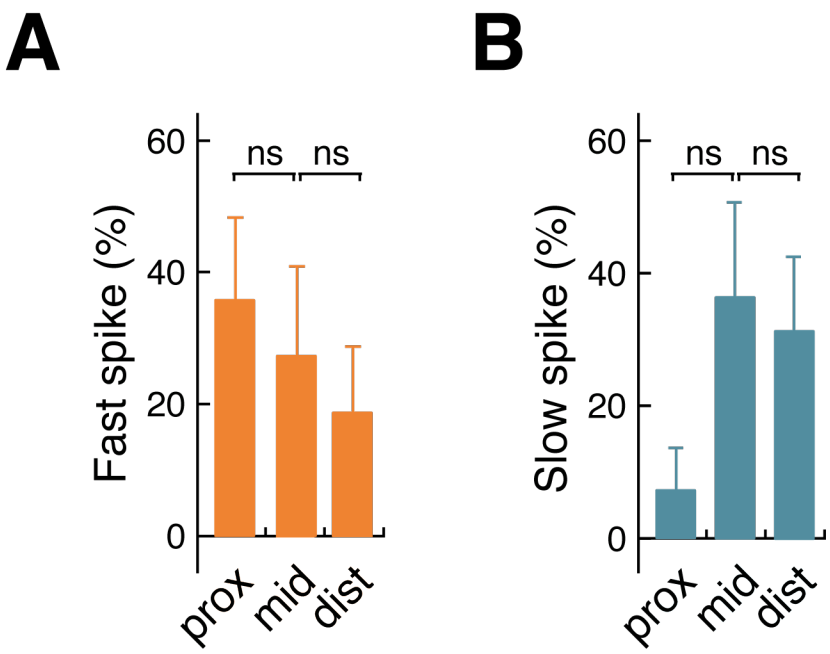

Figure 4.4 Fast and slow dendritic spikes can be generated at various locations along the dendrite

A. Fast dendritic spikes are present in 36% of all recordings uncaging interval ≤ 1 ms interval on proximal dendrites, 27% on middle dendrites, and 19% on distal dendrites. Proportion of fast dendritic spikes does not depend on the location on the dendrite (Fisher's exact test: PROX to MID: $P = 1.0$, PROX to DIST: $P = 0.42$, PROX to MID: $P = 0.66$). **B.** Slow dendritic spikes are present in 7% of all recordings uncaging at interval ≤ 1 ms on proximal dendrites, 36% on middle dendrites, and 31% on distal dendrites. Proportion of slow dendritic spikes does not depend on the location on the dendrite (Fisher's exact test: PROX to MID: $P = 0.13$, PROX to DIST: $P = 0.18$, PROX to MID: $P = 1.0$).

4.2.2 Pharmacology

To test which active conductances mediate supralinear dendritic integration, I blocked voltage-gated sodium channels (VGSCs) with tetrodotoxin (TTX), and NMDA receptors (NMDARs) with the NMDA receptor antagonist (2*R*)-amino-5-phosphonovaleric acid (APV), both separately and together, by bath application of these drugs at 0.5μM and

50μM concentrations respectively (Chapter 2). In the presence of TTX, some recordings still exhibited levels of supralinearity and occasionally slow dendritic spikes (Fig. 4.5A). However, in the presence of both APV and TTX or APV alone, inputs to the dendrites of the stellate cells of MEC II are summated in a linear manner (Fig. 4.5B and C).

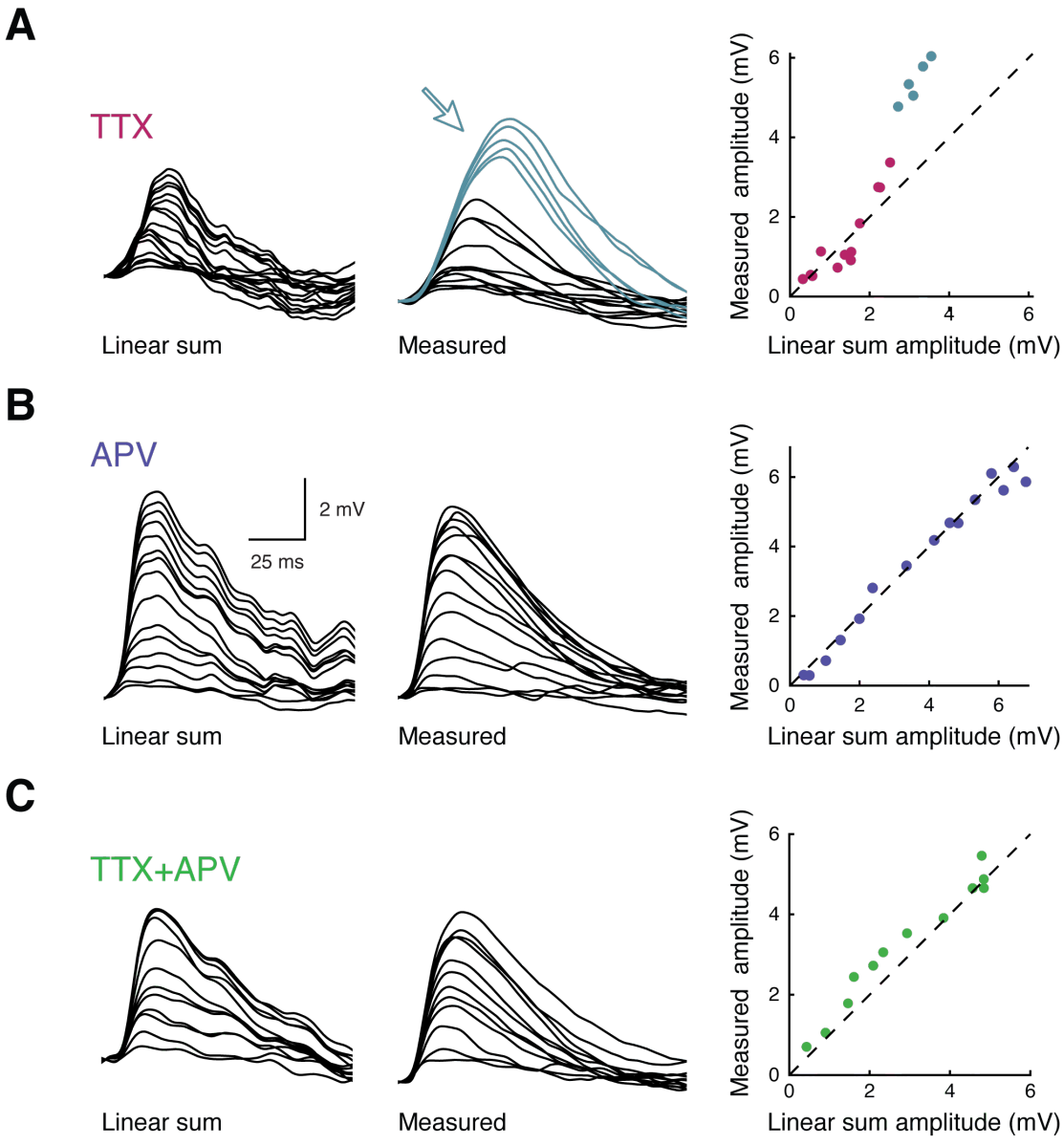

Figure 4.5 Dendritic integration after blocking VGS channels and NMDA receptors

A. Linear sum (left) and measured (middle) EPSPs and input-output function (right) of recording after blocking VGSCs with TTX. This recording still exhibits supralinear summation and slow dendritic spikes (blue traces and blue arrow). **B.** Linear sum (left) and measured (middle)

EPSPs and input-output function (right) of recording after blocking NMDA receptors with APV. In this recording summation is linear. **C.** Linear sum (left) and measured (middle) EPSPs and input-output function (right) of recording in APV and TTX. In this recording summation is linear.

Supralinearity was largely reduced in 7 recordings in the presence of TTX (Fig. 4.6A bottom left in pink) and completely abolished in 3 recordings in the presence of APV (Fig. 4.6A top right in violet), and 3 recordings in the presence of both APV and TTX (Fig. 4.6A bottom right in green) in comparison to control (Fig. 4.6A top left in red). Supralinearity was significantly different in the presence of TTX and in the presence of both TTX and APV (Fig. 4.6B) in comparison to control.

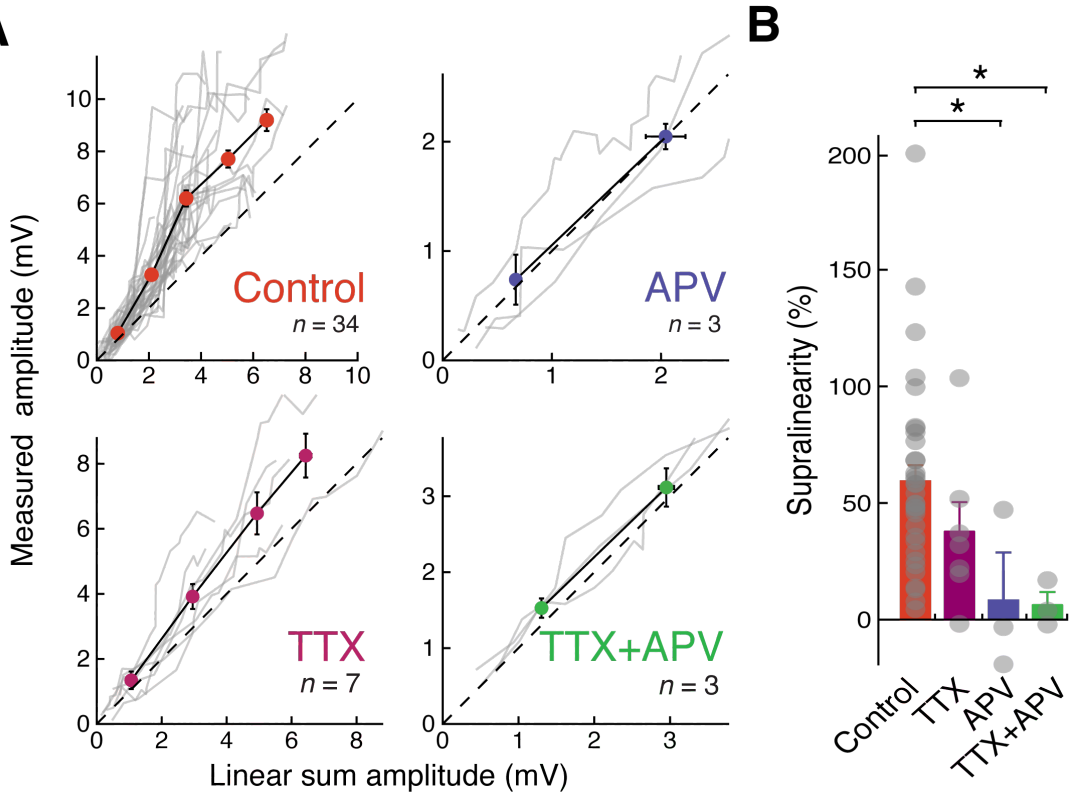

Figure 4.6 Supralinear dendritic integration is abolished by blocking VGS channels and NMDA receptors

A. Summary of the recordings in control (red, n=34), VGCCs blocked with TTX (pink, n=7) or NMDA Rs blocked with APV (violet, n=3), or VGCCs and NMDA Rs blocked with both TTX and APV (green, n=7).

Grey lines represent individual recordings and coloured dots are binned averages. **B.** TTX and APV significantly reduce nonlinearity of dendritic integration (One-way ANOVA: P = 0.03, F = 3.16). TTX and APV together abolish supralinear dendritic integration (Mann-Whitney U test: P = 0.02, U = 5), TTX alone (Mann-Whitney U test: P = 0.03, U = 66) and APV alone (Mann-Whitney U test: P = 0.02, U = 12) also significantly reduce it.

Moreover, fast dendritic spikes were completely abolished by TTX alone, APV alone, and TTX with APV in combination (Fig. 4.7A), while slow dendritic spikes were still present in TTX alone but not in APV alone or TTX with APV (Fig. 4.7B).

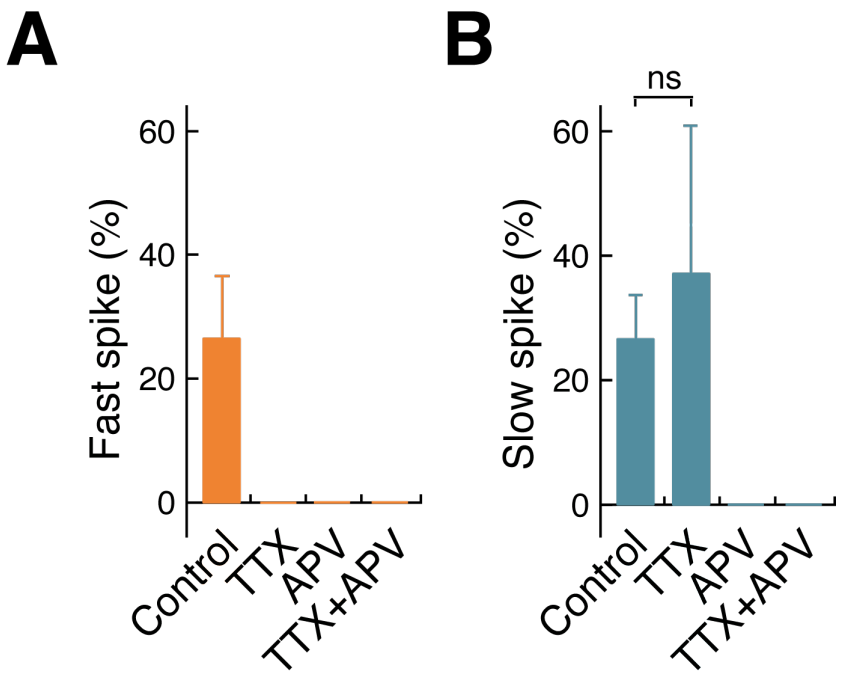

Figure 4.7 Dendritic spikes are blocked by TTX and APV

A. Fast dendritic spikes are present in 26% of all recordings and are absent when VGSCs are blocked with TTX, or when NMDARs are blocked with APV. **B.** Slow dendritic spikes are present in 26% of all recordings and persist when VGSCs are blocked with TTX (42 %), P = 0.4 (Fisher's exact test), but not when NMDARs are blocked with APV.

4.3 Discussion

Here I have shown that supralinear dendritic integration in MEC II stellate cells is mediated by voltage-gated sodium channels and NMDA receptors. Moreover, nearly-synchronous dendritic inputs are boosted by fast and slow dendritic spikes, which can be blocked by TTX and APV. This is the first report of dendritically triggered regenerative subthreshold events (putative dendritic spikes) in MEC stellate cells.

These mechanisms of supralinear integration are similar to previous studies in neocortical layer II/III pyramidal cells, where blocking VGSCs with TTX and, in another set of experiments L-type VGCCs with nifedipine, has partly reduced the supralinearity, and blocking NMDARs with APV was able to block supralinear summation completely (Branco & Häusser, 2011). Supralinearity in hippocampal CA3 pyramidal cells has also been found to be mainly NMDA receptor mediated (Makara & Magee, 2013).

In this chapter I have also shown that similarly to hippocampal CA1 (Losonczy & Magee, 2006) and CA3 (Makara & Magee, 2013) pyramidal cells, MEC stellate cells boost synchronous inputs with fast VGSC-mediated dendritic spikes, which are absent when inputs are more spread in time (Losonczy & Magee, 2006). In addition, dendritic spikes with a slower onset, resembling NMDA spikes in tuft dendrites of layer V pyramidal cells (Branco & Häusser, 2011) were also detected in MEC II stellate cells. Slow spikes persisted in the presence of TTX but were completely abolished by APV, however, suggesting them being NMDA spikes.

In contrast to other cortical neuron types (Branco & Häusser, 2011; Losonczy & Magee, 2006), somatic action potentials could not be evoked by uncaging on multiple dendritic spines of single dendritic branches of MEC II stellate cells. In the following chapter I will describe the conditions under which MNI-glutamate uncaging can evoke somatic action potentials.

5. INTEGRATION OF INPUTS FROM MULTIPLE DENDRITES AND DURING *IN VIVO*-LIKE MEMBRANE POTENTIAL DYNAMICS IN STELLATE CELLS

5.1 Introduction

Having assessed dendritic integration on a single dendritic branch of stellate cells at resting membrane potential (-65mV), we now wanted to examine how dendritic inputs are integrated under more realistic conditions, when a cell receives simultaneous inputs from multiple dendrites. Whole-cell patch clamp recordings in head-restrained animals navigating a virtual reality environment revealed a gradual depolarization of membrane potential that drives action potential output in grid cells when an animal crosses the firing field of the cell (Schmidt-Hieber & Hausser, 2013). How are dendritic inputs integrated on a single dendritic branch during *in vivo* membrane potential dynamics, potentially resulting from excitatory and inhibitory inputs to the dendrites and perisomatic region of a cell in a behaving animal (Domnisoru et al., 2013; Schmidt-Hieber & Hausser, 2013)?

In Chapter 3 I demonstrated that somatic action potentials could not be evoked by uncaging on multiple synapses (15-30) on a single dendritic branch, thus, I ask here whether stimulating inputs in a single dendrite during membrane potential at the *in vivo*-like levels of membrane potential depolarization could produce somatic action potentials. Furthermore, since spatiotemporal input dynamics during *in vivo* synaptic integration of stellate cells are not yet known, we next wanted

to determine how many dendrites needed to receive inputs to the synapses placed on them to evoke a somatic spike. In this chapter, I present my investigation of dendritic integration of multiple simultaneous inputs on a single dendritic branch during *in vivo*-like membrane potential dynamics, as well as the integration of inputs on two dendritic branches.

5.2 Results

The experiments described in this chapter have been conducted using two-photon glutamate uncaging on multiple synapses to either single (Chapter 5.2.1) or two dendritic branches (Chapter 5.2.2).

5.2.1 Dendritic integration of inputs to a single dendritic branch during somatic *in vivo*-like membrane potential dynamics

To assess dendritic integration during *in vivo*-like membrane potential dynamics, I aimed to reproduce membrane potential trajectories during firing field crossings recorded *in vivo* from mice navigating in a virtual reality environment (Schmidt-Hieber & Hausser, 2013). Action potentials were clipped from the *in vivo* data, traces were filtered as described in Schmidt-Hieber & Häusser (2013), and averaged over recordings acquired from 6 stellate cells. Next, I devised a procedure to obtain current waveforms that I could inject into the cell soma to produce a depolarizing *in vivo*-like membrane potential ramp in stellate cells *in vitro*. To achieve this, I used the *in vivo* membrane potential ramp as a voltage clamp command waveform, and recorded the clamp current (Chapter 2). I averaged recordings from 5 stellate cells with a series resistance of ≤10-15 MΩ, to obtain a final current waveform. Then I injected this current waveform into the soma of stellate cells in current-clamp mode to create *in vivo*-like membrane potential dynamics

(Chapter 2). Finally, I uncaged on an increasing number of synapses during the peak of the *in vivo*-like depolarizing ramp (Fig. 5.1A and B).

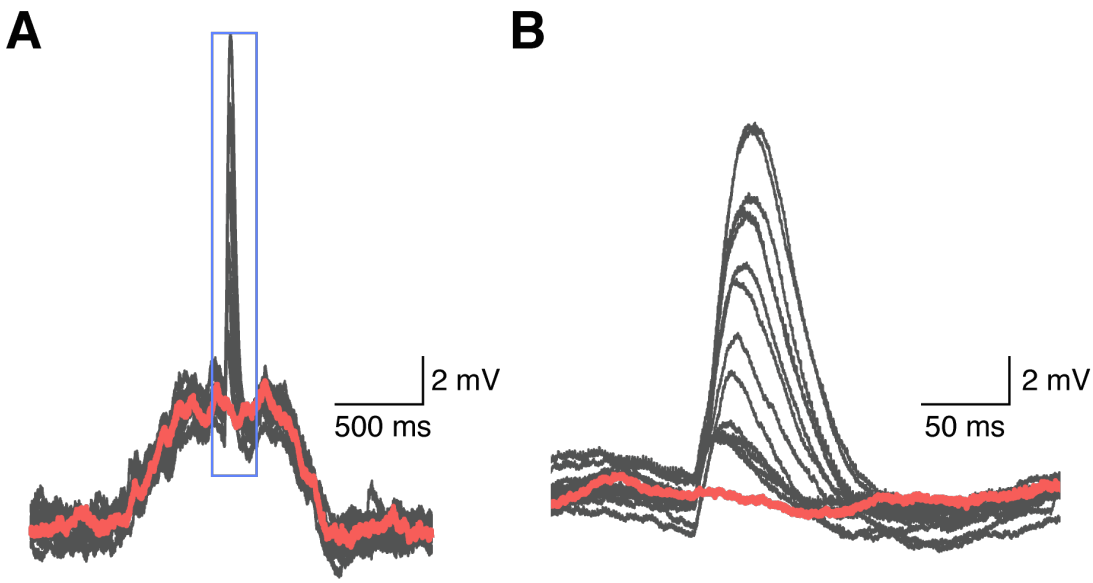

Figure 5.1 Generating *in vivo*-like membrane potential dynamics *in vitro*

A. EPSPs were evoked by uncaging an increasing number of inputs to a single dendritic branch at the peak of an *in vivo*-like ramp. Red trace represents *in vivo*-like ramp, grey traces – recordings of uncaging at the peak of the ramp. **B.** Uncaging evoked EPSPs on the peak of the ramp, at a higher magnification (blue box in C).

Using this approach I aimed to investigate the summation of inputs arriving at a single dendritic branch under *in vivo*-like conditions. Thus, as before, I first activated 10-15 inputs individually, and used this data to compute the linear sum of the individual responses. Next, I uncaged near-simultaneously on a gradually increasing number of synapses while recording membrane potential responses in the soma. In some of the cells, I acquired paired data at resting membrane potential (V_m = -65 mV) (Fig. 5.2A) and during *in vivo*-like membrane potential dynamics (*in vivo*-like ramp) (Fig. 5.2B). Thus, it was possible to directly compare the input-output functions of the cell under these different conditions (Fig. 5.2C). This example recording shows that supralinearity was larger during *in vivo*-like ramps in terms of the integral, but not in terms of the amplitude of EPSPs. Importantly, stimulation of 13 synapses on a single dendritic branch was sufficient to evoke somatic action potentials (Fig. 5.2 B right panel).

These results were consistent across 7 cells when comparing uncaging-evoked EPSPs at resting membrane potential (Fig. 5.3A for amplitudes and Fig. 5.3C for integral) and during *in vivo*-like membrane potential dynamics (Fig. 5.3B for amplitudes and Fig. 5.3D for integrals).

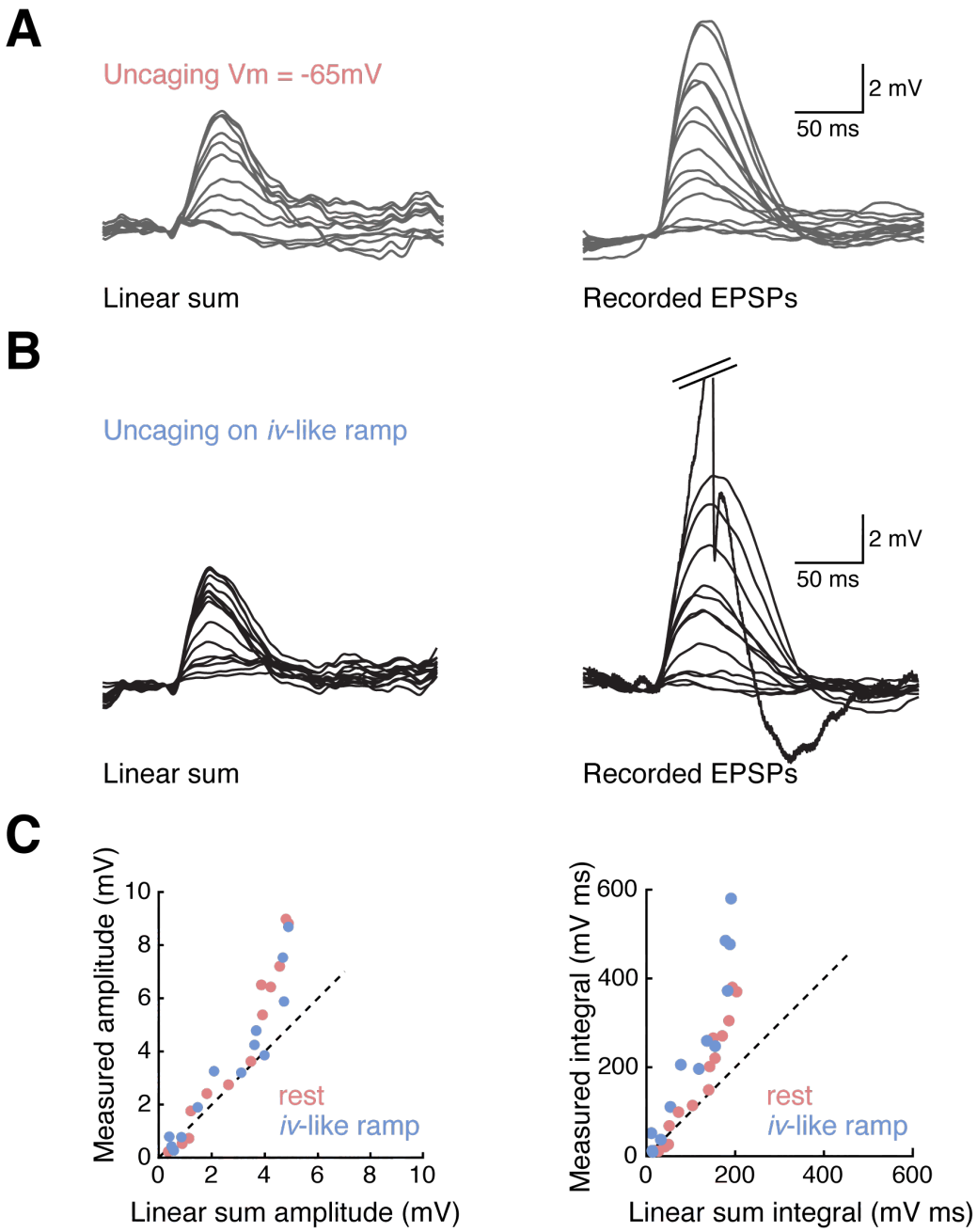

Figure 5.2 Uncaging *in vitro* during *in vivo*-like membrane potential dynamics

A. Linear sum (left) and recorded (right) EPSPs at resting membrane potential. **B.** Linear sum (left) and recorded (right) EPSPs during *in vivo*-like depolarizing membrane potential dynamics (*iv*-like ramp). Note: an action potential could be elicited by uncaging on 13 synapses on a single dendritic branch during *in vivo*-like membrane potential dynamics. **C.** *In vivo*-like membrane potentials increased the integral (right) but not the amplitude (left) of EPSPs.

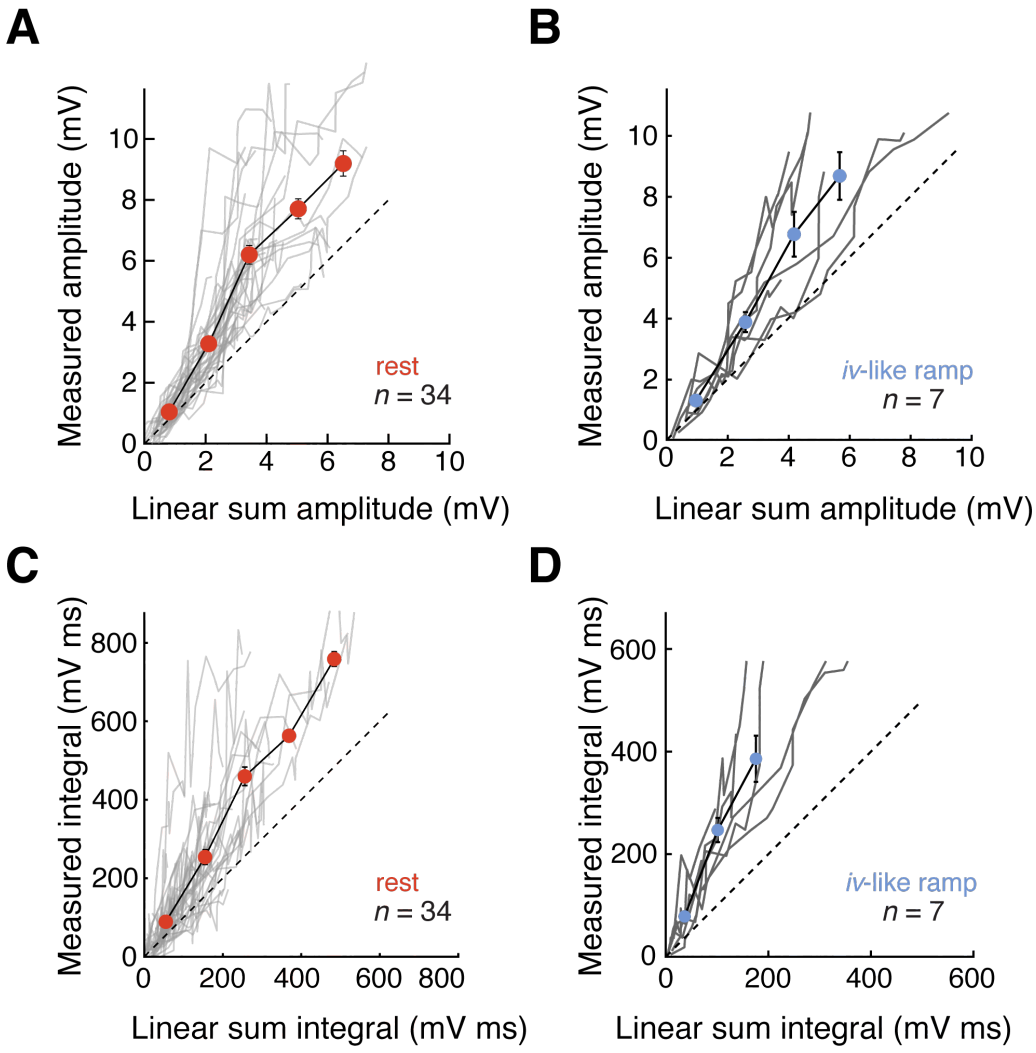

Figure 5.3 Uncaging during *in vivo*-like membrane potential dynamics boosts supralinearity of integrals of EPSPs

Summary plot of amplitudes (**A**) and integrals (**C**) at resting membrane potential (n = 34). Grey lines represent individual recordings, red dots represent binned averages. Summary plot of amplitudes (**B**) and integrals (**D**) during *in vivo*-like membrane potential dynamics (n = 7). Grey lines represent individual recordings, blue dots represent binned averages.

There was a significantly larger nonlinearity of the integral during *in vivo*-like membrane potential dynamics than at resting membrane potential (Fig. 5.4B) (Mann-Whitney *U* test: $P = 0.01$, $U = 53$), however,

the amplitude nonlinearity was not significantly different (Fig. 5.4A) (Mann-Whitney *U* test: $P = 0.616$, $U = 61$)..

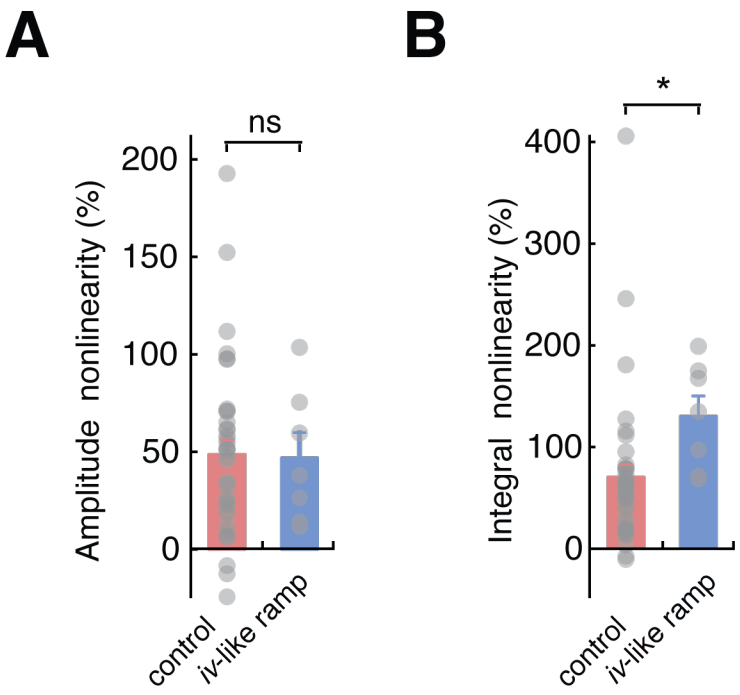

Figure 5.4 Nonlinearity of dendritic integration is significantly larger in terms of integrals but not amplitudes of EPSPs during *in vivo*-like ramps

A. Summary of amplitude nonlinearity of individual recordings (grey dots) and population average when uncaging at resting membrane potential (Control) and during *in vivo*-like membrane potential ramp (*iv*-like ramp) (Mann-Whitney *U* test: $P = 0.616$, $U = 61$). Pink and blue bars represent population average for Control and *iv*-like ramp data, respectively. **B**. Summary of integral nonlinearity of individual recordings (grey dots) and population average for uncaging at resting membrane potential (Control) and during *in vivo*-like membrane potential dynamics (*iv*-like ramp) (Mann-Whitney *U* test: $P = 0.01$, $U = 53$). Pink and blue bars represent population average for Control and *iv*-like ramp data, respectively.

A significantly larger proportion of slow ($P = 0.014$, Fisher's exact test) but not fast ($P = 0.940$, Fisher's exact test) dendritic spikes occurred

during *in vivo*-like depolarizing ramps compared to recordings at resting membrane potential (Fig. 5.5 A and B).

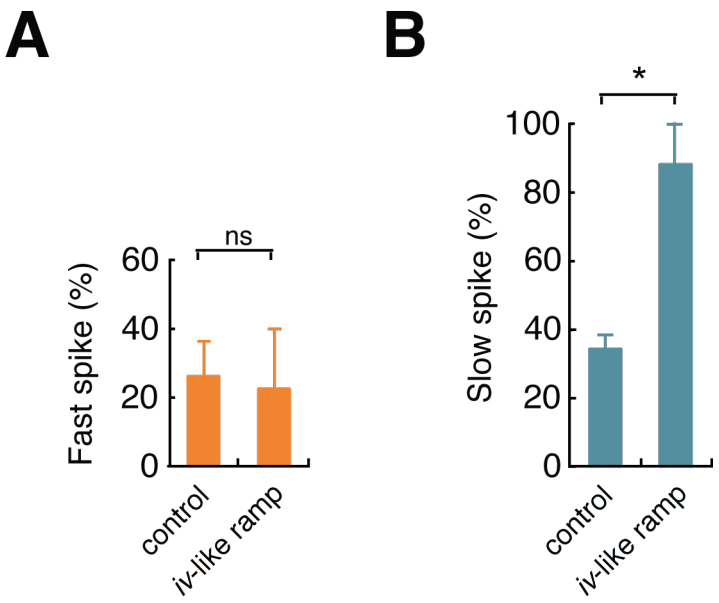

Figure 5.5 *In vivo*-like membrane potential dynamics results in increased occurrence of slow dendritic spikes

A. Proportion of fast dendritic spikes at resting membrane potential (Control) and during *in vivo*-like depolarizing ramps (*iv*-like ramp) (Fisher's exact test: $P = 0.940$). **B**. Proportion of slow dendritic spikes (Fisher's exact test: $P = 0.014$) at resting membrane potential (Control) and during *in vivo*-like depolarizing ramps (*iv*-like ramp).

5.2.2 Dendritic integration of inputs from two dendritic branches

I next investigated how inputs arriving at multiple dendritic branches are integrated, as well as how many dendrites need to be activated to make a cell fire, given that it is impossible to induce somatic spikes by uncaging on a single dendritic branch at resting potential. To address these questions I activated synapses on adjacent dendritic branches.

This experiment was challenging and had a low yield due to the morphology of the dendritic tree of stellate cells, as it was rare to find 2 branches of the same dendritic subtree within a field of view in the same focal plane. Nevertheless, in the recordings acquired I could substantially boost EPSP amplitude by uncaging on 2 branches (Fig. 5.6) and, in some cases I could induce somatic action potentials (Fig. 5.7). In the Fig. 5.7 thought both dendritic branches are very close together and signal cross contamination might be the reason of such high levels of supralinearity.

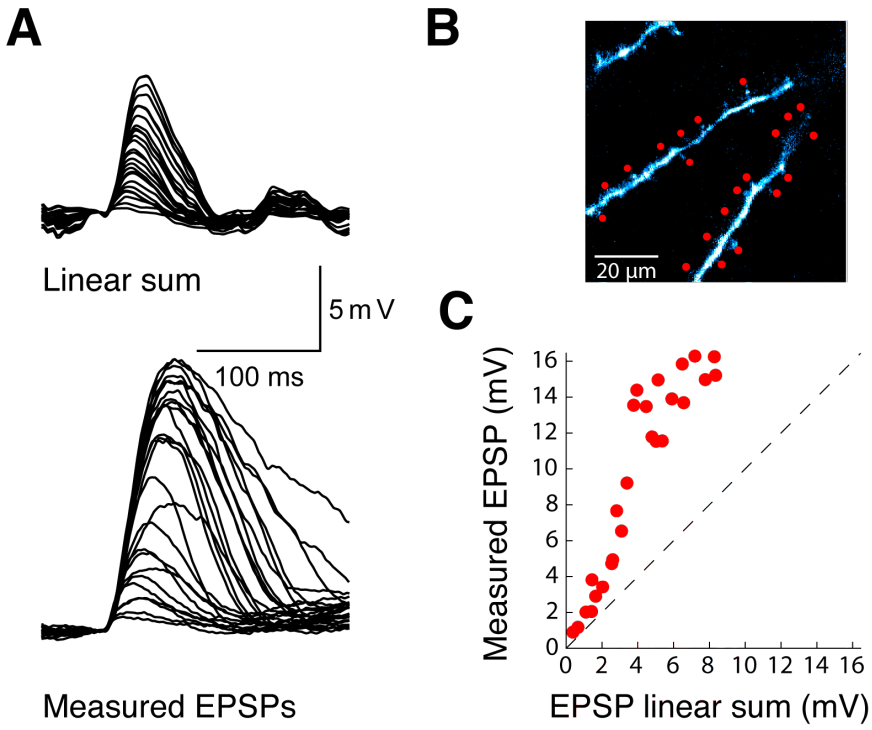

Figure 5.6 Uncaging on 2 dendrites results in substantially increased supralinearity of dendritic integration

A. Linear sum and recorded EPSPs activating multiple synapses on both dendrites in an interleaved manner. **B**. Image of 2 dendritic branches. Uncaging spots are indicated by filled red filled circles. **C.** Input-output function of dendritic integration of inputs to both dendrites.

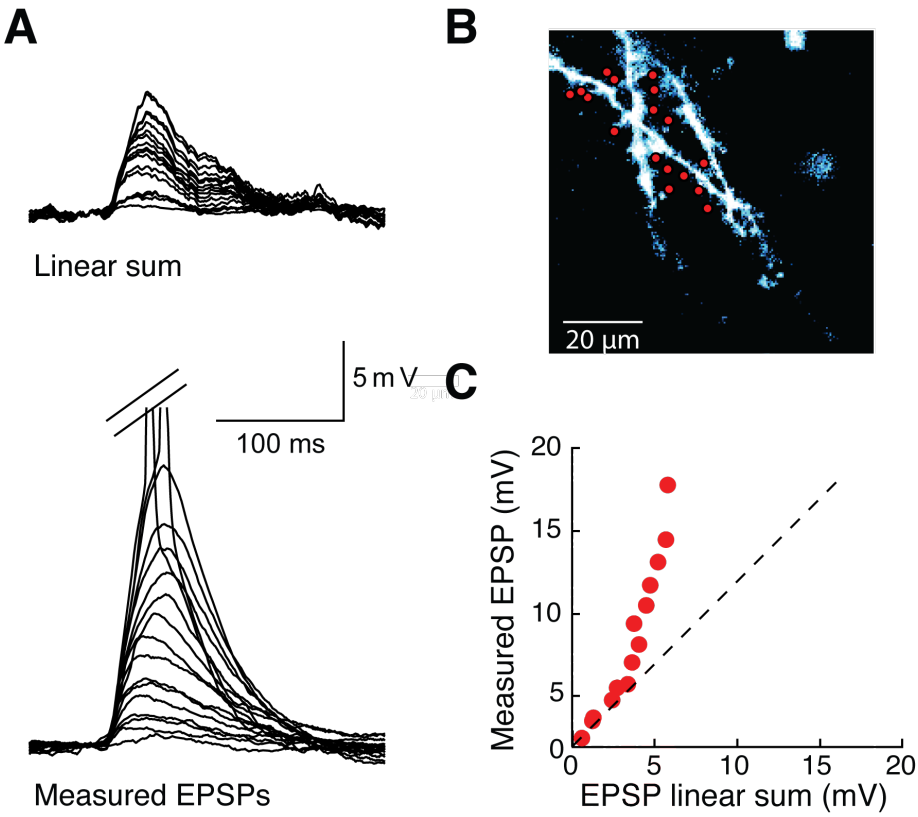

Figure 5.7 Action potentials could be evoked by uncaging on two dendrites

A. Image of 2 dendritic branches. Uncaging spots are indicated by filled red circles. **B.** Linear sum and recorded EPSPs evoked by activating multiple synapses on both dendrites in an interleaved manner. **C.** Input-output function of dendritic integration of this recording.

In order to further compare dendritic integration of inputs arriving at two dendrites as opposed to single dendrites, I assessed input-output functions of interleaved stimulations of synapses of both dendrites (Fig. 5.8A) and input-output functions of stimulations of each of these dendrites individually (Fig. 5.8B).

This turned out to be a challenging experiment since uncaging had to be performed multiple times on each spine, which could result in photo damage. To avoid this, I reduced the laser power, which resulted in smaller EPSPs, thus, more synapses needed to be activated in order to

reach large EPSPs, which was rarely possible in a single focal plane due to the radial morphology of the dendritic tree.

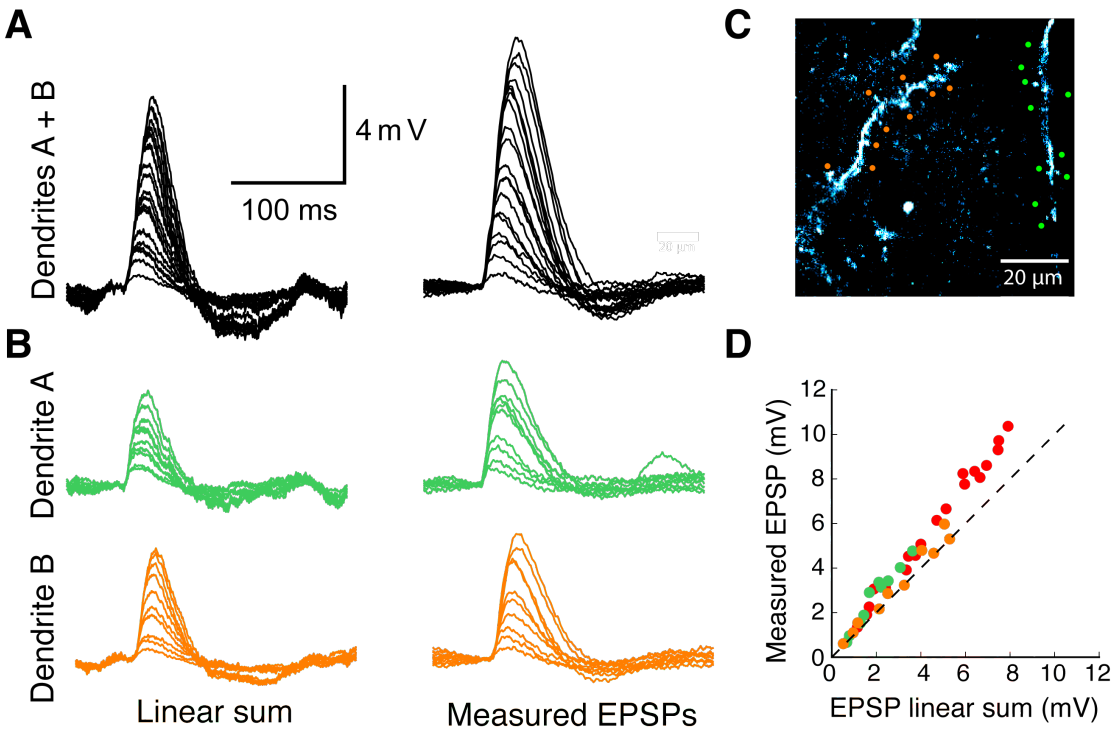

Figure 5.8 Comparison of dendritic integration during stimulation of single or multiple dendritic branches

A. Linear sum and recorded EPSPs, acquired somatically while uncaging on synapses on both dendrites in an interleaved manner. **B**. Linear sum and recorded EPSPs, acquired somatically while uncaging on synapses on dendrite A (green) or on dendrite B (orange). **C**. Image of 2 dendritic branches. Uncaging spots are indicated by filled circles. **D.** Input-output function of dendritic integration of the recordings in A and B, where red circles represent recordings acquired uncaging on both dendrites and orange and green circles represent recordings uncaging on either of these dendrites individually.

With smaller laser power inputs to single branches were integrated in a slightly supralinear manner (Fig. 5.8D orange and green dots). Uncaging on both dendrites simultaneously evoked larger cumulative EPSP amplitudes since more synapses were activated (Fig. 5.8D red dots). Uncaging on both dendrites simultaneously resulted in a degree of supralinearity that was comparable to the supralinearity that I expected from the sum of the responses to stimulations of the individual dendrites, i.e. there was no noticeable cooperative effect between the dendritic branches (Fig. 5.9). This held true for 10 other recordings (Fig. 5.10), majority of which were sister dendrites of the same branch. However, it is important to mention, that many recordings were discarded due to the slice drift or photo damage artefacts which were common during this experiment due to the duration of it and that each synapse has been activated multiple times. Thus, I cannot claim for certain that cooperativity between the dendrites of stellate cells does not exist, however, it was not detected in the present experiments.

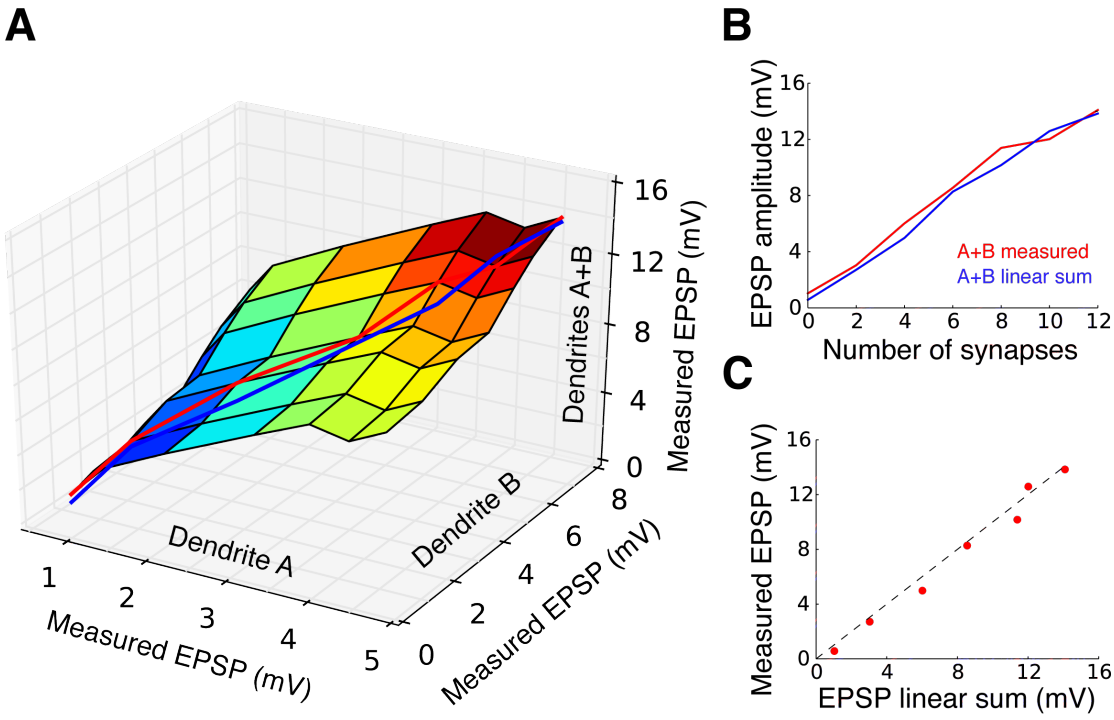

Figure 5.9 Near-simultaneous stimulation of inputs on two dendrites

A. Surface profile of measured EPSPs uncaging on dendrite A (x axis), dendrite B (y axis) and linear sum of both dendrites together (z axis). **B**. Comparison of linear sum and recorded amplitude of EPSPs evoked by increasing number of synapses. **C**. Input-output function of stimulating 2 dendrites.

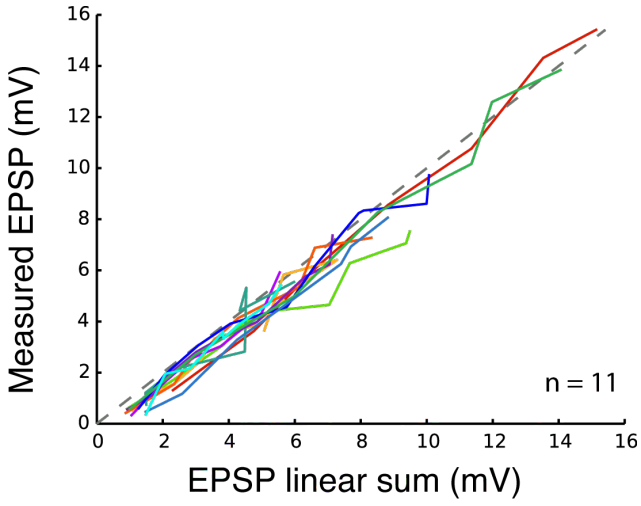

Figure 5.10 Dendritic integration of inputs on two dendrites

11 recordings of uncaging on interleaved inputs on 2 dendrites show nearly linear integration.

5.3 Discussion

Here I have described the dendritic integration of multiple inputs on a single dendritic branch during *in vivo*-like membrane potential dynamics. I have shown that dendritic inputs are integrated in a supralinear fashion, similar to what we observed in the data presented in Chapter 3; however, the EPSPs here are broader (integral nonlinearity is significantly higher), meaning that they can potentially provide a significantly longer time window for effective input integration. Moreover, slow but not fast dendritic spikes were considerably more frequent when uncaging during *in vivo*-like membrane potential dynamics than when uncaging at resting membrane potential.

Finally, during *in vivo*-like membrane potential dynamics, somatic action potentials could be evoked by uncaging on as few as 13 spines of single dendritic branches. This brings us to a better understanding of how simultaneous inputs to single dendritic branches might be integrated *in vivo*. However, presumably *in vivo* depolarization occurs due to the inputs to the dendrites, not the soma, thus, reaching much higher membrane potential values locally in the dendrites, than what is possible to be achieved during somatic current injection. Moreover, *in vivo* depolarization is caused by synaptic conductances, not current injection, what would cause a big shunt *in vivo*, which we are not accounting for in slices. Furthermore, we do not know yet the spatiotemporal pattern of inputs arriving at the dendrites of the stellate cells. Therefore, we cannot tell for certain that this level of supralinearity and dendritic spikes is comparable to what is happening *in vivo* during behavior.

I also wanted to assess how simultaneous inputs are integrated on multiple dendritic branches. Using two-photon MNI-glutamate uncaging on multiple interleaved synapses of 2 nearby dendritic branches in some cases resulted in triggering of somatic action potentials; however, no cooperativity effect between 2 dendrites was found using this technique. Of course, we do not know what are spatiotemporal characteristics of the inputs to the stellate cells *in vivo*. It is likely this could be assessed using different tools, such as photo stimulation of channelrhodopsins in cells projecting onto the dendritic tree of stellate cells, although this technique would not give us the same specificity as the single-spine resolution obtained by two-photon MNI-glutamate uncaging. However, this could at the very least help us obtain a better understanding of the spatial distribution of the inputs arriving at the stellate cells.

6. DENDRITIC INTEGRATION IN MEC II PYRAMIDAL CELLS

6.1 Introduction

As described in the introduction of this thesis, dendritic integration varies between cell types, as it depends on many factors, including cell morphology and distribution of active conductances. The grid cell phenotype is not restricted to a single cell type, as neurons throughout all layers of MEC display grid cell firing (Boccara et al., 2010; Sargolini, 2006). In layer 2 of MEC, there is strong evidence for stellate cells representing a large fraction of the grid cell population, since they make up the majority of MEC II principal cell population (Gatome et al., 2010) and have been found to show grid-like firing (Burgalossi et al., 2011; Domnisoru et al., 2013; Schmidt-Hieber & Hausser, 2013; Zhang et al., 2013). Recently there has been indirect evidence that MEC II pyramidal neurons may also contribute to the grid cell population (Ray et al., 2014; Tang et al., 2014). These cells form anatomical clusters and are calbindin antibody positive (CB+) in immunohistochemical stainings (Ray et al., 2014; Kitamura et al., 2014). Another recent study, using spike locking to theta oscillations in the extracellular recordings to identify stellate cells from pyramidal cells in freely moving animals shows that both cell types exhibit weak hexagonal activity in the environment, but that stronger hexagonal discharges were mainly found in pyramidal cells (19/99 pyramidal cells vs. 3/94 stellate cells) and stellate cells were mainly border cells (10/94 stellate cells vs. 3/99 pyramidal cells) (Tang et al., 2014).

However, at this stage we cannot fully determine what fractions of the MEC II grid cell population are composed of pyramidal or stellate cells. Thus, here I will present pilot data on dendritic integration in MEC II pyramidal cells.

6.2 Results

This set of experiments has been conducted in the same manner as dendritic integration experiments in MEC II stellate cells presented in chapter 3, stimulating synapses with an uncaging interval of ≤ 1ms. MEC II pyramidal cells and stellate cells differ in dendritic tree morphology (Fig. 6.1A) and electrophysiological profiles (Fig. 6.1B) compared to stellate cells (Fig. 2.1). However, MEC II contains intermediate types between, e.g. cells with pyramidal-like cell morphology (one pronounced apical-like dendrite) and stellate cell electrophysiology (abundant in I_h) or continuum in between putative stellates and putative pyramidal cells in morphologies, specially in the deeper part of MEC II (Alonso & Klink, 1993; Klink & Alonso, 1997, Gatome et al, 2010; Canto et al., 2011). Therefore I have targeted putative pyramidal cells which were located in the deeper side of layer II of MEC, within the calbindin positive cell patches (Fig. 6.1C), as has also been reported in a recent study (Ray et al., 2014). Biocytin-filled cells were weakly immunopositive for calbindin (Fig. 6.1D), which may be explained by a fast washout of cytoplasm-soluble endogenous calbindin during whole-cell recordings lasting 30-60 minutes, as has been described previously (A. Müller et al., 2005).

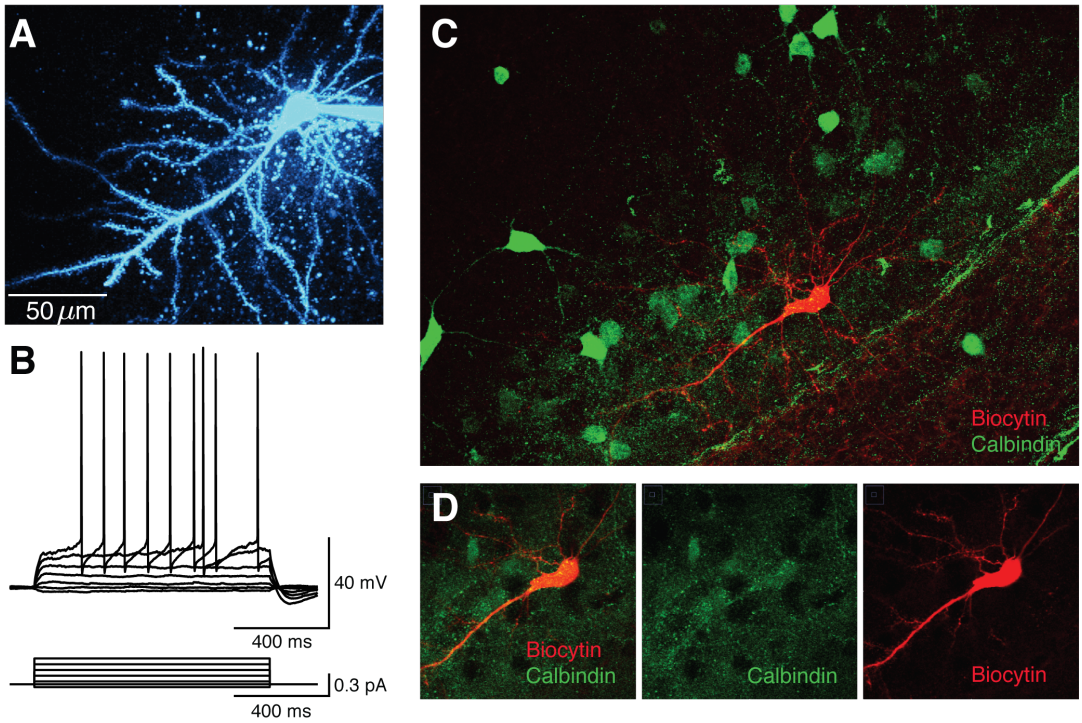

Figure 6.1 MEC II pyramidal cells were located within calbindin positive cell patches

A. Alexa 594 filled pyramidal cell during whole-cell recording. **B**. Electrophysiological response to steady state current injections. C. Immunohistochemical staining against calbindin (green). A pyramidal cell (same as in A) was filled with biocytin during the recording (counter-stained with Streptavidin-Alexa594, red). D. Pyramidal cells showed weak calbindin signal after whole-cell recordings, potentially due to calbindin washout during recording.

Pyramidal cells have apical and basal dendrites, and they could potentially be governed by different rules for dendritic integration, as for example has been reported in pyramidal cells of CA3 (Makara & Magee, 2013). Therefore I limited my experiments to single branches of apical dendrites of pyramidal cells (Fig. 6.2A). Uncaging near-simultaneously on multiple spines resulted in larger EPSPs than expected from the linear sum of individual EPSPs evoked by activation of single spines (Fig. 6.2B). As can be seen in the input-output function of the cell (Fig. 6.2C), the first 5 EPSPs were summated in an approximately linear

fashion, and supralinearity increased as the number of synapses increased.

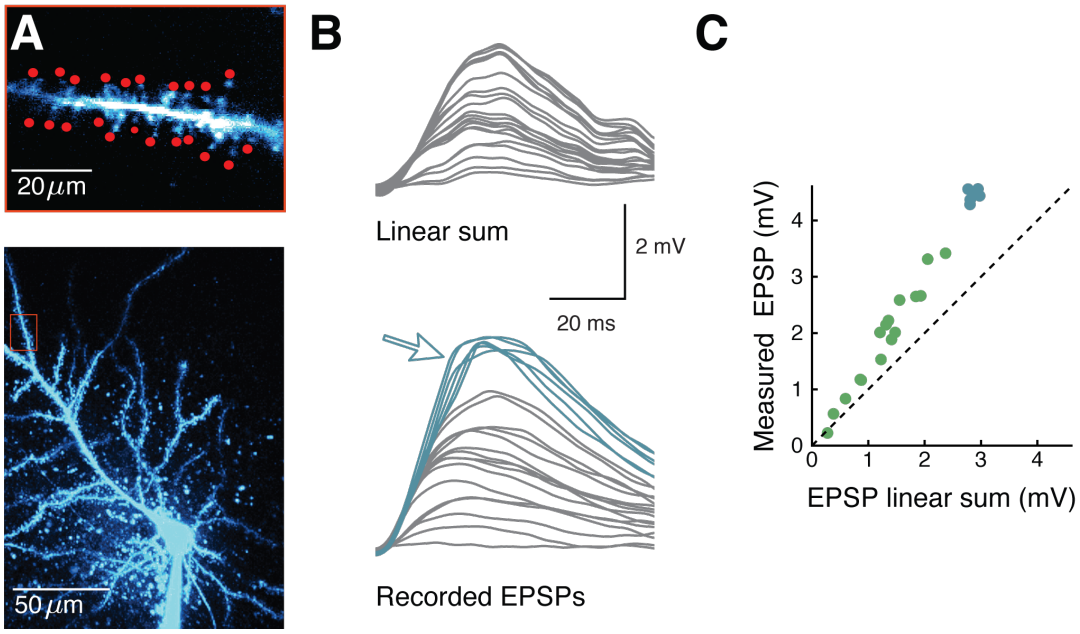

Figure 6.2 MEC II pyramidal cells summate near-synchronous inputs in a supralinear manner

A. Pyramidal cell filled with Alexa 594 during a whole-cell recording (bottom). Inset (top) shows dendritic uncaging spots at higher magnification. **B.** Linear sum of individual EPSPs (top) and recorded EPSPs evoked by uncaging on multiple spines of a single pyramidal cell dendrite. Blue traces represent recordings with slow dendritic spikes. **C.** Input-output function of the recording in (B) shows that this MEC II pyramidal cell integrates near-synchronous inputs in a supralinear manner.

At the population level stellate cells (Fig. 6.3A) and pyramidal cells (Fig. 6.3B) integrated inputs in a similar manner, showing similar amounts of supralinearity (Fig.6.3C) (Mann-Whitney *U* test: $P = 0.18$, $U = 122$).

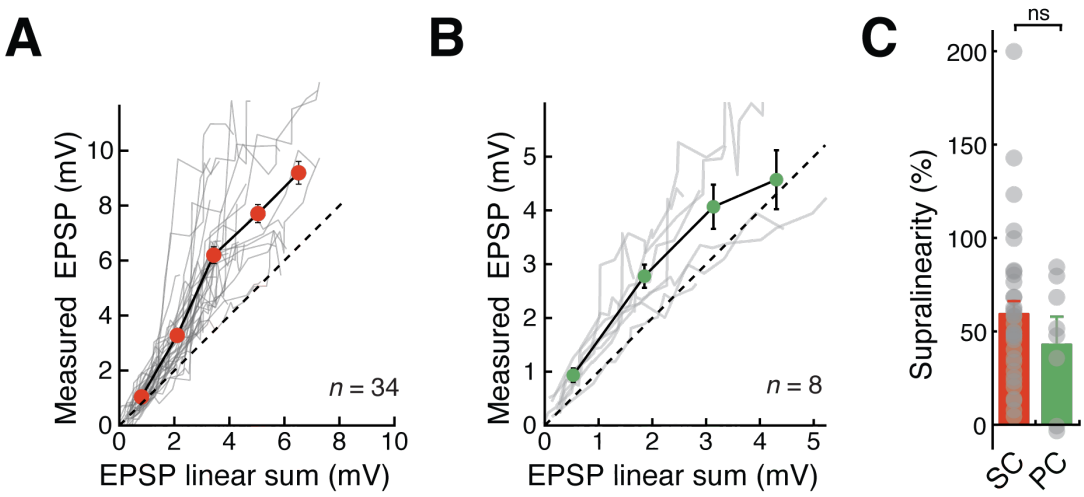

Figure 6.3 MEC II pyramidal cells and stellate cells both exhibit supralinear summation

A. Summary of 34 recordings from stellate cells, uncaging on multiple synapses of single dendritic branches with uncaging interval ≤ 1ms. **B.** Summary of 8 recordings from pyramidal cells, uncaging on multiple synapses of single dendritic branches with uncaging interval ≤ 1ms. **C.** MEC II stellate cells (SC) and pyramidal cells (PC) show a comparable level of supralinearity (Mann-Whitney *U* test: $P = 0.18$, $U = 122$).

Moreover, fast and slow dendritic spikes could be evoked by uncaging on the apical dendrites of pyramidal cells (Fig.6.4A traces in orange represent EPSPs with fast spike and Fig. 6.2B traces in blue represent EPSPs with slow spike). Fast spikes boosted supralinearity (Fig. 6.4C) and could be identified by a shift of the peak in the d^2V/dt^2 trace (Fig. 6.4B). Comparable amounts of fast and slow dendritic spikes could be evoked in stellate and pyramidal cells (Fig. 6.4D) (fast spikes – SC: 26%, PC: 33%, $P = 0.692$ (Fisher's exact test); slow spikes – SC: 26%, PC: 22%, $P = 0.413$ (Fisher's exact test)).

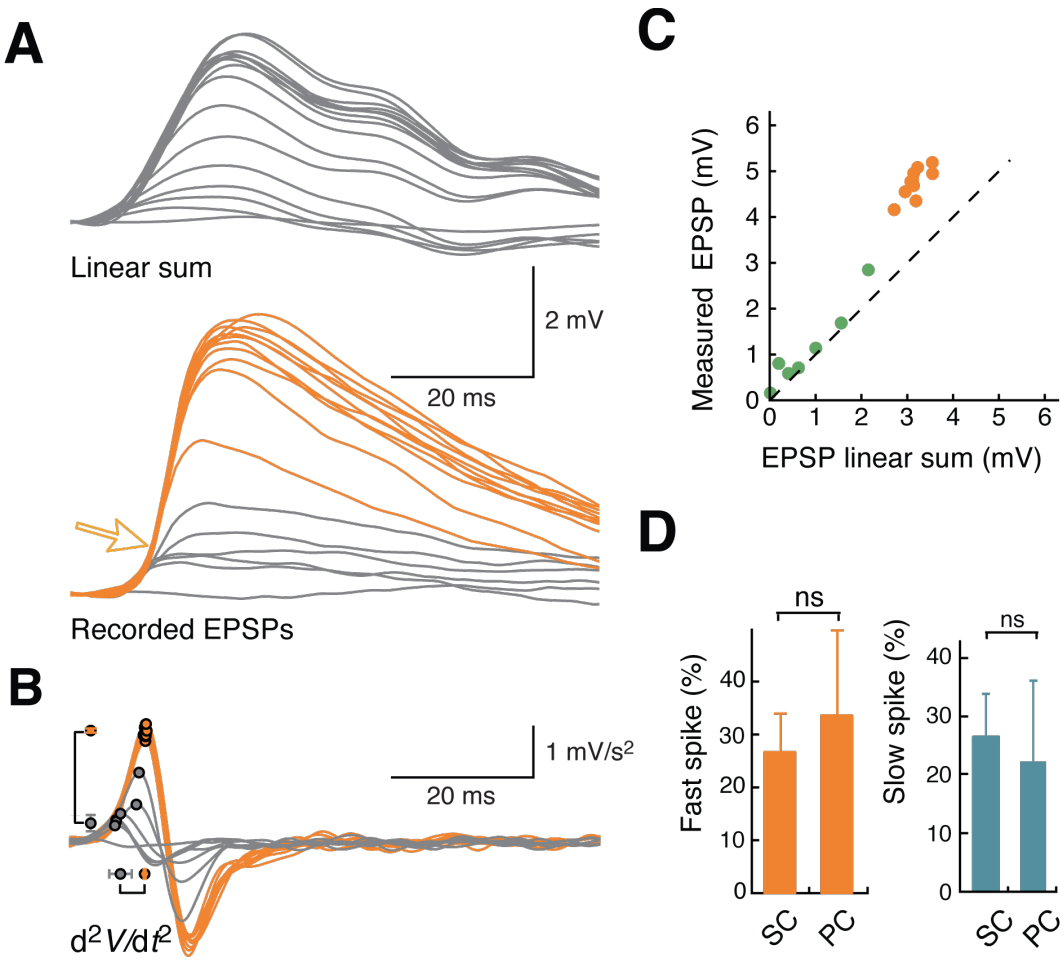

Figure 6.4 Fast and slow dendritic spikes can be evoked in MEC II pyramidal cells by near-synchronous stimulation

A. Linear sum of EPSPs (top) and recorded EPSPs (bottom) evoked by uncaging on a single dendrite of a pyramidal cell. Orange traces represent recordings with fast dendritic spikes. **B.** Fast spikes were detected by a shift of the peak in the d^2V/dt^2 trace. **C.** Input-output function of the recording in (A), where traces with a fast dendritic spike (orange) show strong supralinearity. **D.** MEC II stellate and pyramidal cells show a comparable proportion of fast (SC: 26%, PC: 33%, $P = 0.692$ (Fisher's exact test)) and slow (SC: 26%, PC: 22%, $P = 0.413$ (Fisher's exact test)) dendritic spikes.

6.3 Discussion

In this chapter I have described that apical dendrites of MEC II pyramidal cells integrate inputs in a supralinear manner, and both fast and slow dendritic spikes can be detected. Despite the fact that no obvious differences were observed for supralinear dendritic summation between pyramidal and stellate cells, more work needs to be done to fully assess potential differences in measures that have not been tested (e.g., temporal window of supralinear integration, active conductances mediating supralinearity and dendritic spikes).

In addition, there might be different integration modes in distal versus proximal dendrites in pyramidal cells, as has been reported in neocortex layer II/III pyramidal cells (Branco & Häusser, 2011) but has not yet been found to be the case for MEC II stellate cells (Chapter 3). Moreover, inputs arriving to the apical and basal dendrites might be integrated differently (Makara & Magee, 2013). Also we do not know yet if pyramidal cells in the MEC II integrate inputs differently from the other areas of the brain. Thus, more work is needed to obtain a complete understanding of dendritic integration in MEC II pyramidal cells.

7. GENERAL DISCUSSION AND FUTURE DIRECTIONS

In this thesis, I have presented novel research on dendritic integration in stellate cells and pyramidal cells of medial entorhinal cortex layer II (MEC II). This has been achieved using patterned two-photon uncaging of MNI-glutamate on multiple synapses. I will l discuss the advantages and limitations of this method in Chapter 7.1. Then, I will overview the modes of dendritic integration MEC II principal neurons are capable off and what conductances mediate them and the factors that influence integration mode in Chapter 7.2. Additionally, I have also assessed dendritic integration in MEC II stellate cells during *in vivo*-like membrane potential dynamics, which I will discuss in Chapter 7.3. What do these findings suggest about mechanisms mediating grid cell activity will be discussed in Chapter 7.4. And some future directions will be outlined in Chapter 7.5.

7.1 Two-photon uncaging of MNI-glutamate Dendritic integration in MEC II principal neurons

To study dendritic integration in MEC II principal neurons I used patterned two-photon MNI-glutamate uncaging of multiple and whole-cell patch clamp recordings. MNI-glutamate does not activate glutamate receptors till it absorbs high-energy photons of the laser. Two-photon stimulation has a few advantages over one-photon stimulation. Firstly, it uses long wavelength (730 nm) radiation, which does not cause thermal and photo damage across the tissue as compared to one-photon stimulation, which has to be used as much shorter wavelength to have

the same amount of energy (around 400 nm). Secondly, two-photon laser has much smaller point spread function, thus, allows a very localized photolysis. Two-photon laser stimulations combined with MNI-glutamate, which is not active on glutamate receptors prior to photolysis and has a fast photolysis kinetics once photon energy is absorbed, enables us to activate synapses at single spine resolution so creating a great tool to study a wide range of questions to in terms of dendritic integration.

This method has a few limitations. Firstly, even though MNI-glutamate is not active on the glutamate receptors, it does inactivate synaptic transmission of $GABA_A$ receptors, thus, is not suitable to be used if contribution of inhibitory synapses is to be studied. In these experiments I have applied MNI-glutamate locally via large opening pipette to prevent slices from going epileptic due to global $GABA_A$ receptors inactivation and indeed local spread of MNI-glutamate did not cause epileptic activity in the neurons of interest. Another limitation is that local application of MNI-glutamate does not allow it to penetrate well deep in the tissue, making it difficult to evoke large EPSPs in the dendrites, which were deeper in the tissue, thus, limiting us to the dendrites close to the surface of the slice. Another problem occurred during experiments if we were using the same slice for longer periods of time (30-75 mins, depending on the quality and freshness of slice) cells at the bottom of the recording chamber were dying due to poor supply of ACSF and slices started to swell causing physical drift during uncaging, often resulting in photodamage of the dendrite, after which experiment on that cell had to be terminated and recording dismissed. This has improved using only very fresh slices of younger animals (P26) and using high rates of perfusion (70-75 drips/min). After learning to play around the limitations, this method was a great tool to assess if principal neurons of the MEC II are capable of supralinear summation of synaptic inputs and, if so, what active conductances mediate it.

7.2 Dendritic integration in MEC II principal neurons

In this thesis I present for the first time the rules governing dendritic integration in MEC II stellate and pyramidal cells. I found that both pyramidal cells and stellate cells were found to be able to integrate near-synchronous clustered inputs to single dendritic branches in a supralinear manner, with summation boosted by sodium channels and NMDA receptors. Supralinearity was reduced via increasing time interval between synapse activation and was near to linear at the intervals of 8 ms. Supralinearity was also reduced by blocking VGSCs with TTX and completely abolished in the presence of the NMDAR antagonist APV. This suggests that a combination of both conductances is needed to mediate supralinear dendritic integration. Since APV alone was able to reduce supralinearity to near-linear level, an initial depolarization via NMDARs might be needed for reaching the VGSC activation threshold in the dendrite, what has as also been reported before in layer II/II pyramidal cells in neocortex (Branco & Häusser, 2011). Similarly, previous studies using direct recordings from the dendrites of stellate cells (Magistretti, et al., 1999a; 1999b) revealed the existence of VGSCs, which may potentially mediate this fast spike.

In about a quarter of all whole-cell somatic recordings, when activating synapses at a high spatial and temporal clustering, fast and slow dendritic regenerative events have been detected. Since dendritic patch clamp recordings or calcium imaging at dendrites have not been simultaneously performed it is hard to claim for certain that these events were dendritic spikes, however, they resembled sodium and NMDA spikes reported in other studies (Losonszy & Magee 2006), moreover, they were not present in the recordings under TTX and APV.

Another conductance abundantly expressed in the stellate cells of MEC

II is hyperpolarization-activated current (I_h) (Alonso & Klink, 1993), which can be pharmacologically blocked by ZD7288 (Gasparini & DiFrancesco, 1997; Harris & Constanti, 1995). This current is important for shaping resting and resonant properties of stellate cells (Nolan et al., 2007), therefore might contribute to dendritic integration of inputs, arriving to the cell over the longer period of time. Due slow kinetics of this current, it was not likely to play an active role in the integration of 15-30 nearly-coincident inputs. For this reason and time limitations on the project I did not study contribution of this current for dendritic integration. However, blocking I_h was found to depolarize membrane potential and subsequently reduce amplitude of EPSPs, what was rescued by depolarisation of the cell by somatic current injection in layer 5 pyramidal neurons (Branco & Hausser, 2011) and my pilot experiments (not presented in this thesis) provided comparable results.

Another factor which I suspected to influence dendritic integration mode was distance from the soma, what has been found in the pyramidal cells of MEC layer 5 (Gasparini, 2011), however, my experiments did not notice such a big difference between distal and proximal dendrites. Synapses were stimulated 50-250 μm away from the soma, and it is likely that some of the dendritic spikes were strongly attenuated while propagating to the soma, as observed in layer V pyramidal neurons (Nevian et al., 2007). Similarly, somatically recorded EPSP amplitudes were likely strongly attenuated compared to their local dendritic amplitudes at the synaptic site (Nevian et al. 2007). Some recordings (9/34) showed pronounced saturation where increasing the number of synapses did not serve to further increase EPSP amplitude, and the majority of these saturating recordings (7/9) were obtained when activating distal parts (> 120 μm) of dendrites, where input impedance is highest, and therefore local membrane potential at the synaptic site will reach AMPA and NMDA receptor reversal potential at the synapse more readily.

Temporal summation window did not depended on the uncaging location along the dendrite in stellate cells, while rate of rise was higher in proximal as compared to distal dendrites. Amplitude was not significantly different between proximal and distal, but different between middle and distal dendrites. Location independence of EPSP temporal summation has been previously reported in the apical dendrites of CA1 (Magee & Cook, 2000). This phenomenon might be achieved via higher densities of synaptic conductances and higher input impedance in the distal dendrites (Nicholson et al., 2006) in order to normalize their somatic impact, a phenomenon that has been called 'synaptic scaling' (Magee, 2000; Williams & Stuart, 2003).

Stimulating the apical dendrites of pyramidal cells led to a comparable amount of supralinearity and dendritic spikes to stellate cells; however, we cannot yet assert that rules governing dendritic integration in pyramidal cells and stellate cells are the same. The main focus of this thesis was on dendritic integration in stellate cells and more thorough studies would be needed to get a better understanding of dendritic integration in pyramidal cells. Future points of interest would include assessing the influence of the spatial and temporal distribution of inputs, comparing the integration of inputs in basal and apical dendrites, and pharmacologically testing the active conductances mediating supralinear summation in pyramidal cells of MEC II.

Supralinear dendritic integration in MEC II principal neurons is comparable to previous findings in pyramidal cells in neocortical layers II/III (Branco et al., 2010; Branco & Häusser, 2011), V (Larkum et al., 2009; Nevian et al., 2007), hippocampal CA1 (Losonczy & Magee, 2006) and CA3 (Makara & Magee, 2013). Interestingly, there was a substantial amount of variability in the supralinearity of dendritic integration in different cells. Due to the limitations imposed by the

radial dendritic morphology of stellate cells, the limited depth of effective uncaging and occasional photodamage or slice drift that occurred during the recording, I usually activated only 1 dendrite per cell. This made it difficult to rule out whether this variability was caused by the limitations of methodology, differences between cells (cell heterogeneity), or different dendrites integrating inputs in distinct manners as a result of their intrinsic heterogeneity of active conductances.

Moreover, even though inputs were integrated in a supralinear manner, the stimulation of a single dendrite using this method was not sufficient to evoke action potential output. This can either be explained by a limited number of synapses that can be stimulated in a single focal plane because of the radial morphology of the dendritic tree of stellate cells, or alternatively multiple dendrites need to be activated to drive cells to fire. The latter mechanism might provide robustness against noise, which could explain why grid cells have very low firing activity outside of grid fields (Fyhn et al. , 2008; Hafting et al., 2005).

Even though here I have shown that supralinear summation is possible in the MEC II dendrites, when nearly-synchronous synaptic inputs are highly clustered on the same dendritic branches, however, it is not clear if that activation is common *in vivo*. Also, it is not known yet how inputs to the principal neurons of MEC II are distributed across the dendritic tree. More physiologically relevant stimulation can be achieved stimulating cells which project to stellate or pyramidal cells at the MEC II either by electrical or optogenetic stimulation together with calcium imaging in dendritic branches or dendritic patch clamp recordings to estimate postsynaptic currents. This might be rather tricky since stellate cells have very long and thin dendrites, making it merely impossible to patch. Also, I have done some calcium imaging in distal dendritic branches of the MEC II stellate cells during uncaging at the

beginning of my project and could not detect any calcium transients, suggesting that either locally evoked EPSPs were too small to activate voltage-gated calcium channels or that calcium is not the main conductance in the distal dendrites of the stellate cells. Moreover, activation of input cells to the MEC II principal neurons would not provide such a great control over the number of synapses activated and would not allow to address the questions I analysed in this thesis. Also, how many neurons are projecting to the principal neurons of MEC II at the same time and at what sequence and frequency are they activated *in vivo* is also unknown, raising again limitations to reproducing functionally relevant stimuli.

7.3 Dendritic integration under in vivo like membrane potential dynamics

In an attempt to make our *in vitro* conditions more biologically realistic, we combined two-photon glutamate uncaging on single synapses *in vitro* with *in vivo*-like membrane potential dynamics mimicking membrane potential ramps observed during firing field crossings in somatic whole-cell patch clamp recordings from MEC II neurons during virtual navigation. In these *in vivo* experiments, both a depolarizing ramp as well as a firing rate increase were observed as the animal was crossing a firing field (Schmidt-Hieber & Hausser, 2013).

Interestingly, *in vivo*-like membrane potential dynamics significantly increased the supralinearity of the integrals of EPSPs; this increase in supralinearity could potentially result in a longer integration time window for synaptic inputs at the peak of a depolarizing *in vivo*-like ramp. Moreover, the proportion of fast and slow dendritic spikes were also significantly increased and stimulation of the same amount of synapses (10-17) to previous experiments resulted in somatic action

potential output. This suggests that synchronous inputs to single dendrites might be more effective *in vivo* if they arrive at the right time during the depolarizing ramp, which is most likely created by excitatory and inhibitory inputs arriving on the dendrites and the perisomatic region (Schmidt-Hieber & Hausser, 2013).

Reproducing this *in vivo*-like membrane potential dynamics *in vitro* is certainly not an easy task since this dynamics most likely originate from an interplay between inhibition and excitation arriving to different dendrites and perisomatic region. Unfortunately this was not feasible to created *in vitro* since currently we do not know what synaptic activation spatiotemporal patterns and synaptic weights have created this profile, therefore, I create it with custom waveform current injection at the soma. Of course, interpreting the results from these experiments, it is important to keep in mind that dendritic current profiles and dendritic membrane potential gradients will probably be different *in vivo* since currents do not propagate well from the soma to the dendrites, especially if we examine distal dendrites.

7.4 Dendritic integration and grid cell activity

It has been a lasting debate if grid cell firing emerges from network activity or intrinsic properties of the cell.

There has been some evidence from previous studies that intrinsic properties of the cell are important in formation of spatially modulated firing fields of place cells. Firstly dendritic spikes have been found in place cells of hippocampus during two-photon calcium imaging of dendritic branches while head restrained mice were navigating in virtual environment (Sheffield and Dombeck, 2014). Prevalence of dendritic spikes throughout dendritic arbour was not only highly variable depending on animal's location in virtual environment but also

was a good indicator of spatial precision and persistence or disappearance of place fields (Sheffield and Dombeck, 2014). Another study has shown that a small and spatially uniform depolarization of spatially untuned somatic membrane potential of silent cells lead to a sudden and reversible emergence of a spatially tuned subthreshold response and firing fields, suggesting the importance of postsynaptic cell excitability in formation of place fields (Lee et al., 2012).

Dendritic spikes might be well suited to explain grid cell activity. Firstly, fast onset Na^+ regenerative event, which have been recorded in principal neurons of MEC II, might increase the precision of grid cell phase precession, increasing the robustness of the temporal code of grid cells. Secondly, long lasting NMDA spikes might function as coincidence detectors since both depolarization of cell membrane and abundant release of glutamate in multiple co-localized synapses are needed to evoke NMDA spikes, what might mediate the precision and robustness of grid cell firing. More experimental and theoretical work is needed to test these hypothesis.

7.5 Future directions

Functional advantages and limitations of the method and some alternative techniques are described in detail Chapter 7.1. Here I will focus on my dream experiment for the future. Incredible advancement of techniques in the recent years enables us to study cell activity of awake, behaving animals. Activity of grid cells and place cells has recently been recorded using whole-cell patch clamp (Domnisoru et al., 2013; Schmidt-Hieber and Hausser, 2013) or calcium imaging (Dombeck et al, 2010; Dombeck and Tank 2014) techniques while head-restrained mice were navigating in the virtual environment projected on the spherical screen covering mouse vision field via movements on the spherical treadmill. MEC is a difficult area to perform calcium imaging since it's positioning

in the brain, what has just been overcome by a chronic implantation of microprism at the caudal part MEC together with genetically encoded calcium indicator, that allowed to observe activity of population of grid cells while animal was navigating in virtual environment. Another study from the same research group tracked calcium transients in the soma, axon and different branches of dendritic tree of place cells using electric lens, which could rapidly switch the focal planes while head-restrained animal was also exploring virtual environment (Sheffield and Dombeck, 2015). They discovered that not only regenerative dendritic events do exist in place cells, but also they are good predictors of the spatial persistence and the persistence or disappearance of place fields, suggesting that spiking in the dendritic tree is important for the formation of hippocampal representation of space (Sheffield and Dombeck, 2015). Thus, next step is to combine the advancements of both studies to monitor dendritic activation patterns of the grid cells. This experiment would allow us to better understand cellular mechanisms mediating grid cell activity.

REFERENCES

Alonso, A., & Klink, R. (1993). Differential electroresponsiveness of stellate andpyramidal-like cells of medial entorhinal cortex layerII. *J Neurophysiology*, 1–17.

Alonso, A., & Llinás, R. R. (1989). Subthreshold Na+-dependent theta-like rhythmicity in stellate cells of entorhinal cortex layer II. *Nature*, *342*(6246), 175–177. doi:10.1038/342175a0

Alonso, A., de Curtis, M., & Llinás, R. (1990). Postsynaptic Hebbian and non-Hebbian long-term potentiation of synaptic efficacy in the entorhinal cortex in slices and in the isolated adult guinea pig brain. *Proceedings of the National Academy of Sciences of the United States of America*, *87*(23), 9280–9284.

Amitai, Y., Friedman, A., Connors, B. W., & Gutnick, M. J. (1993). Regenerative activity in apical dendrites of pyramidal cells in neocortex. *Cerebral Cortex (New York, N.Y. : 1991)*, *3*(1), 26–38.

Angelo, K., London, M., Christensen, S. R., & Häusser, M. (2007). Local and global effects of I(h) distribution in dendrites of mammalian neurons. *The Journal of Neuroscience*, *27*(32), 8643–8653.

Antic, S. D., Zhou, W.-L., Moore, A. R., Short, S. M., & Ikonomu, K. D. (2010). The decade of the dendritic NMDA spike. *Journal of Neuroscience Research*, *88*(14), 2991–3001.

Barry, C., Ginzberg, L. L., O'Keefe, J., & Burgess, N. (2012). Grid cell firing patterns signal environmental novelty by expansion. *Proceedings of the National Academy of Sciences*, *109*(43), 17687–17692.

Barry, C., Hayman, R., Burgess, N., & Jeffery, K. J. (2007). Experience-dependent rescaling of entorhinal grids. *Nature Neuroscience*, *10*(6), 682–684.

Bekkers, J. M. (2000). Distribution and activation of voltage-gated potassium channels in cell-attached and outside-out patches from large layer 5 cortical pyramidal neurons of the rat. *The Journal of Physiology*, *525 Pt 3*, 611–620.

Boccara, C. N., Sargolini, F., Thoresen, V. H., Solstad, T., Witter, M. P., Moser, E. I., & Moser, M.-B. (2010). Grid cells in pre- and parasubiculum. *Nature Neuroscience*, *13*(8), 987–994.

Bonnevie, T., Dunn, B., Fyhn, M., Hafting, T., Derdikman, D., Kubie, J., et al. (2013). Grid cells require excitatory drive from the hippocampus. *Nature Neuroscience*.

Branco, T., & Häusser, M. (2011). Synaptic integration gradients in single cortical pyramidal cell dendrites. *Neuron*, *69*(5), 885–892.

Branco, T., Clark, B. A., & Häusser, M. (2010). Dendritic discrimination of temporal input sequences in cortical neurons. *Science*, *329*(5999), 1671–1675.

Brandon, M. P., Bogaard, A. R., Libby, C. P., Connerney, M. A., Gupta, K., & Hasselmo, M. E. (2011). Reduction of theta rhythm dissociates grid cell spatial periodicity from directional tuning. *Science*, *332*(6029), 595–599.

Bruehl, C., & Wadman, W. J. (1999). Calcium currents in acutely isolated stellate and pyramidal neurons of rat entorhinal cortex. *Brain Research*, *816*(2), 554–562.

Buetfering, C., Allen, K., & Monyer, H. (2014). Parvalbumin interneurons provide grid cell-driven recurrent inhibition in the medial entorhinal cortex. *Nature Neuroscience*, *17*(5), 710–718.

Burak, Y., & Fiete, I. R. (2009). Accurate path integration in continuous attractor network models of grid cells. *PLoS Computational Biology*, *5*(2), e1000291.

Burgalossi, A., Herfst, L., Heimendahl, von, M., Förste, H., Haskic, K., Schmidt, M., & Brecht, M. (2011). Microcircuits of Functionally Identified Neurons in the Rat Medial Entorhinal Cortex. *Neuron*, *70*(4), 773–786.

Burgess, N. (2008). Grid cells and theta as oscillatory interference: Theory and predictions. *Hippocampus*, *18*(12), 1157–1174.

Burgess, N., Barry, C., & O'Keefe, J. (2007). An oscillatory interference model of grid cell firing. *Hippocampus*, *17*(9), 801–812.

Carter, A. G., & Sabatini, B. L. (2004). State-dependent calcium signaling in dendritic spines of striatal medium spiny neurons. *Neuron*, *44*(3), 483–493.

Castelli, L., & Magistretti, J. (2006). High-voltage-activated Ca2+ currents show similar patterns of expression in stellate and pyramidal cells from rat entorhinal cortex layer II. *Brain Research*, *1090*(1), 76–88.

Chalifoux, J. R., & Carter, A. G. (2010). GABAB receptors modulate NMDA receptor calcium signals in dendritic spines. *Neuron*, *66*(1), 101–113.

Clark, B. A., Monsivais, P., Branco, T., London, M., & Häusser, M. (2005). The site of action potential initiation in cerebellar Purkinje neurons. *Nature Neuroscience*, *8*(2), 137–139.

Colbert, C. M., & Johnston, D. (1996). Axonal action-potential initiation and Na+ channel densities in the soma and axon initial segment of subicular pyramidal neurons. *Journal of Neuroscience*, *16*(21), 6676–6686.

Conklin, J., & Eliasmith, C. (2005). A controlled attractor network model of path integration in the rat. *Journal of Computational Neuroscience*, *18*(2), 183–203.

Couey, J. J., Witoelar, A., Zhang, S.-J., Zheng, K., Ye, J., Dunn, B., et al. (2013). Recurrent inhibitory circuitry as a mechanism for grid formation. *Nature Neuroscience*, *16*(3), 318–324.

Dhillon, A., & Jones, R. S. (2000). Laminar differences in recurrent excitatory transmission in the rat entorhinal cortex in vitro. *Nsc*, *99*(3), 413–422.

Dickson, C. T., Magistretti, J., Shalinsky, M., Fransen, E., Hasselmo, M. E., & Alonso, A. (2000). Properties and Role of I h in the Pacing of Subthreshold Oscillations in Entorhinal Cortex Layer II Neurons. *Journal of Neurophysiology*, 1–19.

Doeller, C. F., Barry, C., & Burgess, N. (2010). Evidence for grid cells in a human memory network. *Nature*, *463*(7281), 657–661.

Dombeck, D. A., Harvey, C. D., Tian, L., Looger, L. L., & Tank, D. W. (2010). Functional imaging of hippocampal place cells at cellular resolution during virtual navigation. *Nature Neuroscience*, 1–11.

Dombeck, D., & Tank, D. (2014). Two-photon imaging of neural activity in awake mobile mice. *Cold Spring Harbor Protocols*, *2014*(7), 726–736.

Domnisoru, C., Kinkhabwala, A. A., & Tank, D. W. (2013). Membrane potential dynamics of grid cells. *Nature*, *495*(7440), 199–204.

Dudman, J. T., & Nolan, M. F. (2009). Stochastically gating ion channels enable patterned spike firing through activity-dependent modulation of spike probability. *PLoS Computational Biology*, *5*(2), e1000290.

Erdem, U. M., & Hasselmo, M. (2012). A goal-directed spatial navigation model using forward trajectory planning based on grid cells. *The European Journal of Neuroscience*, *35*(6), 916–931.

Fuhs, M. C., & Touretzky, D. S. (2006). A spin glass model of path integration in rat medial entorhinal cortex. *The Journal of Neuroscience*, *26*(16), 4266–4276.

Fyhn, M., Hafting, T., Witter, M. P., Moser, E. I., & Moser, M.-B. (2008). Grid cells in mice. *Hippocampus*, *18*(12), 1230–1238.

Fyhn, M., Molden, S., Witter, M., Moser, E., & Moser, M.-B. (2004). Spatial Representation in the Entorhinal Cortex. *Science*, *305*(5688), 1258–1264.

Garden, D. L. F., Dodson, P. D., O'Donnell, C., White, M. D., & Nolan, M. F. (2008). Tuning of Synaptic Integration in the Medial Entorhinal Cortex to the Organization of Grid Cell Firing Fields. *Neuron*, *60*(5), 875–889.

Gasparini, S., & DiFrancesco, D. (1997). Action of the hyperpolarization-activated current (Ih) blocker ZD 7288 in hippocampal CA1 neurons. *Pflugers Archiv European Journal of Physiology*, *435*(1), 99–106.

Gasparini, S. (2011). Distance- and activity-dependent modulation of spike back-propagation in layer V pyramidal neurons of the medial entorhinal cortex. *Journal of Neurophysiology*, *105*(3), 1372–1379.

Gatome, C. W., Slomianka, L., Lipp, H. P., & Amrein, I. (2010). Number estimates of neuronal phenotypes in layer ii of the medial entorhinal cortex of rat and mouse. *Nsc*, *170*(1), 156–165.

Ghosh, K. K., Burns, L. D., Cocker, E. D., Nimmerjahn, A., Ziv, Y., Gamal, A. E., & Schnitzer, M. J. (2011). Miniaturized integration of a fluorescence microscope. *Nature Methods*, *8*(10), 871–878.

Giocomo, L. M., & Hasselmo, M. E. (2008). Computation by oscillations: Implications of experimental data for theoretical models of grid cells. *Hippocampus*, *18*(12), 1186–1199.

Giocomo, L. M., Moser, M.-B., & Moser, E. I. (2011). Computational Models of Grid Cells. *Neuron*, *71*(4), 589–603.

Giocomo, L. M., Zilli, E. A., Fransen, E., & Hasselmo, M. E. (2007). Temporal Frequency of Subthreshold Oscillations Scales with Entorhinal Grid Cell Field Spacing. *Science*, *315*(5819), 1719–1722.

Givens, B., & Olton, D. S. (1994). Local modulation of basal forebrain: effects on working and reference memory. *Journal of Neuroscience*, *14*(6), 3578–3587.

Golding, N. L., Jung, H. Y., Mickus, T., & Spruston, N. (1999).

Dendritic calcium spike initiation and repolarization are controlled by distinct potassium channel subtypes in CA1 pyramidal neurons. *The Journal of Neuroscience*, *19*(20), 8789–8798.

Hafting, T., Fyhn, M., Molden, S., Moser, M.-B., & Moser, E. I. (2005). Microstructure of a spatial map in the entorhinal cortex. *Nature*, *436*(7052), 801–806.

Hafting, T., Fyhn, M., Bonnevie, T., Moser, M.-B., & Moser, E. I. (2008). Hippocampus-independent phase precession in entorhinal grid cells. *Nature*, *453*(7199), 1248–1252.

Harris, N. C., & Constanti, A. (1995). Mechanism of block by ZD 7288 of the hyperpolarization-activated inward rectifying current in guinea pig substantia nigra neurons in vitro. *Journal of Neurophysiology*, *74*(6), 2366–2378.

Hasselmo, M. E. (2008). Grid cell mechanisms and function: Contributions of entorhinal persistent spiking and phase resetting. *Hippocampus*, *18*(12), 1213–1229.

Hasselmo, M. E., Giocomo, L. M., & Zilli, E. A. (2007). Grid cell firing may arise from interference of theta frequency membrane potential oscillations in single neurons. *Hippocampus*, *17*(12), 1252–1271.

Heys, J. G., Rangarajan, K. V., & Dombeck, D. A. (2014). The Functional Micro-organization of Grid Cells Revealed by Cellular-Resolution Imaging. *Neuron*, *84*(5), 1079–1090.

Hoffman, D. A., Magee, J. C., Colbert, C. M., & Johnston, D. (1997). K+ channel regulation of signal propagation in dendrites of hippocampal

pyramidal neurons. *Nature*, *387*(6636), 869–875.

Jeewajee, A., Barry, C., O'Keefe, J., & Burgess, N. (2008). Grid cells and theta as oscillatory interference: Electrophysiological data from freely moving rats. *Hippocampus*, *18*(12), 1175–1185.

Jones, R. S. (1994). Synaptic and intrinsic properties of neurons of origin of the perforant path in layer II of the rat entorhinal cortex in vitro. *Hippocampus*, *4*(3), 335–353.

Kitamura, T., Pignatelli, M., Suh, J., Kohara, K., Yoshiki, A., Abe, K., & Tonegawa, S. (2014). Island cells control temporal association memory. *Science*, *343*(6173), 896–901.

Klee, M., & Rall, W. (1977). Computed potentials of cortically arranged populations of neurons. *Journal of Neurophysiology*, *40*(3), 647–666.

Klink, R., & Alonso, A. (1997). Morphological Characteristics of Layer II Projection Neurons in the Rat Medial Entorhinal Cortex. *Hippocampus*, 1–13.

Krueppel, R., Remy, S., & Beck, H. (2011). Dendritic Integration in Hippocampal Dentate Granule Cells. *Neuron*, *71*(3), 512–528.

Krupic, J., Bauza, M., Burton, S., Barry, C., & O'Keefe, J. (2015). Grid cell symmetry is shaped by environmental geometry. *Nature*, *518*(7538), 232–235.

Krüppel, T. (1993). Inward rectification by hyperpolarization-activated Na current in the marine ciliate Euplotes vannus. *The Journal of Membrane Biology*, *133*(3), 263–270.

Larkum, M. E., Zhu, J. J., & Sakmann, B. (1999). A new cellular mechanismfor coupling inputs arrivingat different cortical layers. *Nature*, 1–4.

Larkum, M. E., & Zhu, J. J. (2002). Signaling of layer 1 and whisker-evoked Ca2+ and Na+ action potentials in distal and terminal dendrites of rat neocortical pyramidal neurons in vitro and in vivo. *The Journal of Neuroscience*, *22*(16), 6991–7005.

Larkum, M. E., Nevian, T., Sandler, M., Polsky, A., & Schiller, J. (2009). Synaptic integration in tuft dendrites of layer 5 pyramidal neurons: a new unifying principle. *Science*.

Lavzin, M., Rapoport, S., Polsky, A., Garion, L., & Schiller, J. (2012). Nonlinear dendritic processing determines angular tuning of barrel cortex neurons in vivo. *Nature*, *490*(7420), 397–401.

Lee, D., Lin, B.-J., & Lee, A. K. (2012). Hippocampal place fields emerge upon single-cell manipulation of excitability during behavior. *Science*, *337*(6096), 849–853.

Lipowsky, R., Gillessen, T., & Alzheimer, C. (1996). Dendritic Na+ channels amplify EPSPs in hippocampal CA1 pyramidal cells. *Journal of Neurophysiology*, *76*(4), 2181–2191.

Lipton, P. A., & Eichenbaum, H. (2008). Complementary Roles of Hippocampus and Medial Entorhinal Cortex in Episodic Memory. *Neural Plasticity*, *2008*, 1–8.

Losonczy, A., & Magee, J. C. (2006). Integrative Properties of Radial Oblique Dendrites in Hippocampal CA1 Pyramidal Neurons. *Neuron*, *50*(2), 291–307.

Lörincz, A., Notomi, T., Tamás, G., Shigemoto, R., & Nusser, Z. (2002). Polarized and compartment-dependent distribution of HCN1 in pyramidal cell dendrites. *Nature Neuroscience*, *5*(11), 1185–1193.

Magee, J. C. (1999). Dendritic lh normalizes temporal summation in hippocampal CA1 neurons. *Nature Neuroscience*, *2*(6), 508–514.

Magee, J. C. (2000). Dendritic integration of excitatory synaptic input. *Nature Reviews Neuroscience*, *1*(3), 181–190. doi:10.1038/35044552

Magee, J. C., & Cook, E. P. (2000). Somatic EPSP amplitude is independent of synapse location in hippocampal pyramidal neurons. *Nature Neuroscience*, *3*(9), 895–903.

Magistretti, J., & Alonso, A. (1999). Biophysical Properties and Slow Voltage-dependent Inactivation of a Sustained Sodium Current in Entorhinal Cortex Layer-II Principal Neurons A Whole-Cell and Single-Channel Study, 1–19.

Magistretti, J., Ragsdale, D. S., & Alonso, A. (1999a). Direct demonstration of persistent Na+ channel activity in dendritic processes of mammalian cortical neurones. *The Journal of Physiology*, *521 Pt 3*, 629–636.

Magistretti, J., Ragsdale, D., & Alonso, A. (1999b). High Conductance Sustained Single-Channel Activity Responsible for the Low-Threshold Persistent Na+ Current in Entorhinal Cortex Neurons, 1–8.

Major, G., Larkum, M. E., & Schiller, J. (2013). Active Properties of Neocortical Pyramidal Neuron Dendrites. *Annual Review of Neuroscience*, *36*(1), 1–24.

Makara, J. K., & Magee, J. C. (2013). Variable dendritic integration in hippocampal CA3 pyramidal neurons. *Neuron*, *80*(6), 1438–1450.

Matsuzaki, M., Ellis-Davies, G. C. R., Nemoto, T., Miyashita, Y., Iino, M., & Kasai, H. (2001). Dendritic spine geometry is critical for AMPA receptor expression in hippocampal CA1 pyramidal neurons. *Nature Neuroscience*, *4*(11), 1086–1092.

McNaughton, B. L., Battaglia, F. P., Jensen, O., Moser, E. I., & Moser, M.-B. (2006). Path integration and the neural basis of the 'cognitive map'. *Nature Reviews Neuroscience*, *7*(8), 663–678.

Medinilla, V., Johnson, O., & Gasparini, S. (2012). Features of proximal and distal excitatory synaptic inputs to layer V neurons of the rat medial entorhinal cortex. *The Journal of Physiology*, *591*(1), 169–183.

Mizumori, S. J., Perez, G. M., Alvarado, M. C., Barnes, C. A., & McNaughton, B. L. (1990). Reversible inactivation of the medial septum differentially affects two forms of learning in rats. *Brain Research*, *528*(1), 12–20.

Moser, E. I., Roudi, Y., Witter, M. P., Kentros, C., Bonhoeffer, T., & Moser, M.-B. (2014). Grid cells and cortical representation. *Nature Publishing Group*, *15*(7), 466–481.

Müller, A., Kukley, M., Stausberg, P., Beck, H., Müller, W., & Dietrich, D. (2005). Endogenous Ca2+ buffer concentration and Ca2+ microdomains in hippocampal neurons. *The Journal of Neuroscience*, *25*(3), 558–565.

Navratilova, Z., Giocomo, L. M., Fellous, J.-M., Hasselmo, M. E., &

McNaughton, B. L. (2011). Phase precession and variable spatial scaling in a periodic attractor map model of medial entorhinal grid cells with realistic after-spike dynamics. *Hippocampus*, *22*(4), 772–789.

Nevian, T., Larkum, M. E., Polsky, A., & Schiller, J. (2007). Properties of basal dendrites of layer 5 pyramidal neurons: a direct patch-clamp recording study. *Nature Neuroscience*, *10*(2), 206–214.

Nicholson, D. A., Trana, R., Katz, Y., Kath, W. L., Spruston, N., & Geinisman, Y. (2006). Distance-dependent differences in synapse number and AMPA receptor expression in hippocampal CA1 pyramidal neurons. *Neuron*, *50*(3), 431–442.

Nobel Media AB 2014. (2014, December 27). The Nobel Prize in Physiology or Medicine 2014. *Nobelprize.org*. Retrieved December 27, 2014

Nolan, M. F., Dudman, J. T., Dodson, P. D., & Santoro, B. (2007). HCN1 Channels Control Resting and Active Integrative Properties of Stellate Cells from Layer II of the Entorhinal Cortex. *Journal of Neuroscience*, *27*(46), 12440–12451.

O'Keefe, J., & Burgess, N. (2005). Dual phase and rate coding in hippocampal place cells: Theoretical significance and relationship to entorhinal grid cells. *Hippocampus*, *15*(7), 853–866.

O'Keefe, J., & Dostrovsky, J. (1971). The hippocampus as a spatial map. Preliminary evidence from unit activity in the freely-moving rat. *Brain Research*, *34*(1), 171–175.

O'Keefe, J. (1976). Place units in the hippocampus of the freely moving rat. *Experimental Neurology*, *51*(1), 78–109.

O'Keefe, J., & Recce, M. L. (1993). Phase relationship between hippocampal place units and the EEG theta rhythm. *Hippocampus*, *3*(3), 317–330.

O'Keefe, J., & Nadel, L. (1978). The Hippocampus as a Cognitive Map. *Oxford University Press*, 1–296.

Pastoll, H., Ramsden, H. L., & Nolan, M. F. (2012). Intrinsic electrophysiological properties of entorhinal cortex stellate cells and their contribution to grid cell firing fields. *Frontiers in Neural Circuits*, *6*, 17.

Pilly, P. K., & Grossberg, S. (2014). How does the modular organization of entorhinal grid cells develop? *Frontiers in Human Neuroscience*, *8*, 337.

Quilichini, P., Sirota, A., & Buzsáki, G. (2010). Intrinsic circuit organization and theta-gamma oscillation dynamics in the entorhinal cortex of the rat. *The Journal of Neuroscience*, *30*(33), 11128–11142.

Ray, S., Naumann, R., Burgalossi, A., Tang, Q., Schmidt, H., & Brecht, M. (2014). Grid-layout and theta-modulation of layer 2 pyramidal neurons in medial entorhinal cortex. *Science*, *343*(6173), 891–896.

Remme, M. W. H., Lengyel, M., & Gutkin, B. S. (2010). Democracy-Independence Trade-Off in Oscillating Dendrites and Its Implications for Grid Cells. *Neuron*, *66*(3), 429–437.

Samsonovich, A., & McNaughton, B. L. (1997). Path integration and cognitive mapping in a continuous attractor neural network model. *Journal of Neuroscience*, *17*(15), 5900–5920.

Sargolini, F. (2006). Conjunctive Representation of Position, Direction, and Velocity in Entorhinal Cortex. *Science*, *312*(5774), 758–762.

Schiller, J., & Schiller, Y. (2001). NMDA receptor-mediated dendritic spikes and coincident signal amplification. *Current Opinion in Neurobiology*, *11*(3), 343–348.

Schiller, J., Major, G., Koester, H. J., & Schiller, Y. (2000a). NMDA spikes in basal dendrites of cortical pyramidal neurons. *Nature*, *404*(6775), 285–289.

Schiller, J., Major, G., Koester, H., & Schiller, Y. (2000b). NMDA spikes in basal dendrites of cortical pyramidal neurons, 1–5.

Schiller, J., Schiller, Y., Stuart, G., & Sakmann, B. (1997). Calcium action potentials restricted to distal apical dendrites of rat neocortical pyramidal neurons. *The Journal of Physiology*, *505 (Pt 3)*, 605–616.

Schmidt-Hieber, C., & Hausser, M. (2013). Cellular mechanisms of spatial navigation in the medial entorhinal cortex. *Nature Neuroscience*, *16*(3), 325–331.

Schwartz, S. P., & Coleman, P. D. (1981). Neurons of origin of the perforant path. *Experimental Neurology*, *74*(1), 305–312.

Schwartzkroin, P. A., & Slawsky, M. (1977). Probable calcium spikes in hippocampal neurons. *Brain Research*, *135*(1), 157–161.

Schwindt, P., & Crill, W. (1996). Equivalence of amplified current flowing from dendrite to soma measured by alteration of repetitive firing and by voltage clamp in layer 5 pyramidal neurons. *Journal of*

Neurophysiology, *76*(6), 3731–3739.

Seong, H. J., Behnia, R., & Carter, A. G. (2014). Impact of subthreshold membrane potential on synaptic responses at dendritic spines of layer 5 pyramidal neurons in the prefrontal cortex. *Journal of Neurophysiology*, *111*(10), 1960–1972.

Sheffield, M. E. J., & Dombeck, D. A. (2014). Calcium transient prevalence across the dendritic arbour predicts place field properties. *Nature*, *517*(7533), 200–204.

Smith, S. L., Smith, I. T., Branco, T., & Häusser, M. (2013). Dendritic spikes enhance stimulus selectivity in cortical neurons in vivo. *Nature*, *503*(7474), 115–120.

Spruston, N. (2008). Pyramidal neurons: dendritic structure and synaptic integration. *Nature Reviews Neuroscience*, *9*(3), 206–221.

Stuart, G., & Sakmann, B. (1994). Active propagation of somatic action potentials into neocortical pyramidal cell dendrites. *Nature*, 1–4.

Stuart, G., Spruston, N., Sakmann, B., & Hausser, M. (1997). Action potential initiation and backpropagation in neurons of the mammalian CNS. *Trends in Neurosciences*, *20*(3), 125–131.

Tang, Q., Burgalossi, A., Ebbesen, C. L., Ray, S., Naumann, R., Schmidt, H., et al. (2014). Pyramidal and Stellate Cell Specificity of Grid and Border Representations in Layer 2 of Medial Entorhinal Cortex. *Neuron*.

Ulanovsky N, Yartsev MM: Evidence for theta oscillations in the hippocampus of flying bats. Society for Neuroscience Abstract 2011, 937:27.

van Strien, N. M., Cappaert, N. L. M., & Witter, M. P. (2009). The anatomy of memory: an interactive overview of the parahippocampal–hippocampal network. *Nature Reviews Neuroscience*, *10*(4), 272–282.

Visan, V., Heinemann, U., Volynets, A., & Müller, W. (2002). Calcium currents in rat entorhinal cortex layer II stellate and layer III pyramidal neurons in acute brain slice. *Neuroscience Letters*, *327*(3), 153–156.

Waters, J., Larkum, M., Sakmann, B., & Helmchen, F. (2003). Supralinear Ca2+ influx into dendritic tufts of layer 2/3 neocortical pyramidal neurons in vitro and in vivo. *The Journal of Neuroscience*, *23*(24), 8558–8567.

Welday, A. C., Shlifer, I. G., Bloom, M. L., Zhang, K., & Blair, H. T. (2011). Cosine directional tuning of theta cell burst frequencies: evidence for spatial coding by oscillatory interference. *The Journal of Neuroscience, 31*(45), 16157–16176.

Welinder, P. E., Burak, Y., & Fiete, I. R. (2008). Grid cells: The position code, neural network models of activity, and the problem of learning. *Hippocampus*, *18*(12), 1283–1300.

Williams, S. R., & Stuart, G. J. (2000). Site independence of EPSP time course is mediated by dendritic I(h) in neocortical pyramidal neurons. *Journal of Neurophysiology*, *83*(5), 3177–3182.

Williams, S. R., & Stuart, G. J. (2002). Dependence of EPSP efficacy on synapse location in neocortical pyramidal neurons. *Science*, *295*(5561), 1907–1910.

Williams, S. R., & Stuart, G. J. (2003). Role of dendritic synapse location in the control of action potential output. *Trends in Neurosciences*, *26*(3),

147–154.

Witter, M. P., & Moser, E. I. (2006). Spatial representation and the architecture of the entorhinal cortex. *Trends in Neurosciences*, *29*(12), 671–678.

Witter, M. P., Wouterlood, F. G., Naber, P. A., van Haeften, T (2000). Anatomical Organization of the Parahippocampal-Hippocampal Network, *911*(1), 1–24.

Xu, N.-L., Harnett, M. T., Williams, S. R., Huber, D., O'Connor, D. H., Svoboda, K., & Magee, J. C. (2012). Nonlinear dendritic integration of sensory and motor input during an active sensing task. *Nature*, *492*(7428), 247–251.

Yartsev, M. M., Witter, M. P., & Ulanovsky, N. (2011). Grid cells without theta oscillations in the entorhinal cortex of bats. *Nature*, *479*(7371), 103–107.

Zhang, S. J., Ye, J., Miao, C., Tsao, A., Cerniauskas, I., Ledergerber, D., et al. (2013). Optogenetic dissection of entorhinal-hippocampal functional connectivity. *Science*, *340*(6128), 1232627–1232627.

Zilli, E. A., & Hasselmo, M. E. (2010). Coupled Noisy Spiking Neurons as Velocity-Controlled Oscillators in a Model of Grid Cell Spatial Firing. *Journal of Neuroscience*, *30*(41), 13850–13860.